Università Politecnica delle Marche
Scuola di Dottorato di Ricerca in Scienze dell'Ingegneria
Corso di Dottorato in Ingegneria Industriale

Air pollution from natural and anthropogenic sources over Mediterranean region: assessment of an online coupled meteorological and air quality model

Ph.D. Dissertation of:
Mauro Morichetti

Supervisor:
Prof. Giorgio Passerini

Assistant Supervisor:
Dr. Umberto Rizza

Assistant Supervisor:
Dr. Mary Barth

Ph.D. Course coordinator:
Prof. Ferruccio Mandorli

XVII edition - new series

Università Politecnica delle Marche
Dipartimento di Ingegneria Industriale e Scienze Matematiche
Via Brecce Bianche — 60131 - Ancona, Italia

Acknowledgements

To Prof. Giorgio Passerini and Dr. Umberto Rizza, for helping me on the PhD carrier and for trusting me, even when I did not deserve it.

To Dr. Mary Barth and Dr. Sasha Madronich, for giving me the opportunity to take part in the NCAR family, but above all, for Phd-Dissertation advices and helps. To the Scientists, Researchers and PhD students of the NCAR Institute for the time you have dedicated to my WRF-Chem understanding.

To all the people from the DIISM department for assisting me every day.

This one, with gratitude, is for

Rosane, Santa, Ave, Manuela, Mario, Alessandro and Brando

"…mi ricordi una poesia che non riesco a ricordare,
una canzone che non è mai esistita
e un posto in cui non devo essere mai stato…"
(Efraim Medina Reyes)

Abstract

A study to better understand and quantify the source of air pollution in Italy and the surrounding Mediterranean region is proposed. Suspected sources of pollutants include human activities, natural hydrocarbons from forests (isoprene and terpenes) and episodes of wind-blown mineral dust from the Sahara Desert. A deep understanding of these sources is fundamental to developing science-based mitigation actions. The study addresses specifically the natural hydrocarbons and dust, using a state-of-the-art chemistry transport model (Weather Research and Forecasting with Chemistry). The WRF-Chem system is an "online" regional scale prediction model designed to simulate many detailed meteorological, gas and aerosol chemical processes, with full coupling between the different components and phases. This study documents two different applications, and their evaluation, that have been made using WRF-Chem model in order to improve its representation of gas and aerosol chemical processes. The first application includes the description, examination and test of a set of updates made to the MEGAN version 2.04 (Model of Emission Gas and Aerosols from Nature) model, one of the BVOC (biogenic volatile organic compound) emission model includes in WRF-Chem, by two different test cases (i.e. the first at European level, and the second, at United States level). The main objective of the second WRF-Chem application, involves the assessment of Sharan dust outbreaks to the southern Europe and how they compare to anthropogenic emissions over a whole year (2017).

The MEGAN sensitivity study, at European level, includes four simulations. The first one is (1) the control one: the MEGAN database has been used without any change (Megan_V2.04); on the (2) second one all the activity factors (γ_i) have been modified following the MEGAN version 2.10 (Megan_Gamma). The (3) third simulation adds the PFTs (Plant Functional Type) emission factors changes to the activity factors (Megan_GammaPFT); finally, the (4) last one calculates more the isoprene emission factor within the MEGAN emission algorithm, instead of reading it directly from the input database (Megan_GammaPFTISO). The simulations listed above, are applied to simulate an intense ozone event that took place over central Italy in August 13th, 2015. Results for isoprene and α-pinene emissions demonstrate the updating the MEGAN code the emissions increase considerably (i.e. Zagreb has an increase about 100 mol/km^{2}hr and Kiev about 50 mol/km^2 hr). The comparison with the AIRBASE (European Environment Agency air quality network) showed that only the temporal and spatial distribution of the O_3 are well represented; the control simulation demonstrated the ozone better results, since the updates simulations increase the ozone concentration of nearly from 20 to 40 ppb. The other trace gases considered (NO_2 and CO) model results are very underestimate, respectively by a factor of 2 and 10 regardless of simulations considered, since the MEGAN updates does not affect that compounds.

On the other hands, the U.S. MEGAN sensitivity case of study, includes two simulations: the control one (Megan_V2.04) and a simulation with all code changes applied (Megan_GammaPFTISO). They are concurrently with the NOMADSS (Nitrogen, Oxidants, Mercury and Aerosol

Distributions, Sources and Sinks) field campaign (from June 1th 00:00 UTC to June 15th 00:00 UTC, 2013), in order to validate the updates with that dataset. Isoprene concentrations overestimate the NOMADSS considerably up to a factor of 5 (average discrepancy is about 7000 ppt). The O_3 modeled values confirm the European case of study, updating MEGAN ozone concentrations increase by 10 %; the NO_x concentrations are overestimate, as European case, but with better agreement. The MEGAN updates do not take effects on the NO_x concentrations.

Last WRF-Chem application has one-year time duration (from January 1st 2017 00:00 UTC to January 1st 2018 00:00 UTC) where two simulations are carried out: the first considering only the dust emission (chem_opt = 401 – "DUSTONLY" simulation) and the second one considering all the type of emissions (biogenic, biomass burning and anthropogenic) (chem_opt = 201 – "MOZMOSAIC" simulation); both of simulations use the GOCART (Goddard Chemistry Aerosol Radiation and Transport) dust emission scheme. The NCEP/NCAR reanalysis and the University of Wyoming surface stations network have been used to assess the spatial resolution of simulated temperature, relative humidity and wind speed and direction, showing a great capability of WRF-Chem model to reproduce the experimental data and its spatial trend. The association between the modeled dust column mass density [kg/m^2] and the field with the corresponding MERRA-2 (Modern-Era Retrospective Analysis for Research and Applications) reanalysis showed an evident dust load overestimated over the North-Africa regions (i.e. by a factor of 10 - MERRA-2 = $2x10^{-4}$ kg/m^2; WRF-Chem = $2x10^{-3}$ kg/m^2). The dust modeled overestimate is confirmed by

the comparison of both simulations with the AERONET AOD (550 nm) products; i.e. Rome and Naples stations have nearly the same year trend, AOD peaks are captured as well, but the dust magnitude is overestimated from both simulations (e.g. May – $AOD_{DUSTONLY}$ = 0.9; $AOD_{MOZMOSAIC}$ = 1.2; $AOD_{AERONET}$ = 0.3).

Notations

Abbreviations

AERONET	*Aerosol Robotic NETwork.*
AFWA	*Air Force Weather Agency.*
AIRBASE	*European Air Quality DataBASE.*
AOD	*Aerosol Optical Depth.*
ARPAM	*Regional Environmental Protection Agency of Marche ("Autorità Regionale Protezione Ambientale Marche").*
BEIS	*Biogenic Emissions Inventory System.*
CAM-CHEM	*Community Atmosphere Model – Chemistry.*
CONUS	*Contiguous United States.*
CTM	*Chemical Transport Models.*
ECMWF	*European Centre for Medium-Range Weather Forecasts.*
EDGAR	*Emission Database for Global Atmospheric Research.*
EEA	*European Environment Agency.*
EMEP	*European Monitoring and Evaluation Programme.*
EXTCOEF	*Extinction Coefficient.*
FDDA	*Four-Dimensional Data Assimilation.*
FINN	*Fire Inventory from NCAR.*
GEOS-CHEM	*Goddard Earth Observing System – Chemistry.*
GMAO	*Global Modeling and Assimilation Office.*
GOCART	*Goddard Chemistry Radiation and Transport.*

IGAC-GEIA	*International Global Atmospheric Chemistry Global Emissions Inventory Activity.*
LAI	*Leaf Area Index.*
LDF	*Light Dependent Fraction.*
LIF	*Light Independent Fraction.*
MEGAN	*Model of Emissions of Gases and Aerosols from Nature.*
MERRA-2	*Modern-Era Retrospective Analysis for Research and Applications, version 2.*
MISR	*Multi-angle Imaging SpectroRadiometer.*
MODIS	*MODerate resolution Imaging SpectroRadiometer.*
MOSAIC	*Model for Simulating Aerosol Interactions and Chemistry.*
MOZART	*Model for Ozone and Related chemical Tracers.*
NAAMEX	*North American Airborne Mercury Experiment.*
NCAR	*National Center for Atmospheric Research.*
NCEP	*National Center for Environmental Prediction.*
NOAA	*National Oceanic and Atmospheric Administration.*
NOMADSS	*Nitrogen, Oxidants, Mercury and Aerosol Distributions, Sources and Sinks.*
NSF	*National Science Foundation.*
PBL	*Planetary Boundary Layer.*
PCEEA	*Parameterized Canopy Environment Emission Activity.*
PFT	*Plant Functional Type.*
PPFD	*Photosynthetic Photon Flux Density.*
SOAS	*Southern Oxidant and Aerosol Study.*

TROPHONO	*Photolysis of Particulate Nitrate: a Daytime HONO Source and a Re-NOx-ification Pathway in the Troposphere.*
UniWy	*University of Wyoming.*
UTC	*Coordinated Universal Time.*
WRF-CHEM	*Weather Research Forecast – Chemistry.*

Chemical compounds

BVOCs	*Biogenic Volatile Organic Compounds*
CO	*Carbon monoxide*
MACR	*Methacrolein*
MVK	*Methyl vinyl ketone*
NO	*Nitric oxide*
NO_2	*Nitrogen dioxide*
NO_x	*Nitrogen oxides*
O_3	*Ozone*
PM	*Particulate Matter*
VOCs	*Volatile Organic Compounds*
SOA	*Secondary Organic Aerosol*
HONO	*Nitrous Acid*

Contents

List of Figures

List of Table

Appendix A.

Appendix B.

1. Introduction

Problem formulation

Known as the cradle of civilization, the Mediterranean region has been subject to human intervention for millennia since the area is well known for its predominantly mild climate and moderate temperatures; as a matter of fact, around its coasts are lands rich in vegetation species. Unfortunately, forest cover has been significantly reduced throughout the history of human pressure and agriculture. Archaeological remains show that there once were rich forests throughout the area, where now often only shrub or desert remains. Nowadays, 82 million people live in coastal cities accounting for 32% of the region; by 2025 there will be an estimated 150-170 million reaching 60%. The fast population growth along the coastlines, intense rural activity, marine transportation and fishing activities are all phenomena responsible for the exponentially increasing of anthropogenic emissions over the Mediterranean region. The sources of pollutants include also natural emissions, as hydrocarbons from forests (isoprene and terpenes) and episodes of wind-blown mineral dust from arid and semi-arid areas (mainly Saharan Desert); these emissions have permanently been part of earth-atmosphere interactions system, but nowadays with the human "progress", they can react (i.e. physical or chemical transformations) with those anthropogenic resulting in a secondary pollutant.

Topicality of work

In order to assess the growing emissions over the Mediterranean region we used WRF-Chem an "online" chemical transport model. WRF-

Chem is the Weather Research and Forecasting (WRF) model coupled with Chemistry. The novelty of the present study is the utilization of a state-of-the-art chemistry transport model qualified to simulates the emission, transport, mixing, and chemical transformation of trace gases and aerosols simultaneously with the meteorology.

Aim of work

The aim of the work is to simulates dissimilar pollution event and phenomena, for different type of pollutants (gas and aerosol phases), in order to recognize the best WRF-Chem setup in term of physics, metrological and chemistry parameters for Southern Europe.

Methodology of the research

The research includes two main steps: a sensitivity model study to investigate the BVOC interaction with some trace gases as ozone (O_3), nitrogen dioxide (NO_2) and carbon monoxide (CO), and a study to simulate the natural and anthropogenic aerosol source and emission to Mediterranean south region.

Practical value of the results

Understanding the driving parameter (e.g. physical, meteorological chemical) of WRF-Chem model over a selected region (Mediterranean basin), in different pollution event (e.g. ozone event or mineral dust outbreaks), and for different type of emissions (anthropogenic or natural) allows us to have a ready "online" model to apply systematically to study and mitigate atmospheric pollution, and in order to have the ability to forecast extreme dust events several days before they occur.

2. The influence of biogenic emissions on trace gases: MEGAN sensitivity study

2.1. Model of Emission of Gases and Aerosols from Nature: model description

Natural gases, produced by the "earth ecosystems", include mostly biogenic volatile organic compounds (BVOCs). They can have a remarkable impact on the atmosphere chemistry mainly due to two compounds that dominate the annual global flux to the atmosphere: methane and isoprene. Methane is primarily emitted from microbial sources, while isoprene is emitted from vegetation. Terrestrial plants is the source of 90% of atmospheric isoprene (Wagner *et al.*, 1999), while minor sources include microbes, animals and aquatic organisms. As methane is a long-lived compound, we can be fairly certain about the global emission, in contrast, isoprene is a short-lived compound, then its global flux is less certain (Guenther *et al.*, 2006).

The biogenic emission flux has been consistently included in a global and regional chemical transport models, most of the time, as static emission inventories. A regional biogenic emission model, the Biogenic Emissions Inventory System, or BEIS (Pierce and Waldruff, 1991), was developed in the mid 1980s and replaced by the second-generation model, BEIS2 (Pierce *et al.*, 1998), in the late 1990s. Meanwhile, the International Global Atmospheric Chemistry Global Emissions Inventory Activity (IGAC-GEIA), in the early 1990s, started to develop global emission inventories (1 by 1

degree grid) for use in global chemistry and transport models (Graedel *et al.*, 1993). Later, the IGAC-GEIA natural VOC working group developed a model for isoprene and other BVOCs emissions (Guenther *et al.*, 1995). After about 10 years, the Model of Emissions of Gases and Aerosols from Nature (MEGAN) (Guenther *et al.*, 2006) was available to replace both the Guenther et al. 1995 global emission model and the BEIS/BEIS2 regional emission models (Pierce and Waldruff, 1991; Pierce *et al.*, 1998).

MEGAN model estimates the emission rate of trace gases and aerosols from terrestrial ecosystems into the atmosphere at a specific location and time as

$$EMISSION_{Megan} = [\varepsilon][\gamma][\rho] \quad (1)$$

where:

- **ε** is the emission of a compound into at standard conditions [mg/m^{2}h];
- **γ** is the emission activity factor that accounts for emission changes due to deviations from standard conditions (γ is equal to 1 at standard conditions) [normalized ratio];
- **ρ** is a factor that accounts for production and loss within plant canopies [normalized ratio].

The emissions (equation 1) are calculated for each plant functional type (PFT), summed to estimate the total emission at each cell grid cell (1 km^2) and corrected taking account the deviation from the standard condition (γ and ρ parameters). The use of standard conditions permits emission rates observed, under various conditions, to be incorporated into the model. The

standard conditions for the MEGAN canopy-scale emission factors, the current environmental conditions, and the average canopy environmental conditions of the past 24 to 240 hours are summarized to the Table 1 (Guenther *et al.*, 2006).

Table 1: Values of canopy-scale emission factors, environmental conditions parameters and average canopy environmental conditions of the past 24 to 240 h at standard conditions for the MEGAN model (Guenther *et al.*, 2006).

Canopy emission factors	
LAI	5 [m^2/m^2]
Canopy	80% mature 10% growing 10% old foliage
Environmental conditions parameters	
Solar angle	60°
PPFD* transmission from canopy to atmosphere	0.6
Air temperature	303 [K]
Specific Humidity	14 [g/kg]
Wind Speed	3 [m/s]
Soil moisture	0.3 [m^3/m^3]
Average canopy environmental conditions of the past 24 to 240 h	
Leaf temperature	297 [K]
PPFD* for sun leaves	200 [μmol/m^2s]
PPFD* for shade leaves	50 [μmol/m^2s]

*PPFD is the photosynthetic photon flux density

MEGAN divides the surface of each grid cell into different PFTs, this classification enables MEGAN to simulate different light, temperature distributions, LAI (Leaf Area Index) and leaf age seasonal patterns for

different canopy types (e.g. needle evergreen trees and needle deciduous trees). Table 2 illustrates how the global isoprene emission factors differ between different PFTs. Broadleaf trees and shrubs have the highest average emission factor followed by needle evergreen tree with about a factor of six lower, then the needle deciduous tree and grass PFTs with an average emission factor of 20 lower, and finally, the crop PFT with about two orders of magnitude lower. Table 2 also shows the isoprene emission factor for broadleaf trees ranges from 0.1 to 30 mg/m^{2}h emphasizing the significant variability associated with the isoprene emission factors assigned to different species within a single PFT (Guenther *et al.*, 2006).

Table 2: Global average isoprene emission factors ε [mg/m^{2}h], land area [10^6 km^2] to the annual global isoprene associated with MEGAN plant functional types (Guenther *et al.*, 2006).

		Broadleaf Evergreen and Deciduous Trees	***Needle Evergreen Trees***	***Needle Deciduous Trees***	***Shrubs***	***Crops***	***Grass and other***
Emission factor	Average	12.6	2	0.7	10.7	0.09	0.5
	Range	0.1-30	0.01-13	0.01-2	0.1-30	0.01-1	0.4-1.2
Land area	Global	13.4-38.5	8.6-20	1.3-3.9	15.6-24	8-36.5	17.2-38.6
Isoprene emission	Global	0.51	1.1	<0.01	0.46	03	0.014

Trees are the core of most isoprene emission rate measurement campaigns and studies, their economic value has led to the compilation of high-resolution tree inventories in most part of the world. Figure 1 explains

the global distribution of PFT specific isoprene emission factors. Broadleaf tree isoprene emission ranges from 8 to 16 mg/m^{2}h in most regions but are lower than 1 mg/m^{2}h, and higher than16 mg/m^{2}h, in other few regions. Needle evergreen tree range from 4 mg/m^{2}h in Canada to lower then 0.5 mg/m^{2}h in the U.S. and Europe. For their lesser economic importance, there is less quantitative data on distributions of isoprene emission factors for shrub and grass, however, isoprene emission is rarely observed from plants that are entirely non-woody. Even the agricultural landscapes are isoprene sources: plantations of isoprene-emitting trees (e.g., coconuts-trees, oil palms and cacao-trees) are major isoprene sources, at least in some locations. MEGAN uses the global crop distribution database of Leff, Ramankutty, and Foley 2004 to identify agricultural landscapes where isoprene emissions have a valuable rate (Guenther *et al.*, 2006).

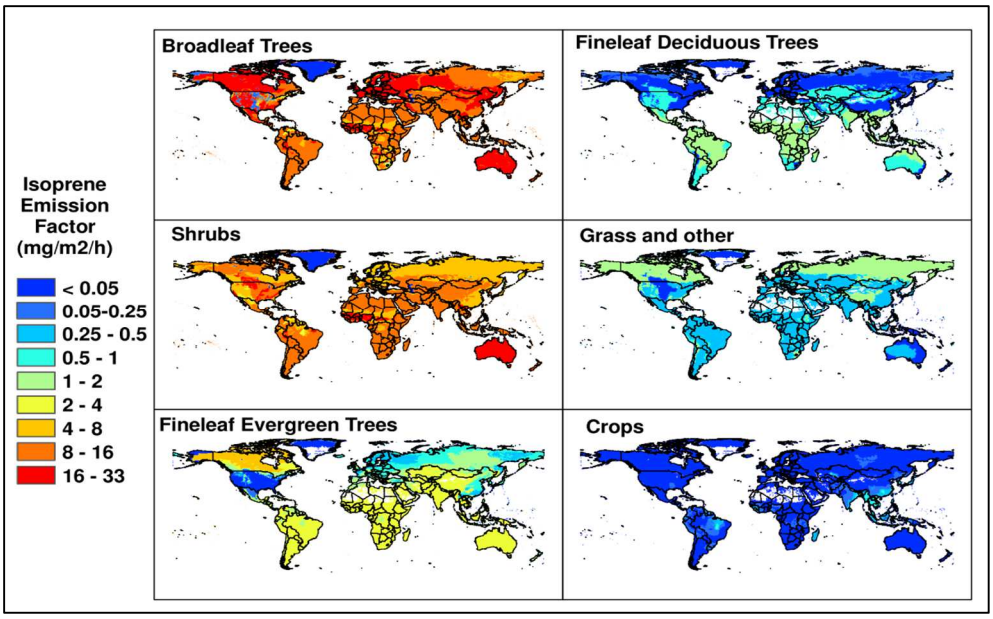

Figure 1: Global distribution of isoprene emission factors for the MEGAN PFTs (Guenther *et al.*, 2006).

The emission activity factor describes variations due to the physiological and phenological processes. Its total factor is the product of single emission activity factors calculated as

$$\gamma = \gamma_{CE} \cdot \gamma_{age} \cdot \gamma_{SM} \qquad (2)$$

where:

- γ_{ce} describes variation due to LAI and light, temperature, humidity and wind conditions within the canopy environment [dimensionless];
- γ_{age} makes adjustments for effects of leaf age [dimensionless];

- γ_{sm} accounts for direct changes in γ due to changes in soil moisture [dimensionless].

The capability of a leaf to emit isoprene depends by a number of physical and biological factors, the driving factors are the incident photosynthetic photon flux density (PPFD) and leaf temperature, which could control emissions on a different time scales (from seconds to weeks) (Guenther *et al.*, 1993). A leaf's capacity to emit isoprene is also influenced by leaf phenology: young leaves emit no isoprene, mature leaves emit isoprene maximally, and for old leaves, emission capacity gradually declines. Moreover, soil characteristics play a role in the plants BVOC emission ability, and while, studies indicate that emission is less sensitive than photosynthesis to soil moisture (Pegoraro *et al.*, 2004), increasing drought effects significantly influence isoprene emission (Guenther *et al.*, 2006; Jiang *et al.*, 2018).

The integration of MEGAN within the earth system model (e.g. temperature, solar radiation and soil moisture) allows examinations of interactions between isoprene emissions and the surrounding environment. The standard MEGAN environment model is based on the methods described by Guenther et al. 1999: it estimates incident PPFD and temperature at five canopy depths, it also includes a leaf isoprene-emitting model that is driven by humidity, solar insolation, ambient temperature, and soil moisture. The above algorithm has been widely used to simulate the response of isoprene emission to changes in light and temperature, but its computational cost made it not very adaptable in the chemical transport models (CTM), so over the years it has been replaced by the parameterized canopy environment emission activity (PCEEA) algorithm,

$$\gamma_{CE} = \gamma_{LAI} \cdot \gamma_P \cdot \gamma_T \quad (3)$$

where γ_{LAI}, γ_P e γ_T account for variations associated with LAI, PPFD and temperature. The BVOC emissions is a product of both the local state (T, PPFD) and the "climate" (soil moisture, heat waves/drought). And therefore, the emissions are a function of both the instantaneous temperature and the average temperature over the past 1 or 10 days (Figure 2) (Guenther *et al.*, 2006).

The canopy-scale isoprene emission response to photosynthetic photon flux density (PPFD) variations is simulated as

$$\begin{gathered} \gamma_P = 0 \\ a < 0 \; a > 180 \end{gathered} \quad (4)$$

$$\gamma_P = sin(a)\left[2.46\left(1 + 005 \cdot \left(P_{daily} - 400\right)\right)\varphi \cdot 0.9\,\varphi^2\right] \quad (5)$$
$$0 < a < 180$$

$$\varphi = P_{ac}/(sin(a)P_{toa}) \quad (6)$$

$$P_{toa} = 3000 + 99 \cdot cos(2 \cdot 3.14 \cdot (DOY - 10)/365) \quad (7)$$

where:

- **P_{daily}** is daily average above canopy PPFD [µmol/m^{2}s];
- ***a*** is the solar angle [degrees];
- ***φ*** is the above canopy PPFD transmission [dimensionless].
- **P_{ac}** is above canopy PPFD [µmol/m^{2}s];
- **P_{toa}** is PPFD at the top of the atmosphere [µmol/m^{2}s];
- **DOY** is the day of the year [Julian day].

The temperature response factor (γ_T) is estimated as

$$\gamma_T = \frac{E_{opt} \cdot CT_2 \cdot exp(CT_1 \cdot x)}{(CT_2 - CT_1 \cdot (1 - exp(CT_2 \cdot x)))} \quad (8)$$

$$x = \frac{\left[\left(\frac{1}{T_{opt}}\right) - \left(\frac{1}{T_{hr}}\right)\right]}{0.00831} \quad (9)$$

$$E_{opt} = 1.75 \cdot exp\,(0.08\,(T_{daily} - 297)) \quad (10)$$

$$T_{opt} = 313 + \left(0.6 \cdot \left(T_{daily} - 297\right)\right) \quad (11)$$

where:

- **T_{hr}** is hourly average air temperature [K];
- **T_{daily}** is daily average air temperature [K];
- **CT_1** (= 80) and **CT_2** (= 200) are empirical coefficients;
- **E_{opt}** is the maximum normalized emission capacity [mol/km^2 hr];
- **T_{opt}** is the temperature at which **E_{opt}** occur [K].

Finally, the emission response to LAI changes are calculated as

$$\gamma_{LAI} = \frac{0.49LAI_C}{[(1 + 0.2LAI_C^2)^{0.5}]} \quad (12)$$

where:

- **LAI_c** is the LAI refer to the month of the simulation [m^2/m^2] (Guenther *et al.*, 2006).

Figure 2 shows the response of γ_{ce} estimates to variations in LAI, solar angle and temperature. Isoprene emission increases with temperature up to a maximum that is dependent on the average temperature of the past 240 hours (T_{24}=T_{240} in this case). The consequence is that MEGAN extrapolations of the isoprene emission response to short term temperature, is often less than the emission predicted by models that do not calculate leaf temperature (e.g. BEIS/BEIS2), because leaf temperature increases slower than environment temperature increases. The PPFD is determined by solar angle and transmission; the γ_{ce} increases linearly with PPFD transmission for canopies that have reported high PPFD levels during the past day (600 and 150 μmol/m^2s, respectively, for sun leaves and shade leaves). The emission increase begins to saturate at high PPFD transmission for lower solar angles. The relationship between LAI and γ_{ce} depends on solar angle and on canopy characteristics (differs for different PFT). Isoprene emissions from canopies with clumped leaves increase relatively slowly with increasing LAI, while a stronger initial increase results with LAI, and a lack of increase with higher

LAI, when the solar angles is less then 30 degrees (i.e. the solar radiation depends proportionally on the solar angle) (Guenther *et al.*, 2006).

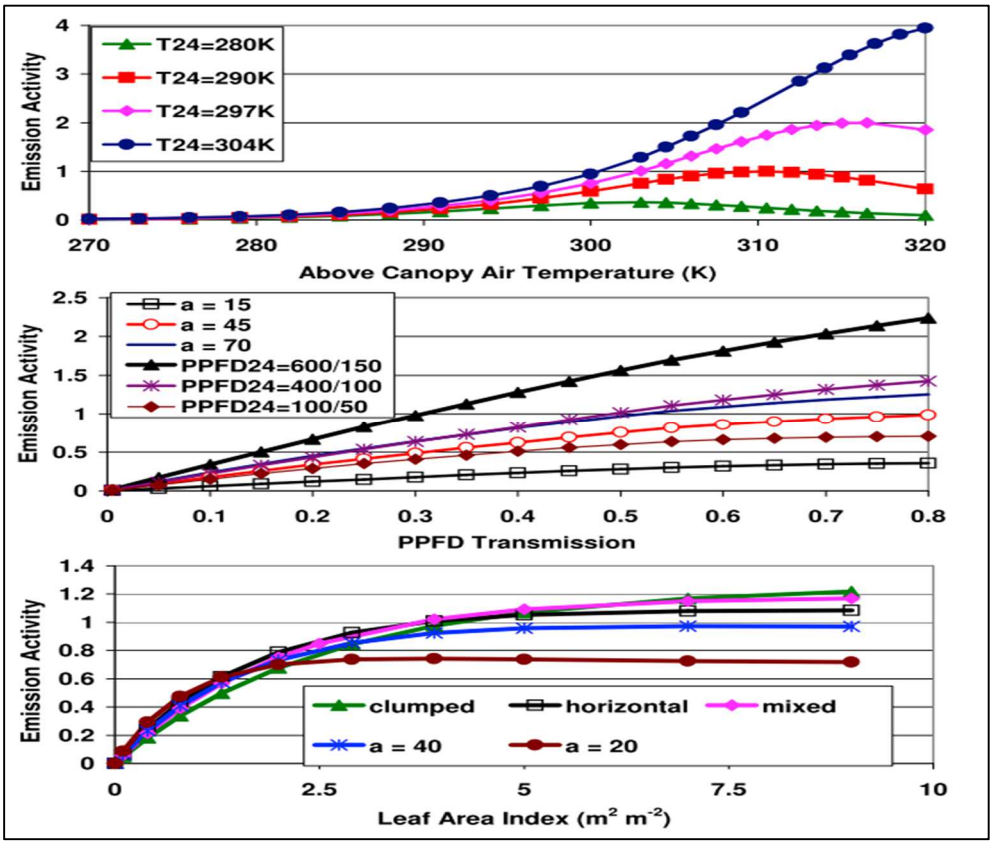

Figure 2: Megan estimates of isoprene emission response to current temperature, PPFD transmission and LAI (Guenther *et al.*, 2006).

The canopy isoprene-emitting capability is also influenced by the leaf age: an increase in foliage is assumed to imply a higher production of isoprene (young leaves), while decreasing foliage is associated to less production of isoprene (old leaves). Guenther et al. 1999 developed an algorithm, with a time step of one month, to simulate the emissions change for young, mature

and old leaves. The algorithm adapted to MEGAN assumes a constant value (γ_{age}=1) for evergreen canopies, while deciduous canopies are divided into four fractions: new foliage (F_{new}), growing foliage (F_{gro}), mature foliage (F_{mat}) and old foliage (F_{old}). The leaf age factor is calculated as

$$\gamma_{age} = F_{new}A_{new} + F_{gro}A_{gro} + F_{mat}A_{mat} + F_{old}A_{old} \quad (13)$$

where A_{new}, A_{gro}, A_{mat}, and A_{old} are the relative emission rates assigned to each canopy fraction, they obviously depend on the plant functional type (PTFs). The canopy is divided into leaf age fractions based on the change in Leaf Area Index (LAI) between the current time step (current month = LAI_c) and the previous time step (previous month = LAI_p) as follow

- if LAI_c=LAI_p (the LAI is mainly formed by mature foliage)

$$F_{mat} = 0.8 \quad (14)$$

$$F_{new} = 0 \quad (15)$$

$$F_{old} = F_{old} = 0.1 \quad (16)$$

- if LAI_p>LAI_c (the LAI is mainly formed by old foliage)

$$F_{new} = F_{gro} = 0 \quad (17)$$

$$F_{old} = \left[\frac{\mathrm{LAI}_p - \mathrm{LAI}_c}{\mathrm{LAI}_p}\right] \quad (18)$$

$$F_{mat} = [1 - F_{old}] \quad (19)$$

the last situation, when the current time step has a higher LAI then the previous time step (LAI_p<LAI_c) (i.e. the LAI is mainly formed by new and growing foliage) it is evaluated as

$$F_{old} = 0 \quad (20)$$

$$F_{gro} = 1 - F_{new} - F_{mat} \quad (21)$$

$$F_{new} = 1 - \left(\frac{LAI_P}{LAI_C}\right) \; t \leq t_i \quad (22)$$

$$F_{new} = \left[\frac{t_i}{t}\right]\left[1 - \left(\frac{LAI_P}{LAI_C}\right)\right] \; t > t_i \quad (23)$$

$$F_{mat} = \left(\frac{LAI_P}{LAI_C}\right) \; t \leq t_m \quad (24)$$

$$F_{mat} = \left(\frac{LAI_P}{LAI_C}\right) + \left[\frac{t - t_m}{t}\right]\left[1 - \left(\frac{LAI_P}{LAI_C}\right)\right] \quad t > t_m \quad (25)$$

$$t_i = 5 + \left(0.7\,(300 - T_t)\right) \quad T_t \leq 303 \tag{26}$$

$$t_i = 2.9 \quad T_t > 303 \tag{27}$$

$$t_m = 2.9\,t_i \tag{28}$$

where:

- **t** is the length of the time step between LAI_c and LAI_p [days];
- $\mathbf{t_i}$ is the time between bud break and the induction of emission [days];
- $\mathbf{T_t}$ is the average ambient temperature [K];
- $\mathbf{t_m}$ is the time between bud break and the initiation of peak emission rates [days] (Guenther *et al.*, 2006).

Different studies have shown that isoprene emission decreases when soil moisture drops below a threshold and eventually becomes insignificant when plants are exposed to extended drought (Pegoraro *et al.*, 2004). MEGAN includes an isoprene emission activity factor, dependent on soil moisture, valued as

$$\gamma_{SM,isoprene} = 1 \qquad \theta > \theta_1 \tag{29}$$

$$\gamma_{SM,isoprene} = \frac{\theta - \theta_W}{\Delta\theta_1} \quad \theta_W < \theta < \theta_1 \tag{30}$$

$$\gamma_{SM,isoprene} = 0 \qquad \theta < \theta_W \tag{31}$$

$$\theta_1 = \theta_W + \Delta\theta_1 \quad (32)$$

where:

- **θ** is soil moisture [m^3/m^3];
- **θ_w** is the soil moisture threshold below which plants cannot extract water from soil [m^3/m^3];
- **$\Delta\theta$** is an empirical parameter from Pegoraro et al. 2004;

MEGAN uses a wilting point database that assigns different θ_w values for each soil type (Table 3) (Chen and Dudhia, 2001).

The last parameter included on the MEGAN emission calculation (equation 1) is a factor that accounts the chemical-physical transformations in the canopy (ρ). A compound emitted into the canopy environment do not always reach the above-canopy atmosphere: it can be consumed by chemical and physical processes on soil and vegetation surfaces while others react within the canopy atmosphere. Some emissions escape to above-canopy atmosphere in a different chemical or physical form. The MEGAN canopy loss factor for isoprene ($\rho_{ISO,ISO}$), is the ratio of isoprene emitted into the above-canopy atmosphere to the isoprene emitted into the canopy atmosphere, and it is calculated as

$$\rho_{ISO,ISO} = 1 - \frac{D}{[\lambda \cdot u^* \cdot \tau + D]} \quad (33)$$

where:

- ***D*** is canopy depth [m] (=15 for generic PFT);
- **u*** is friction velocity [m/s];
- **τ** is the above-canopy isoprene lifetime [s];
- **λ** is an empirically determined parameter (=3 for generic PFT) (Guenther *et al.*, 2006).

Table 3: Soil-related wilting point (θ_w)[m^3/m^3] used by MEGAN soil moisture emission activity factor (Chen and Dudhia, 2001).

Soil type	Wilting point
Sand	0.01
Loamy sand	0.028
Sandy loam	0.047
Silt loam	0.084
Silt	0.084
Loam	0.066
Sandy clay loam	0.067
Silty clay loam	0.12
Clay loam	0.103
Sandy clay	0.1
Silty clay	0.126
Clay	0.138
Organic material	0.06
Water	n.a.
Bedrock	0.094
Other (land–ice)	0.028

2.2.Materials and Methods

2.2.1. Model of Emission of Gases and Aerosols from Nature: model updates

As described in the section above, MEGAN (Model of Emission of Gases and Aerosols from Nature) model estimates the net emission rate of 134 chemicals species (e.g. isoprene, monoterpenes, oxygenated compounds, sesquiterpenes and nitrogen oxide) from terrestrial ecosystems into the above-canopy atmosphere with a resolution of 1 km^2 (Guenther *et al.*, 2006). It can be used in different type of models: global, as GEOS-CHEM (Goddard Earth Observing System) (Bey *et al.*, 2001) or CAM-CHEM (Community Atmosphere Model) (Lamarque *et al.*, 2012), and regional, as WRF-Chem (Grell *et al.*, 2005; Fast *et al.*, 2006).

The use of MEGAN emissions option in WRF-Chem, requires the compilation of an additional preprocessor (megan_bio_emiss.tar) and a global input data (megan.data.tar.gz) (https://www.acom.ucar.edu/wrf-chem/download.shtml); the MEGAN version available on WRF-Chen currently is the version 2.04 (http://lar.wsu.edu/megan/guides.html). The WRF-Chem code reads the global MEGAN input data, maps them on the simulation domain, matching geographical and temporal parameters suitable for the production of biogenic emissions, and creates the biogenic emission files (wrfbiochemi). The MEGAN data elements in the WRF-Chem biogenic emission data file are: the isoprene emission factor (MSEBIO_ISOP) [mol/km^2hr], the grid fraction of different PFTs (PFTP_broad leaf, PFTP_needle leaf, PFTP_shrubs and PFTP_herbaceus biota), the monthly

leaf area index (MLAI) [m^2/m^2], the monthly air temperature (MTSA) [K] and the monthly downward short wave radiation (MSWDOWN) [W/m^2] (Figure 3). Once the preprocessor has created the biogenic emission file, it is used by WRF-Chem code in order to calculate the emission activity factors (γ_i) and the emissions (ε_i) at each grid point for each class compound (Figure 4).

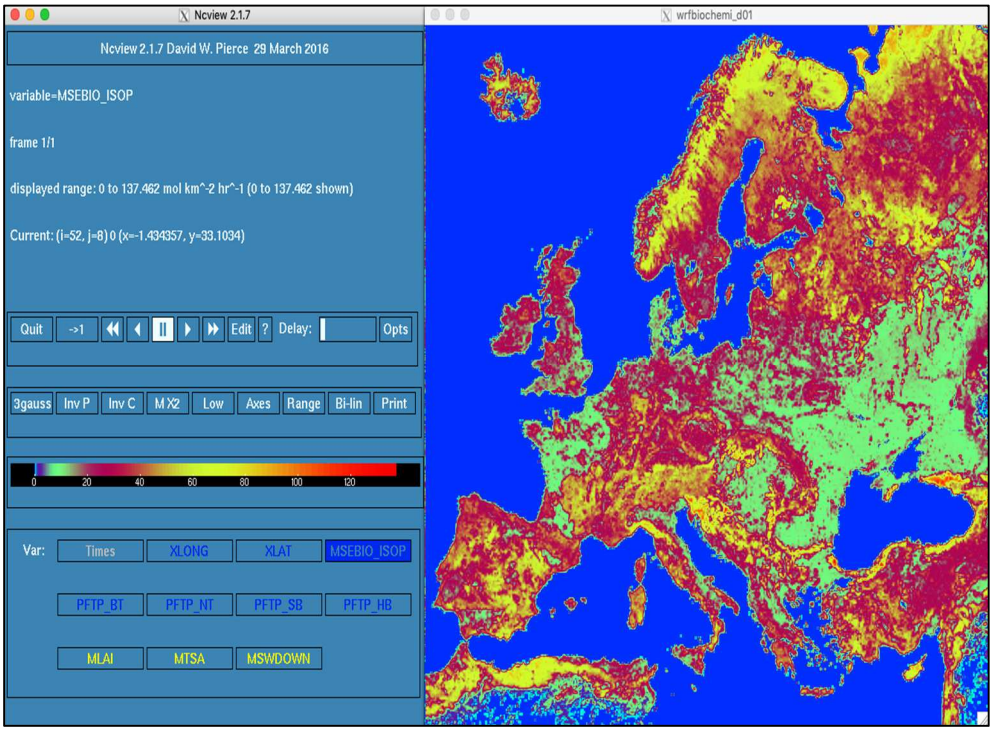

Figure 3: WRF-Chem biogenic emission data file example (wrfbiochemi). The parameter displayed is the amount of isoprene emisson (MSEBIO_ISOP) [mol/km^{2}hr].

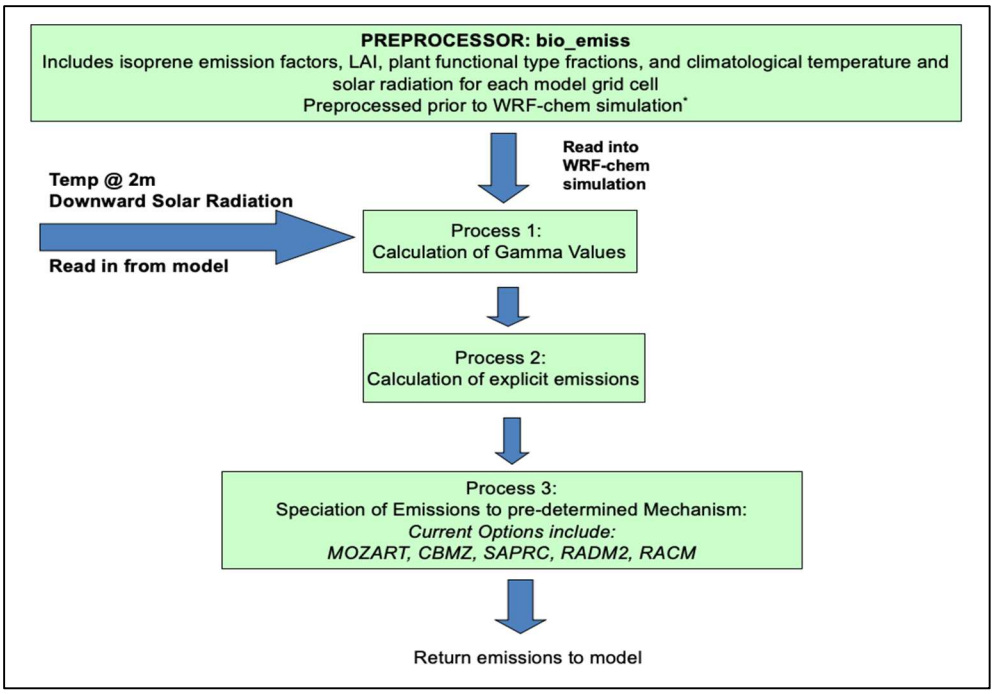

Figure 4: WRF-Chem biogenic emission logic pattern.

The BVOC emission algorithm currently applied to WRF-Chem, results from the combination of equations 1 (ε), 2 (γ_i) and 33 (ρ):

$$EM = \varepsilon \cdot \gamma_{LAI} \cdot \gamma_P \cdot \gamma_T \cdot \gamma_{age} \cdot \gamma_{SM} \cdot \rho \qquad (34)$$

where:

- **EM** the BVOC emission rate [µg/m^{2}hr];
- **ε** emission factor [µg/m^{2}hr];
- γ_{age}, γ_{SM}, γ_{LAI}, γ_P and γ_T are the emission activity factors that accounts respectively for: leaf age, soil moisture, leaf area index,

photosynthetic photon flux density and temperature [normalized ratio];

- **ρ** the loss and production within plant canopy [normalized ratio] (Guenther *et al.*, 2006).

The MEGAN code as is implemented in the WRF-Chem model currently misses of some driving parameters, for example the algorithm and data for the soil moisture emission activity factor (γ_{SM}) and the loss and production within the canopy (ρ) are not yet included, they are set to one. The light dependent factor (γ_P) is only applied to fractions of emission factors based on biological function of plants and not to the surrounding environment features. Last but not least, only maps of isoprene emission factors are used, all other species are assigned an emission factor by PFT (Duhl *et al.*, 2015).

Guenther et al. 2012 developed a new version of MEGAN (version 2.10) updated from MEGAN version 2.0 (Guenther *et al.*, 2006) and MEGAN version 2.02 (Sakulyanontvittaya *et al.*, 2008) to include additional compounds, emission types and controlling processes. After a detailed comparison between equations and parameters within the MEGAN module (module_bioemi_megan2.F) implemented to WRF-Chem code, and the new MEGAN version 2.10 paper (Guenther et al. 2012) the most important updates the code requires are: the update of emission (ε) and emission activity factors (γ), the increase of number of plant function types (PFTs) and the update of leaf area index values. Finally, the changes made in this study to the MEGAN algorithm implemented in WRF-Chem have been the following: (1) update of the emission activity factors (γ_i), (2) increase the number of biogenic compound classes (and the data related to them), (3) update of

emission factor values for each plant functional type (PFT) and (4) the assignment of the emission factor by PFT to isoprene.

One of the main innovations of MEGAN v2.10, is that the emission activity factors, of each compound classes, are divided by a light-dependent fraction (LDF) with the remaining fraction not influenced by light (LIF). The emission activity factor accounting for the light response of emissions, for each class compound (i), is estimated as

$$\gamma_{P,i} = (1 - LDF_i) + LDF_i \cdot \gamma_{P\_LDF} \quad (35)$$

$$\gamma_{P_{LDF}} = C_P \left[\frac{\alpha \cdot PPFD}{(1 + \alpha^2 \cdot PPFD^2)^{0.5}} \right] \quad (36)$$

$$C_P = 0.0468 \cdot e^{(0.0005 \times [P_{24} - P_s])} \cdot [P_{240}]^{0.6} \quad (37)$$

$$\alpha = 04 - 0.0005 \cdot ln(P_{240}) \quad (38)$$

where:

- **PPFD** is the instantaneous photosynthetic photon flux density [µmol/m^{2}s];
- **Ps** the standard conditions for PPFD averaged over the past day (200 µmol/m^{2}s for sun leaves and 50 µmol/m^{2}s for shade leaves);
- **P_{24}** is the average PPFD of the past 24 hours;
- **P_{240}** is the average PPFD of the past 240 hours.

The MEGAN version 2.04 actually applied in WRF-Chem, calculates the light response emission activity (γ_P) using the sine of the solar angle (equations from 4 to 7) without splitting the light depending fraction from the light independent fraction. The version 2.10 code calculates the γ_P with the photosynthetic photon flux density (PPFD) using the internal variable "swdown": the downward solar radiation [W/m^2]. P_{24} and P_{240} are the average PPFD of the past day and the past ten days, nevertheless, in the code modified, they are both equal to "mswdown" variable: the downward solar radiation [W/m^2] of previous month (Figure 3) (Guenther *et al.*, 2012).

Table 4: Example of the photosynthetic photon flux density and the temperature activity factors calculated by the MEGAN module modified in WRF-Chem for each class compound (PPFD=600 W/m^2; P_{240}=P_{24}=300 W/m^2; T= 293.15 K; T_{240}=T_{24}=288.15 K).

COMPOUND CLASS	$\gamma_{P,i}$	$\gamma_{T,i}$
Isoprene	1.2	0.22
Myrcene	1.1	0.42
Sabinene	1.1	0.42
Limonene	1.0	0.59
3-Carene	1.0	0.59
t-β-Ocimene	1.2	0.33
β-Pinene	1.0	0.59
alfa-Pinene	1.1	0.42
Other Monoterpenes	1.1	0.51
alfa-Farnesene	1.1	0.35
β-Caryophyllene	1.1	0.35
Other Sesquiterpenes	1.1	0.35
232-MBO	1.2	0.26
Methanol	1.2	0.37
Acetone	1.0	0.59
CO	1.2	0.28
Bidirectional VOC	1.2	0.33
Stress VOC	1.2	0.33

Other VOC	1.0	0.59

The updated temperature activity factor (MEGAN v2.10 applied to WRF-Chem), is also the weighted average of a light dependent and independent fraction, calculated as

$$\gamma_{T,i} = (1 - LDF_i) \cdot \gamma_{T\_LIF,i} + LDF_i \cdot \gamma_{T\_LDF,i} \quad (39)$$

$$\gamma_{T_{LDF},i} = E_{opt} \cdot \left[CT_2 \cdot \frac{e^{(CT_{1,i} \cdot x)}}{CT_2 - CT_{1,i} \cdot (1 - e^{(CT_2 \cdot x)})} \right] \quad (40)$$

$$x = \frac{\left[\left(\frac{1}{T_{opt}} \right) - \left(\frac{1}{T} \right) \right]}{0.00831} \quad (41)$$

$$E_{opt} = C_{eo,i} \cdot e^{(0{,}05 \cdot (T_{24} - T_S))} \cdot e^{(0{,}05 \cdot (T_{240} - T_S))} \quad (42)$$

$$T_{opt} = 313 + \left(0.6 \cdot (T_{240} - 297) \right) \quad (43)$$

where:

- $\mathbf{E_{opt}}$ is the maximum normalized emission capacity [mol/Km^2 hr];
- $\mathbf{T_{opt}}$ is the temperature at which $\mathbf{E_{opt}}$ occur [K];
- **T** is leaf temperature [K];
- $\mathbf{CT_{1\text{-}i}}$, $\mathbf{CT_2}$ and $\mathbf{C_{eo\text{-}i}}$ are emission-class dependent empirical coefficient (Table 5);

- $\mathbf{T_s}$ the standard conditions for leaf temperature (= 297 [K]);
- $\mathbf{T_{24}}$ the average leaf temperature of the past 24 hours [K];
- $\mathbf{T_{240}}$ the average leaf temperature of the past 240 hours [K];

On the other hand, the response of the light-independent fraction follows the monoterpene exponential temperature response function by Guenther et al. 1993:

$$\gamma_{T_{LIF,i}} = e^{\left(\beta_i (T - T_S)\right)} \tag{44}$$

where

- $\boldsymbol{\beta_i}$ is an empirically determined coefficient, depending on the emission class compound (Table 5)
- **T** is leaf temperature [K];
- $\mathbf{T_s}$ the standard conditions for leaf temperature (= 297 [K]) (Guenther *et al.*, 2012).

The light dependent equation (40) updated is the equivalent of the MEGAN v2.04 equation 8, currently used on WRF-Chem in order to calculate the isoprene temperature activity factor, while the response of the light-independent fraction equation (44) is used for all the others non-isoprenoid compounds. Additional changes made on this part of the code, consist on the update of the parameters as CT_1, CT_2 and C_{eo}. In the Guenther et al. 2006 their values are respectively 80, 200 and 1.75, in the updated version equation (40) $CT_{1,i}$ and $C_{eo,i}$ depend on the class compound (Table 5), CT_2 still have a fixed value (=230). The way to consider the temperature activity factor as the weighted average of a light dependent and independent fraction ($\gamma_{Ti,LDF}$ and

$\gamma_{Ti,LIF}$) and the update of the model parameters (CT_1, CT_2 and C_{eo}), for each class compound, may lead in a more accurate BVOC evaluation where each class compound has the appropriate value. Note that the value of T_{24} and T_{240} in updated code (MEGAN v2.10 applied to WRF-Chem) is estimate equal to the variable "MTSA" (Figure 3). Therefore, it is assumed that the average temperature of the past 24 hours, and the past ten days, are the same as the average temperature of the past month ($T_{24} = T_{240} =$ "MTSA").

The leaf age emission activity factor (γ_{age}) does not undergo profound changes, MEGAN v2.10 estimates it as the equation 13; even the canopy subdivision into four fractions (new foliage F_{new}, growing foliage F_{gro}, mature foliage F_{mat} and old foliage F_{old}) and their computation (equations from 14 to 25) remain unchanged. The only update of equation parameters, is the relative emission rates assigned to each compound class (A_{new}, A_{gro}, A_{mat}, and A_{old}) reported in the Table 5 (Guenther *et al.*, 2012).

As mentioned above, the soil moisture activity factor (γ_{sm}), in the MEGAN v2.04 used by WRF-Chem, is set to 1.0 for both isoprene and no-isoprene classes compound, so the soil moisture dependence is literally not involved into the BVOC emissions algorithm. The update version of code (MEGAN v2.10 applied to WRF-Chem) uses the equations described before (equation from 29 to 32) for isoprene-emission only, for all other compound classes is still set to 1.0 (Guenther *et al.*, 2006).

The canopy environment coefficient (γ_{CE}) has been also updated from the equation 12 to the following

$$\gamma_{LAI} = LAI \cdot C_{CE} \tag{45}$$

where LAI [m^2/m^2] is the leaf area index referred to the month of the simulation and C_{ce} is a value dependent on the canopy environment model being used. WRF-AQ (Weather Research Forecast – Air Quality) canopy environment model uses a value of 0.57 (Guenther *et al.*, 2012).

Isoprene emission activity can also be influenced by other environmental conditions as carbon dioxide (CO_2) (Velikova *et al.*, 2005). The isoprene emission activity factor associated with the CO_2 inhibition follows Heald et al. 2009 as

$$\gamma_{CO_2,isoprene} = I_{Smax} - \left[\frac{I_{Smax} \cdot (C_i)^h}{(C_*)^h + (C_i)^h}\right] \quad (46)$$

where:

- $\mathbf{I_{Smax}}$, $\mathbf{C_*}$ and **h** are empirically determined coefficients;
- $\mathbf{C_i}$ the internal CO_2 concentration (70% of the ambient CO_2 concentration) [ppm];

Equation 46 is used only to estimate emissions of isoprene, all other BVOC compounds are assigned a value equal to 1 ($\gamma_{CO2,non\text{-}iso}$ =1) (Guenther *et al.*, 2012). That emission activity factor is not calculated in the MEGAN v2.10 applied to WRF-Chem, because at the moment, the calculation of CO_2 concentration is not included in the WRF code ($\gamma_{CO2,iso}$ =1 and $\gamma_{CO2,non\text{-}iso}$ =1). Figure 5 shows how the carbon monoxide [ppm] influences the emissions activity of isoprene ($\gamma_{CO2,iso}$ decreases about 10 % with an increase of 100 ppm of CO_2).

After the update of emission activity factors, as described above, there are other modifications that worth to be mentioned. One change is the update of the PFTs classification: MEGAN v2.04 includes 4 PFTs (Needleleaf Trees, Broadleaf Trees, Broadleaf Shrubs and Grass and other) while MEGAN v2.10 includes 15 PTFs (Needleleaf Evergreen Temperate Tree, Needleleaf Evergreen Boreal Tree, Needleleaf Deciduous Boreal Tree, Broadleaf Evergreen Tropical Tree, Broadleaf Evergreen Temperate Tree, Broadleaf Deciduous Tropical Tree, Broadleaf Deciduous Temperate Tree, Broadleaf Deciduous Boreal Tree, Broadleaf Evergreen Temperate Shrub, Broadleaf Deciduous Temperate Shrub, Broadleaf Deciduous Boreal Shrub, Arctic C3 Grass, Cool C3 Grass, Warm C4 Grass and Crop) (Guenther *et al.*, 2012). The emission factors (ε) [$\mu g/m^2hr$] depends on the PFTs and the biogenic emission classes, thus increasing the number of PFTs, and their relative emission factors, the net biogenic flux to the atmosphere could become more realistic.

In order to increase the PFTs the preprocessor (megan_bio_emiss.tar), and mainly the global input data (megan.data.tar.gz), should be updated since the PFTs sectioning comes from the input file. In this study, only the MEGAN algorithm within WRF-Chem is updated, without changing the database. Table 6 shows the new emission factors [$\mu g/m^2h$] applied, for each plant functional types and biogenic emission classes, based on the Table 2 and Table 3 of Guenther et al. 2012. The updated values used for the four PTFs (Needleleaf Trees, Broadleaf Trees, Broadleaf Shrubs and Grass and other) are the PFTs average values adapted from the Table 2 of Guenther et al. 2012 (i.e. NT = EF_1 to EF_3 avarage value; BT = EF_4 to EF_8 avarage value; SB = EF_9 to EF_{11} avarage value; HB = EF_{12} to EF_{14} avarage value; EF_{15} was not

considerd on the calculation since the small value of the emissions factor for crops).

Table 5: MEGAN v2.1 model parameters used in the updated WRF-Chem code (Guenther *et al.*, 2012).

Compound Class	***β***	**LDF**	***Ct1***	***C*eo**	***A*new**	***A*gro**	***A*mat**	***A*old**
Isoprene	0.13	1	95	2	0.05	0.6	1	0.9
Myrcene	0.1	0.6	80	1.83	2	1.8	1	1.05
Sabinene	0.1	0.6	80	1.83	2	1.8	1	1.05
Limonene	0.1	0.2	80	1.83	2	1.8	1	1.05
3-Carene	0.1	0.2	80	1.83	2	1.8	1	1.05
***t* -*β*-Ocimene**	0.1	0.8	80	1.83	2	1.8	1	1.05
***β*-Pinene**	0.1	0.2	80	1.83	2	1.8	1	1.05
***α*-Pinene**	0.1	0.6	80	1.83	2	1.8	1	1.05
Other Monoterpenes	0.1	0.4	80	1.83	2	1.8	1	1.05
***α*-Farnesene**	0.17	0.5	130	2.37	0.4	0.6	1	0.95
***β*-Caryophyllene**	0.17	0.5	130	2.37	0.4	0.6	1	0.95
Other Sesquiterpenes	0.17	0.5	130	2.37	0.4	0.6	1	0.95
232-MBO	0.13	1	95	2	0.05	0.6	1	0.9
Methanol	0.08	0.8	60	1.6	3.5	3	1	1.2
Acetone	0.1	0.2	80	1.83	1	1	1	1
CO	0.08	1	60	1.6	1	1	1	1
Bidirectional VOC	0.13	0.8	95	2	1	1	1	1
Stress VOC	0.1	0.8	80	1.83	1	1	1	1
Other VOC	0.1	0.2	80	1.83	1	1	1	1

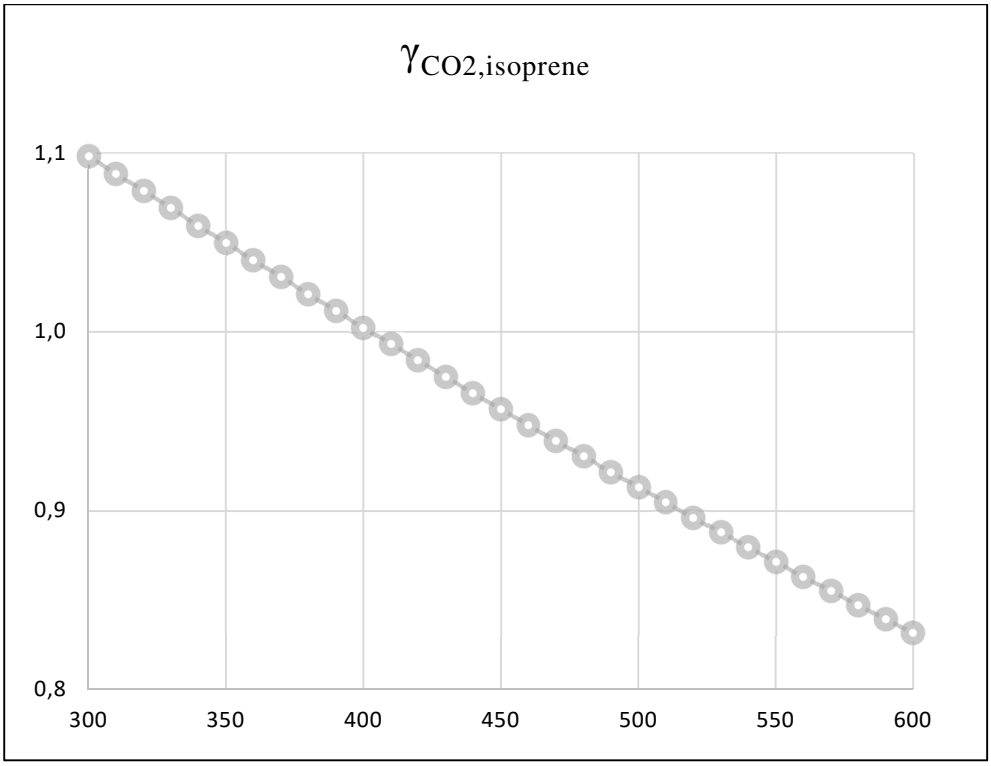

Figure 5: Dependence of the carbon dioxide activity factor for isoprene ($\gamma_{CO2,iso}$) from the CO_2 concentration [ppm] calculated with MEGAN v2.10 algorithm (Guenther *et al.*, 2012).

The PFTs update does not change the isoprene emission, its emission factors are estimated directly from the input database. Conclusively, the last change made in the code has been to compute the isoprene emission factor within the MEGAN emission algorithm (equation 34), instead of reading it directly from the input database ("msebio_isop" variable in "wrfbiochemi" file) (Figure 3).

Table 6: Biogenic emission classes and emission factors (new and old)[µg/m²h] for each plant functional types updated to MEGAN v2.10 applied to WRF-Chem (Guenther *et al.*, 2012).

	BT_old	BT	NT_old	NT	SB_old	SB	HB_old	HB
Isoprene	13000	9000	2000	1800	11000	3333	400	866
Myrcene	20	50	75	70	22	36	0.3	0.3
Sabinene	45	62	70	70	50	56	0.7	0.7
Limonene	45	80	100	100	52	73	0.7	0.7
3-Carene	18	34	160	160	25	53	0.3	0.3
t-β-Ocimene	90	132	60	70	85	110	1	2
β-Pinene	90	126	300	300	100	116	1.5	1.5
alfa-Pinene	180	480	450	500	200	233	2	2
Other Monoterpenes	90	150	180	180	110	140	4.8	5
alfa-Farnesene	35	48	30	40	30	40	0.50	3
β-Caryophyllene	30	48	60	80	45	50	0.90	1
Other Sesquiterpenes	75	108	110	120	85	100	1.40	2
232-MBO	0.1	0.41	100	380	1	0.01	0.01	0.01
Methanol	800	740	800	900	800	900	800	500
Acetone	240	240	240	240	240	240	80	80
CO	1000	600	1000	600	1000	600	1000	600
Bidirectional VOC	1000	500	1000	500	1000	500	1000	80
Stress VOC	1000	280	1000	300	1000	300	1000	300
Other VOC	1000	140	1000	140	1000	140	1000	140

2.2.2. European case of study: domain and simulations settings

The BVOC emissions influence the ozone distribution on the whole European continent that tends to increase in the summer periods, playing a fundamental role in the photochemistry of the polluted boundary layer (Solmon *et al.*, 2004). The connection between the biogenic emissions, and the formation of ozone, is the reaction between nitrogen oxides (NO_X = NO + NO_2) and volatile organic compounds (VOC). The ozone formation is favored by high temperatures: the highest concentrations are found in areas characterized by high pressure, clear sky and warm temperatures. While most of the NO_x emissions in Europe may be associated with anthropogenic sources, VOC formation is thought to be associated with emissions from plants and forests (BVOC).

In order to evaluate the updates of the MEGAN code described in the previous section, it has been carried out a study, at European level, focuses on a reference period of 6 days (from August 10th - 00:00 UTC to August 16th - 00:00 UTC, 2015) characterized by particularly high ozone concentration episode. The choice of this period was made by examining the hourly average ozone concentrations for all the air-quality monitoring stations of the Marche region (Italy) (Figure 6), over a period of 3 years (from 2013 to 2015), just considering the summer time measurements: from May to September. The analysis results have indicated that 2015 presents an extraordinary event which did not occur on the previous years. On August 13th, all the air quality stations have reported the highest ozone hourly average concentration value of the year.

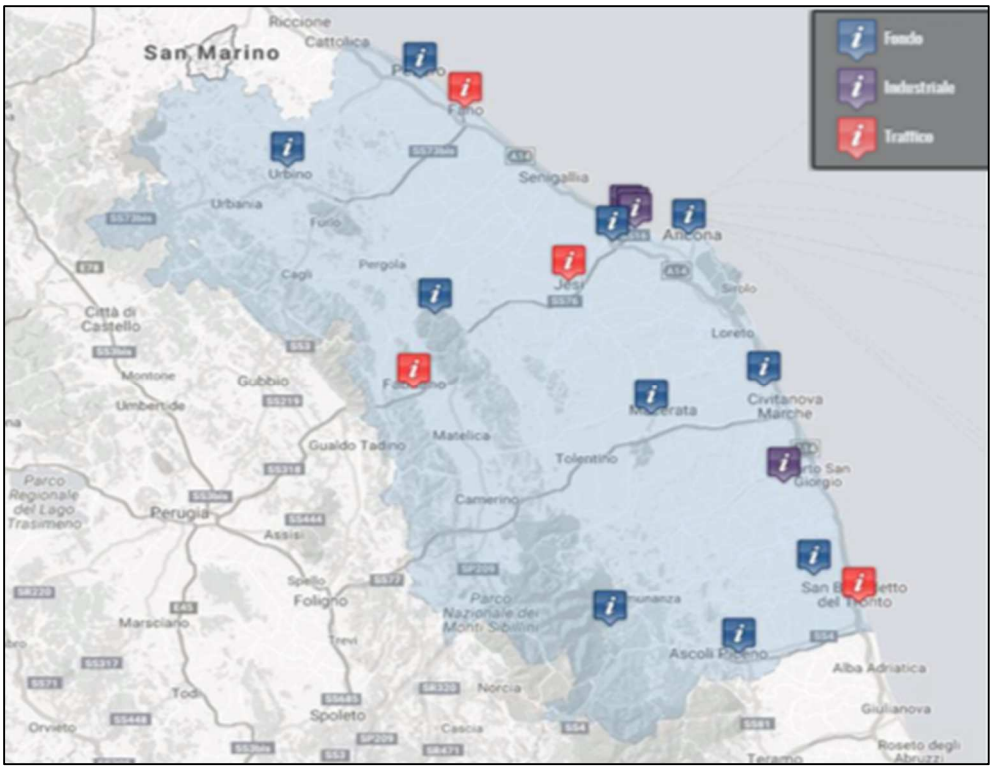

Figure 6: Marche region (Italy) quality monitoring stations analyzed in the 3 years study. The colors represent the surface station type: the blue one is for background stations; the purple denotes the industrial type and the red is for the traffic stations (http://94.88.42.232:16382 - ARPAM).

Due to the deleterious effects of ozone on humans and vegetation, European legislation has regulated the assessment of its air concentration limits; Italy transposed the directive by Legislative Decree n. 155/2010. The Decree reports the target value, the information threshold and the alarm threshold ozone concentration with the respectively value of 120 µg/m³ (about 61 ppbv) (eight-hours average), 180 µg/m³ and 240 µg/m³ (respectively about 91 and 122 ppbv) (hourly average) ("Decreto Legislativo 13 agosto 2010, n.

155", 2010). Figure 7 displays the O_3 hourly average development for eleven, of the eighteen Marche region air quality surface stations, during the week from August 10th to 17th, 2015. The central peak corresponds to the August 13th and the red line indicates the information threshold ("soglia di informazione") of 180 µg/m³.

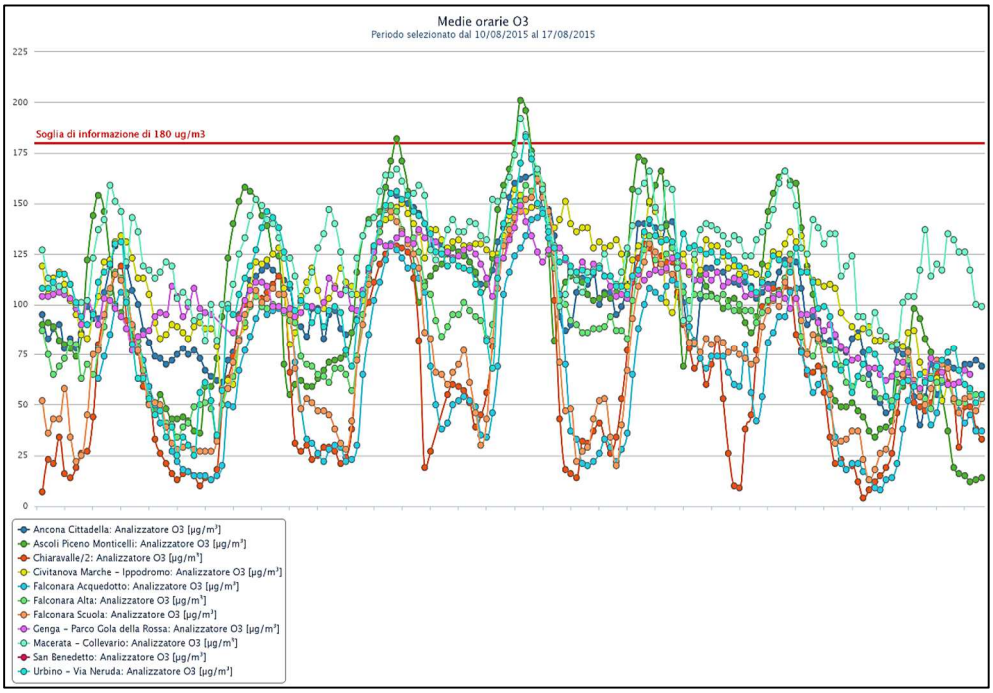

Figure 7: Ozone hourly average increase during the period from August 10th to 17th, 2015. In the legend the surface stations used for the plot, all of them, are part of the Marche region quality monitoring stations of Figure 6 (http://94.88.42.232:16382 - ARPAM).

For this study, the WRF-Chem version 3.9 was used and Figure 8 shows the model domains. The coarse domain covers all Europe, and the western part of Russia, with 380×360 grid points centered at 50° N, 15° E (12

km grid cells), while the nested domain is centered over Italy with 355×355 grid points and 4 Km grid cells. Both, domains include 40 vertical levels up to 50 hPa. As described from the analysis in the previous paragraphs, the simulations lasted 6 days, from August 10th (00:00 UTC) to August 16th (00:00 UTC), 2015. Boundary and initial conditions were extracted from NCAR/NCEP Final Analysis Operational Global Analysis (FNL from GFS - ds083.2), with a 1° grids resolution and are prepared operationally every six hours (Ncep, 2000).

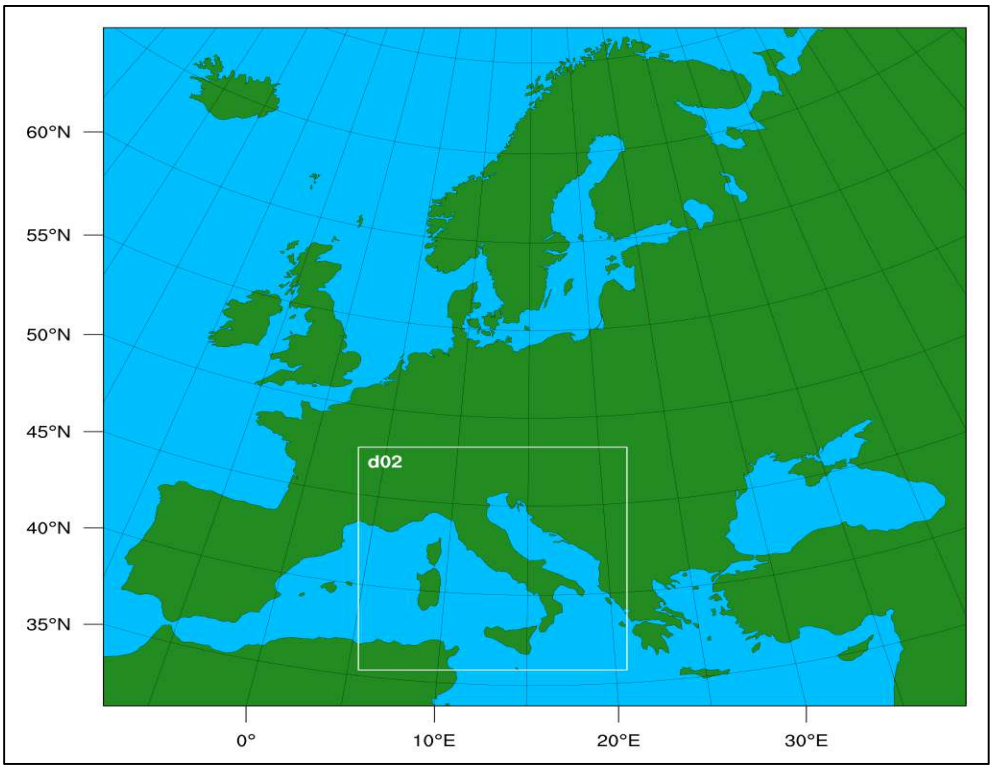

Figure 8: The numerical domains of the simulations: the coarse domain has 380×360 grid points with 12 km grid cells, the nested domain, with 4 km grid cells, has 355×355 grid points.

As summarized in Table 7, the following physical schemes are used. The Morrison double-moment scheme (mp_physics=10) is adopted for the treatment of the microphysics processes (Morrison, Thompson and Tatarskii, 2009). The Rapid Radiative Transfer Model (RRTMG), for both shortwave (ra_sw_physics = 4) and longwave (ra_lw_physics = 4) radiation is used for the aerosol direct radiative effect (Iacono *et al.*, 2008) to represent scattering and absorption in the atmosphere. The Mellor-Yamada-Janjic (MYJ) parameterization (bl_pbl_physics = 2) is considered to describe the planetary boundary layer (Janjić, 1994). The unified Noah land-surface model (sf_surface_physics = 4) is chosen to represent the land surface interaction. It includes soil temperature and moisture in four layers, fractional snow cover and frozen soil physics. Finally, the Grell-Freitas scheme (cu_physics = 3) is considered for the cumulus parameterization scheme: it tries to smooth the transition to cloud-resolving scales (Grell and Freitas, 2014).

The WRF-Chem chemical mechanism selected, in order to investigate the role of isoprene on the high ozone event recorded on the central Europe, is the chemical option (chem_opt = 201) with MOZART (Model for Ozone and Related chemical Tracers – version 4) (Emmons *et al.*, 2010), for the trace gases portion, and MOSAIC (Model for Simulating Aerosol Interactions and Chemistry) (Zaveri *et al.*, 2008) for the aerosol-phase species. Chemical boundary data, for both gas and aerosol fraction, were provided through the MOZBC preprocessor (MOZART Boundary Conditions) and the EDGAR-HTAP (Emission Database for Global Atmospheric Research) emission

inventory for Europe developed by Janssens-Maenhout et al. 2012 provide the anthropogenic emissions. The biomass burning emissions are from the database FINN (Fire Inventory from NCAR) (Wiedinmyer *et al.*, 2011) and the biogenic emissions come from the MEGAN database (Guenther *et al.*, 2006).

Table 7: Namelist settings of the physical parameterizations used in the WRF-Chem setup simulations.

	Number and option variable		Model scheme
Microphysics	10	mp_physics	Morrison two moment
Longwave radiation	4	ra_lw_physics	RRTMG
Shortwave radiation	4	ra_sw_physics	RRTMG
PBL model	2	bl_pbl_physics	MYJ
Surface similarity	2	sf_sfclay_physics	Monin-Obukhov (Janjic Eta)
Land surface	2	sf_surface_physics	Unified Noah land-surface
Cumulus parameterization	3	cu_physics	Grell-Freitas

Table 8 lists the four simulations conducted in order to study the MEGAN updating described above. The first one is the control one, (1) the MEGAN database has been used without any change, then we have the first update, where all (2) the activity factors (γ) have been modified following the MEGAN v2.10 of Guenther et al. 2012. The third simulation (3) adds the

PFTs emission factors changes to the activity factors, (4) the last one calculates more the isoprene emission factor within the equation 34.

Table 8: The four simulations done with the relative updates for the European case study (from August 10th - 00:00 UTC to August 16th - 00:00 UTC, 2015).

MEGAN updates simulations	
Megan without modifications	**Megan_V2.04**
Megan with activity factors modified (γ_i)	**Megan_Gamma**
Megan with activity factors modified (γ_i) and PFTs emission factors update	**Megan_GammaPFT**
Megan with activity factors modified (γ_i), PFTs emission factors update and isoprene emission factor by the MEGAN algorithm	**Megan_GammaPFTISO**

2.2.3. NOMADSS field campaign: domain and simulations settings

The Nitrogen, Oxidants, Mercury and Aerosol Distributions, Sources and Sinks (NOMADSS) project integrates the objectives from three NSF (National Science Foundation) funded projects: SOAS (Southern Oxidant and Aerosol Study), NAAMEX (North American Airborne Mercury Experiment) and TROPHONO (Photolysis of Particulate Nitrate: a Daytime HONO Source and a Re-NOx-ification Pathway in the Troposphere). These three projects have been merged onto the C-130 (NCAR aircraft platform for the NOMADSS airborne component) as a means to complete all three projects in the same year and to increase the scientific value of the joint experiment. The NOMADSS primary objective are: the quantification of biogenic emissions and their interactions with anthropogenic pollutants (SOAS), the distribution and the chemical transformations of speciated mercury in the troposphere (NAAMEX) and the investigation of the role of particulate nitrate photolysis in the cycling of reactive nitrogen species in the troposphere (TROPHONO) (NOMADSS - Operational plan, 2013).

NOMADSS took place over the southeastern United States from June 1st to July 15th, 2013. The NCAR C-130 aircraft base was the Smyrna/Rutherford County Airport in Tennessee (36.00° N, 86.52° W - KMQY), which is located approximately 20 km southeast of Nashville. Because of the range of scientific objectives, NOMADSS had 10 different flight patterns. Flight tracks for NOMADSS has covered much of the eastern United States, this included a north-south section from Michigan to Florida, and an east-west extent from the North Atlantic to western Oklahoma (Figure

9). The C-130 is configured primarily to quantify fluxes, transformations and distributions of VOC, Ozone, NOx, mercury and HONO, according with the main objectives of the entire project (NOMADSS - Operational plan, 2013).

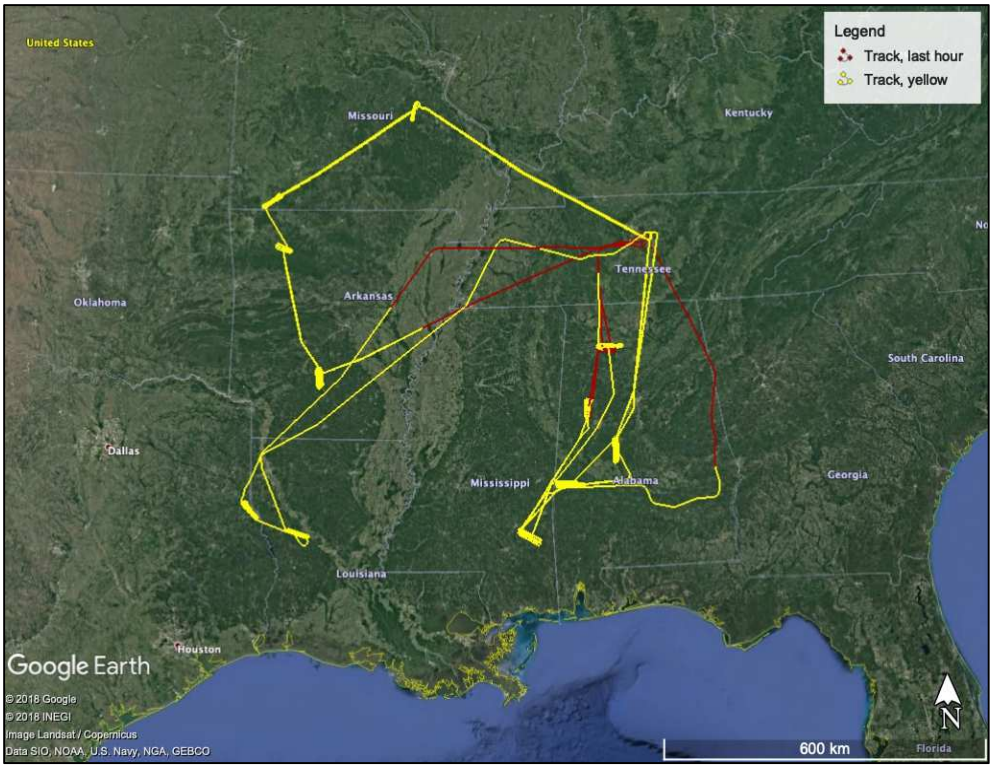

Figure 9: NOMADSS track flights example. Displayed the flight tracks referred to first step of the project: the quantification of biogenic emissions and their interactions with anthropogenic pollutants (Flight codes: from rf01 to rf05 – Flight dates: from 03/6/13 to 14/6/13).

The NOMADSS field campaign includes 19 flights (rf01 - rf19) (Table 10) from June 3rd to July 14th, 2013. From those flights, the first five (rf01 – rf05) (SOAS-NOMADSS) were chosen to estimate and evaluate the updates of the MEGAN code within the WRF-Chem model. In agreement with the study at European level, the WRF-Chem version 3.9 was used; Figure 10 shows the model domains. The coarse domain has 442×265 grid points with 12 Km grid cells centered at 40° N 97° W, covering all United States (CONUS domain – SW corner 22.83° N 120.49° W; NW corner 52.46° N 136.45° W; NE corner 45.98° N 60.82° E; SE corner 20.08° N 81.24 W). The nested domain is centered over the southeastern area of the United States with 301×301 grid points and 4 Km grid cells including the selected NOMADSS flight tracks (rf01 - rf05) inside the simulation domain. Both domains consider 40 vertical levels up to 50 hPa. The simulations lasted 14 days, from June 1st (00:00 UTC) to June 15th (00:00 UTC), 2013; the simulations started two days before the first flight (rf01 - June 3rd) so as to guarantee a spin up for the model and the simulation integration period is to the first five NOMADSS flights (rf01: 03/6/13 - rf02: 05/6/13 - rf03: 08/6/13 - rf04: 12/6/13 - rf05: 14/6/13). In order to consider the flight tracks, the "tracking" option (track_loc_in > 2) was selected in WRF-Chem; the option writes the vertical profiles of prescribed meteorological and chemical species at a set of prescribed times and horizontal coordinates, described in a file (wrfinput_track.txt), to a special output file (wrfout_track_d<nn>).

Meteorological boundary and initial conditions were extracted from NCEP North American Regional Reanalysis (NARR – ds608.0): the NARR project is an addition of the NCEP global reanalysis which is run only over the North American Region with the high resolution of NCEP eta model (32km horizontal resolutions with 45 horizontal layer) (NCAR, 2005). The configuration of the physical and chemical/aerosol schemes used for this part of the study is similar to that described in the previous section and reported to Table 7. Chemical boundary data for gas and aerosol were provided from the global chemistry transport model MOZART v4 using the MOZBC preprocessor to interpolate to the WRF grid. The 2011 National Emissions Inventory (NEI) provides the anthropogenic emissions, while the biomass burning emissions and the biogenic emissions come from FINN (Wiedinmyer et al., 2011) and MEGAN databases (Guenther et al., 2006, 2012), respectively.

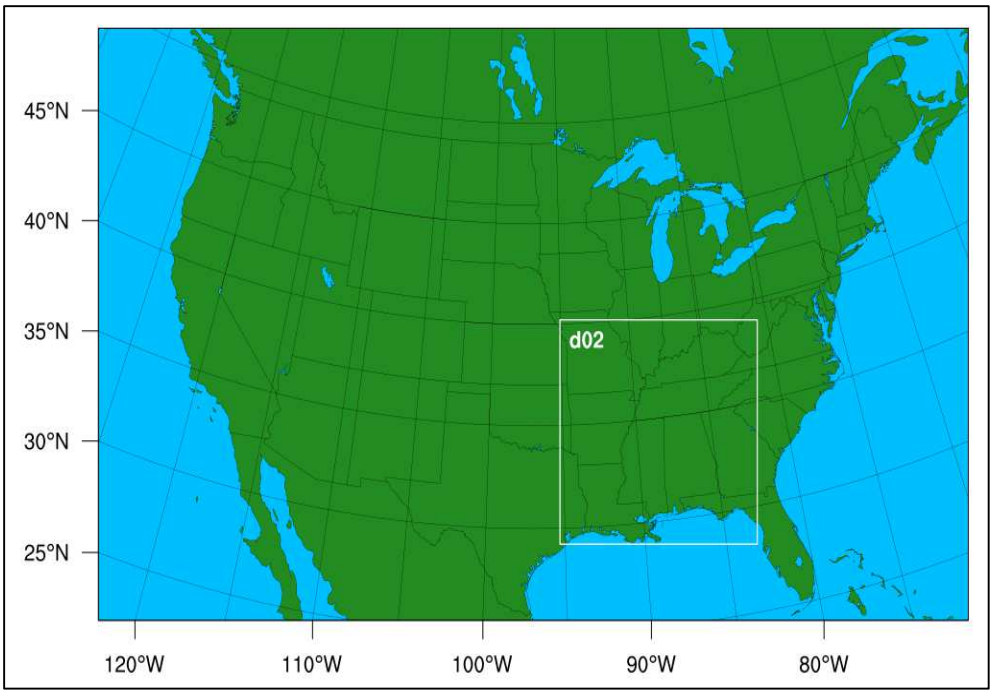

Figure 10: The numerical domains of the NOMADSS simulations: the coarse domain has 442×265 grid points with 12 Km grid cells, the nested domain, with 4 Km grid cells, has 301×301 grid points.

Table 9: The two simulations done with the relative updates for the NOMDASS fields campaign (from June 1st - 00:00 UTC to June 15th - 00:00 UTC, 2013).

MEGAN updates simulations	
Megan without modifications	**Megan_V2.04**
Megan with activity factors modified (γ_i), PFTs emission factors update and isoprene emission factor by the MEGAN algorithm	**Megan_GammaPFTISO**

Table 10: Start-end dates and times [UTC Time] of the 19 NOMADSS flights. The first 5, from rf01 to rf05, are the flight tracks analyzed (http://catalog.eol.ucar.edu/sas/tools/missions).

Flt	Start Date/Time	End Date/Time
rf01	03/6/13 14:00	03/6/13 18:34
rf02	05/6/13 14:44	05/6/13 21:30
rf03	08/6/13 14:06	08/6/13 21:05
rf04	12/6/13 15:14	12/6/13 22:28
rf05	14/6/13 15:05	14/6/13 21:31
rf06	19/6/13 14:59	19/6/13 22:08
rf07	20/6/13 16:29	20/6/13 23:38
rf08	22/6/13 15:16	22/6/13 22:15
rf09	24/6/13 15:09	24/6/13 22:21
rf10	27/6/13 15:03	27/6/13 21:53
rf11	29/6/13 15:20	29/6/13 21:02
rf12	01/7/13 14:14	01/7/13 21:22
rf13	04/7/13 15:19	04/7/13 22:09
rf14	05/7/13 15:08	05/7/13 21:44
rf15	07/7/13 15:11	07/7/13 22:01
rf16	08/7/13 15:04	08/7/13 21:48
rf17	11/7/13 15:08	11/7/13 21:57
rf18	12/7/13 20:32	13/7/13 03:37
rf19	14/7/13 14:05	14/7/13 21:08

Table 9 lists the two simulations setting done in order to evaluate the update on the MEGAN model compared with the measurements of the NCAR C-130 flight tracks. In this case, two simulations are done: in the first one the MEGAN v2.04 database has been used without any change, while the second one considers all the code updates described previously (all the activity factors modified, the activity factors updated follow the PFTs emission factors changes and the isoprene emission factor is considered as the emission factor of all the other compound classes) (Guenther et al. 2012).

2.3. Results evaluation

2.3.1. Main objectives

Isoprene, and more generally the biogenic volatile organic compounds, play an important role in driving the atmosphere photochemistry and may contribute significantly to severe ozone events (Trainer *et al.*, 1987; Chameides *et al.*, 1988; Solmon *et al.*, 2004). Despite the past works put in setting up accurate biogenic emission inventories (e.g. MEGAN and BEIS), uncertainties in European scale biogenic emission estimates remain large, i.e. with a factor of 3–5 for compound as isoprene (Simpson *et al.*, 1999; Curci *et al.*, 2009). Global emissions, of volatile organic compounds from vegetation, account for about 1150 million tons carbon per year [TgC/yr], corresponding to about the total global VOC emissions, even including the anthropogenic sources (Guenther *et al.*, 1995; Curci *et al.*, 2009).

Once in the atmosphere, depending on the presence of carbon monoxide (CO) and in particular on the presence of nitrogen oxides (NO_x), the oxidation of these VOCs produces variable amounts of ozone and secondary organic aerosol (SOA). Therefore, while these compounds influence substantially the atmosphere chemistry, the BVOCs modeling present some significant gaps: they have an high sensitivity to environmental parameters, as temperature and solar radiation, vegetation type and leaf area index (i.e. land use and land cover changes) (Guenther *et al.*, 1995). Kuhlmann *et al.*, 2004, show that, based on different modelling scenarios, the uncertainty of the effect of isoprene on the global tropospheric ozone burden ranges between -35% and +35%, with even greater local variations. Others

several modelling studies, carried out at a regional scale and compared with field campaigns, highlighted the important role of biogenic emissions even in an urbanized landscape during specific air pollution events (Duane *et al.*, 2002; Derognat *et al.*, 2003; Solmon *et al.*, 2004; Liu *et al.*, 2007). One of the key features from these measurements is that abundant anthropogenic NO_x sources in some of these areas boost the oxidation of highly reactive BVOCs. Consequently the episodic contribution to ozone production from biogenic sources, could be as high as 50–75% in Northern Italy (Curci *et al.*, 2009).

As mentioned in the section 2.2.2 and 2.2.3, the main goal is an evaluation of the impact of biogenic VOC emissions on ozone levels over Europe (principally in Italy) and the southeastern area of U.S. This will be realized utilizing a set of simulations with high spatial resolution (12 km coarse domain - 4 km nested domain), considering a sensitivity study on the MEGAN database, in order to understand how the updates made in the biogenic volatile organic compound emission algorithms (from MEGAN v2.04 by Guenther *et al.*, 2006 to MEGAN v2.10 by Guenther *et al.*, 2012) changes the WRF-Chem capability to calculate trace gases concentrations (ozone, nitrogen oxides and carbon monoxide).

2.3.2. Ozone event description: synoptic conditions

The meteorological parameters have been obtained from the NCEP/NCAR reanalysis project (https://www.esrl.noaa.gov/psd/data/). The database uses an analysis-forecast system to perform data assimilation using past data from 1948 to the present. A large subset of this data is available 4 times daily format (0Z, 6Z, 12Z, and 18Z), as daily averages and monthly value. The resolution of the data is about 2.5° x 2.5° horizontal grids, with global coverage and 17 pressure levels (1000, 925, 850, 700, 600, 500, 400, 300, 250, 200, 150, 100, 70, 50, 30, 20, 10 hPa) for the vertical grid (Kalnay *et al.*, 1996).

The averaged geopotential height map at 850 hPa (five-days average: from August 10th 00:00 UTC to 16th 00:00 UTC) (Figure 11), shows the presence of an intense high-pressure (1520-1580 m) affecting the central part of the Mediterranean basin. The ridge separates a pressure minimum (1300-1340 m) over northwestern Europe from a weak depression (1460-1500 m) over Turkey. As a consequence, central and southern Europe are affected by northeasterly currents from north Europe, that permits the weak depression to cross Italy toward the southeast portion of the domain. The WRF-Chem simulations appear consistent with the evolution represented in the reanalysis, although some slight differences emerge. In particular, the pressure low is more intense in the WRF-Chem runs and the high-pressure crossing Italy is more intense in the NCAR/NCEP reanalysis. The visual differences can be partially explained considering that the coarse reanalysis shown (horizontal resolution of 2.5° × 2.5°) differ from the finer-resolution operational analysis used to force the model (12 km grids).

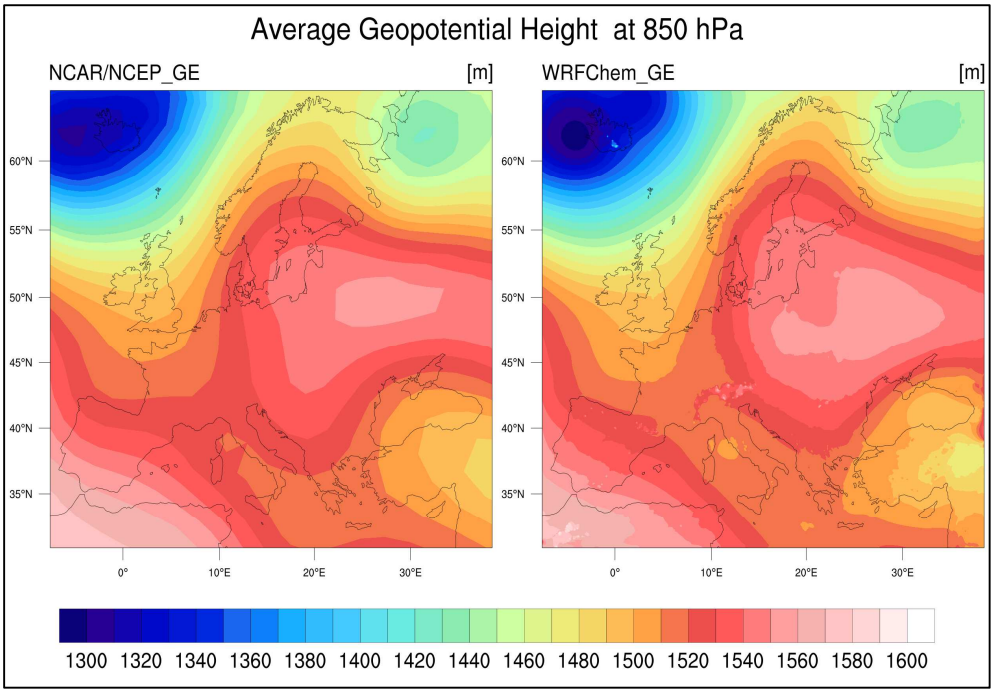

Figure 11: Weekly average of geopotential height (August 10th -15th, 2015) at 850 hPa. Comparison between the NCAR/NCEP reanalysis (horizontal resolution of 2.5° × 2.5°) and the WRF-Chem results on the coarse domain (380×360 grid points - 12 Km grid spacing) [m].

The five-day average temperature analysis (Figure 12) shows that the mean temperature, and its spatial tendency, are well represented by the model. The temperature starts from the northwestern Europe area (Iceland) with about 5-10° C, increases in the northeasterly direction with a temperature of about 10-15° C covering most part of England and the Scandinavian Peninsula. Along the central part of Europe, the temperature increases more up to 15-25° C (Portugal, Spain, French, Germany etc.), while Italy and the southeast portion of Europe (Croatia, Albany, Yugoslavia, Greece, Turkey

etc.) have the highest temperatures at about 30-35° C. There is marginally different spatial trend between WRF-Chem and the reanalysis, however, both maps showed the same increasing temperature trend confirming that the northeast side has observed lower temperature as compared to other Europe areas. Obviously, the WRF-Chem model map (fig.15b) is more detailed, mainly for the resolution difference between the NCAR/NCEP reanalysis (fig.15a) and 12 km WRF-Chem coarse domain grid.

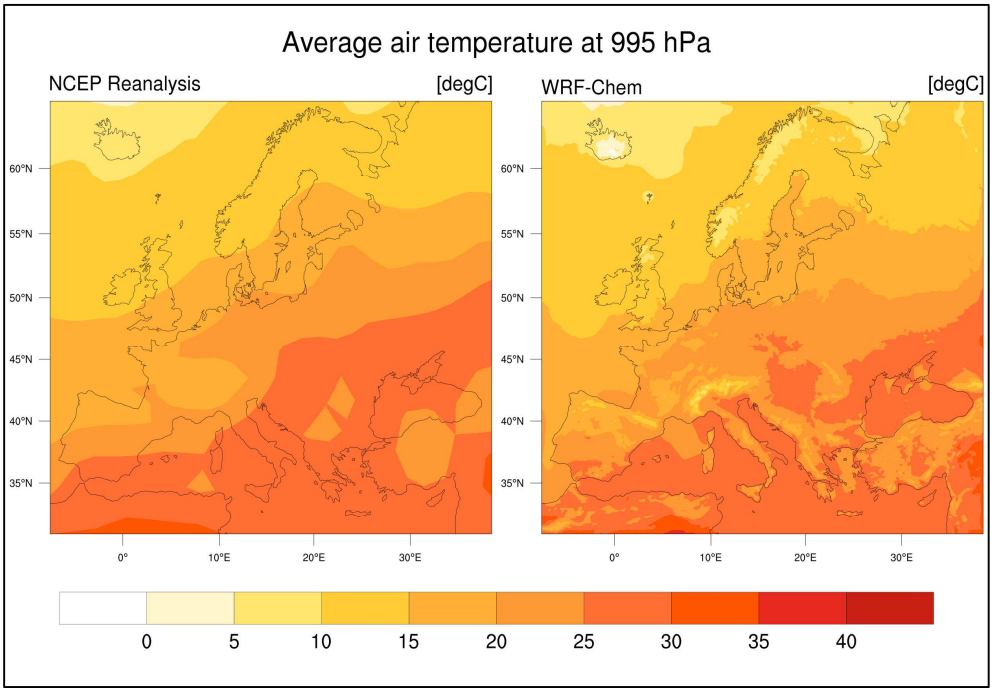

Figure 12: Spatial variability of mean weekly temperature for August 10th -15th, 2015 at 995 hPa. Comparison between the NCAR/NCEP reanalysis (horizontal resolution of 2.5° × 2.5°) and the WRF-Chem results on the coarse domain (380×360 grid points - 12 Km grid cells).

2.3.3. Ozone event description: biogenic emissions

The trace gas (NO_x, CO and O_3) concentration analysis, for the European region (from August 10th 00:00 UTC to 16th 00:00 UTC, 2015), includes two main steps: the first one concerns (1) an evaluation of the differences on BVOC emissions considering the updates described above for the MEGAN emissions algorithm; and the second one is (2) the comparison of the different simulation concentration outputs with an experimental dataset. The second step is divided into two phases: (2-a) a statistical analysis based on the calculation of mean-bias, correlation coefficient and normalized root mean square error, and a (2-b) further assessment of the spatial distribution of the NO_x, CO and O_3 concentrations.

Figure 14 displays the time series of isoprene emission [mol/km^{2}hr] during the simulation at four European cities with the MEGAN algorithm variations. The blue lines represent the control simulation (MEGAN version 2.04 by Guenther *et al.*, 2006), the black lines indicate the first update, where all the activity factors (γ_i) have been adapted following the MEGAN version 2.10 of Guenther et al. 2012. The red lines are representative of the activity factors updates (emission factors relative to PFTs), and green lines represent the last simulations where isoprene emission factor is calculated as the emission factor of all the other compound classes (equation 34) (in MEGAN version 2.04 the isoprene is calculated from the "wrfbiochemi" by the variable "MSEBIO_ISOP"). The emission points chosen are Porto, Portugal (41.15° N – 8.63° W), Genoa, Italy (44.40° N – 8.95° E), Zagreb, Croatia (45.80° N – 16° E) and Kiev, Ukraine (50.45° N – 30.50° E) (Figure 13).

Figure 13: The emission points selected: Porto, Portugal (41.15° N – 8.63° W), Genoa, Italy (44.40° N – 8.95° E), Zagreb, Croatia (45.80° N – 16° E) and Kiev, Ukraine (50.45° N – 30.50° E).

Isoprene emission development (Figure 14) represents clearly its diurnal cycle thus, the six days of the simulations: the emission peaks (day time) are staggered with the phases (night time) in which there are no emissions. The black lines are not showed since it is overlapped by the red lines, i.e. "Megan_Gamma_PFT" simulation does not have effect because the isoprene emission factor is a value originates from the MEGAN database directly, this is why the "Megan_Gamma_PFTISO" simulation it has been prepared. All the city-points analyzed (Porto, Genoa, Zagreb and Kiev) demonstrate how the isoprene emissions increase significantly. The features of MEGAN algorithm that creates the major gap are the emission activity factors (γ_i), the value is about 90 mol/km^{2}hr in the first day and 30 mol/km^{2}hr for all other days in Porto city; Genoa, Zagreb and Kiev have a gap more

constant, respectively about 30-60, 90-100 and 10-30 mol/km^2 hr (red lines). The isoprene emission values related to the last simulations ("Megan_Gamma_PFTISO") are approximately half of the previous values gap (15-45 mol/km^{2}hr – Porto; 15-30 mol/km^{2}hr – Genoa; 45-50 mol/km^{2}hr – Zagreb; 5-15 mol/km^{2}hr – Kiev). This result means that the isoprene emission factor calculated with the MEGAN algorithm is generally less than the emission factor database values.

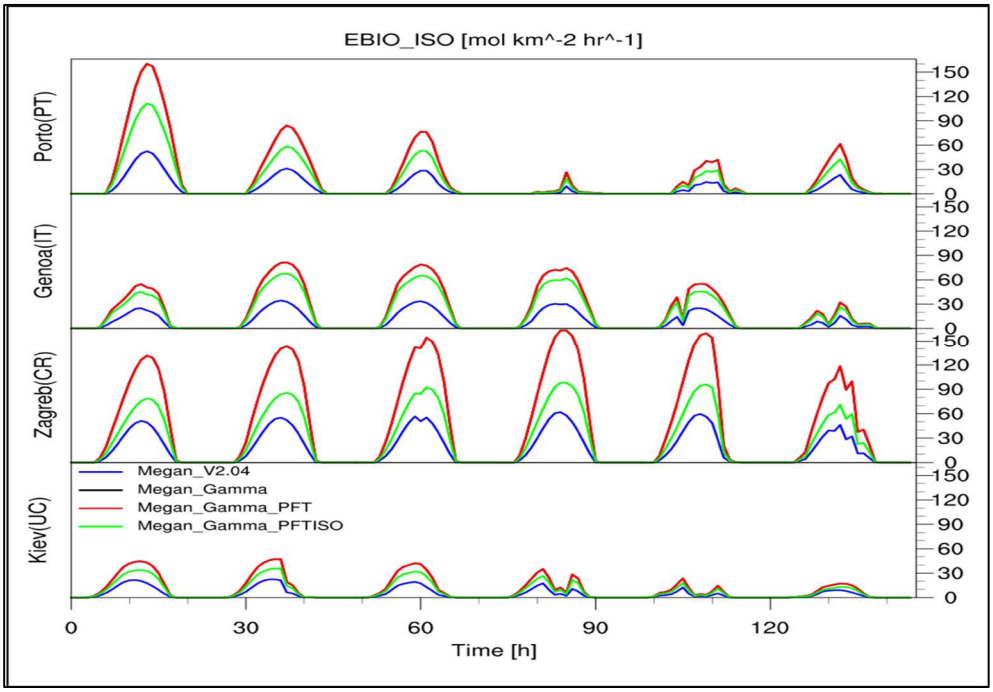

Figure 14: Time series of isoprene emission [mol/km^{2}hr] for different MEGAN algorithm configurations. The blue lines represent the control simulation (Megan_V2.04), the black lines indicate the activity factors (γ_i) updates (Megan_Gamma), the red lines are representative of the PFTs emission factors updates (Megan_Gamma_PFT) and green lines show the isoprene emission factor as the emission factor of all the other compound classes (Megan_Gamma_PFTISO). The emission points are Porto (41.15° N – 8.63° W, Portugal), Genoa (44.40° N – 8.95° E, Italy), Zagreb (45.80° N – 16° E, Croatia) and Kiev (50.45° N – 30.50° E, Ukraine). In the x-axis the time of the simulations in hours (145 hours).

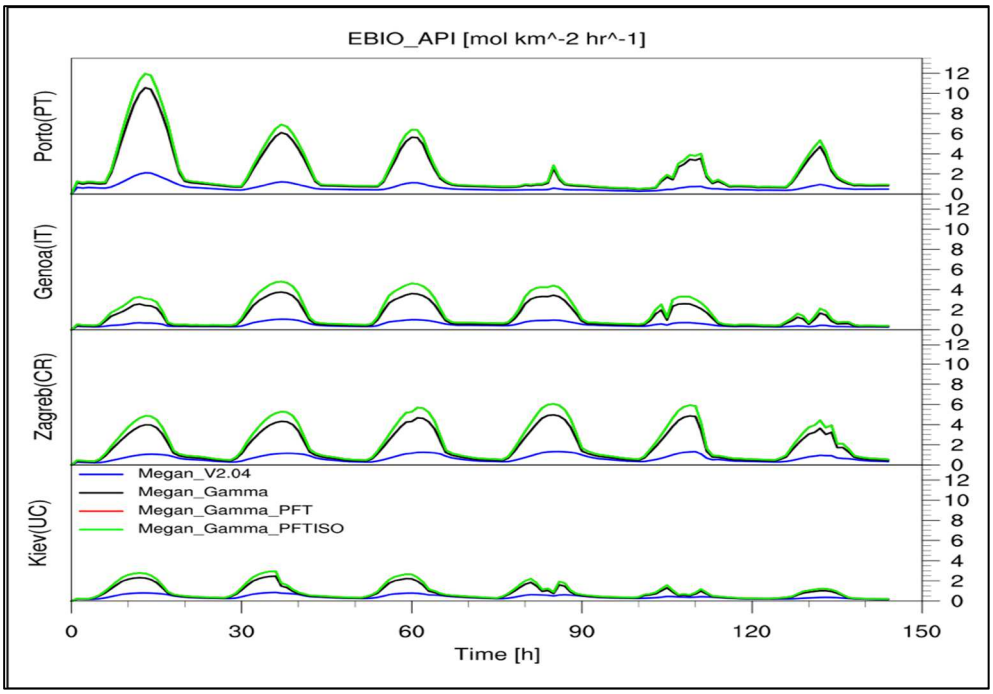

Figure 15: Time series of α-pinene emission [mol/km²hr] for different MEGAN algorithm configurations. The blue lines represent the control simulation (Megan_V2.04), the black lines indicate the activity factors (γ_i) updates (Megan_Gamma), the red lines are representative of the PFTs emission factors updates (Megan_Gamma_PFT) and green lines show the isoprene emission factor as the emission factor of all the other compound classes (Megan_Gamma_PFTISO). The emission points are Porto (41.15° N – 8.63° W, Portugal), Genoa (44.40° N – 8.95° E, Italy), Zagreb (45.80° N – 16° E, Croatia) and Kiev (50.45° N – 30.50° E, Ukraine). In the x-axis the time of the simulations in hours (145 hours).

The α-pinene (representative of terpenes) emission (Figure 15) shows a similar diurnal pattern as isoprene, but with an order of magnitude lower. In this case the red lines are not displayed because they are covered by the green lines, as the last code change takes effect only for the isoprene emissions ("Megan_Gamma_PFTISO"). In general, the emission values increase, from the control simulation ("Megan_V2.04"), by a value from 0.5 (Kiev – 5th day)

to 10 mol/km^{2}hr (Porto – 1st day). There are not remarkable differences between the simulation "Megan_Gamma" and "Megan_Gamma_PFTISO", the gap is about 1-2 mol/km^{2}hr, meaning that the updates made for the emission factor values, for each plant functional type (PFTs), do not change the final results substantially (black lines and green lines - Figure 15).

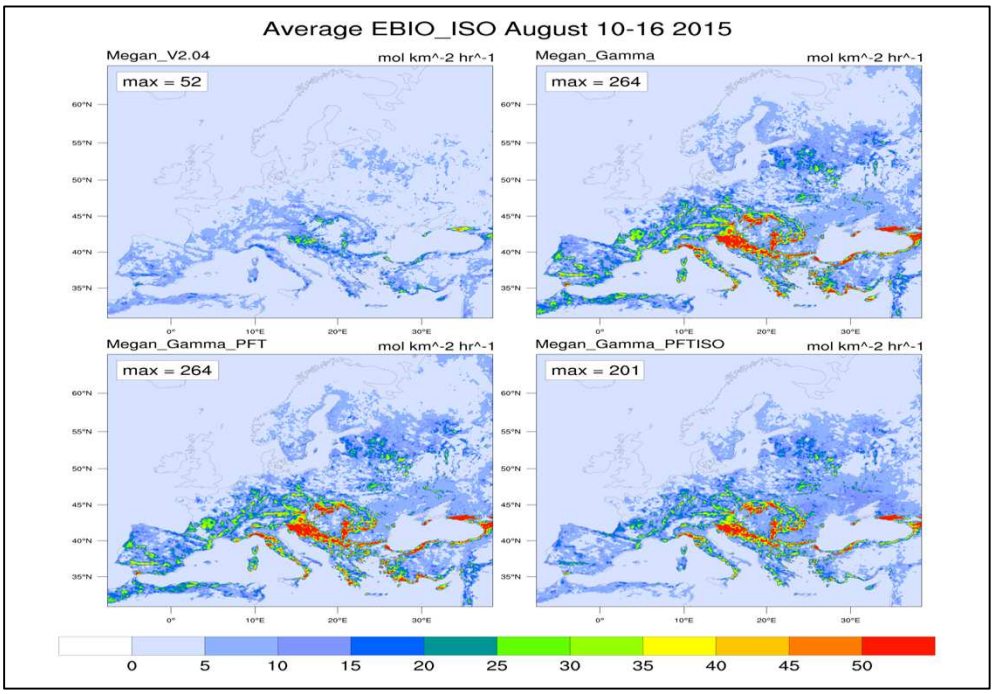

Figure 16: The spatial distribution of isoprene emission calculated as weekly average (from August 10th 00:00 UTC to 16th 00:00 UTC, 2015) for the different MEGAN configurations: control simulation (Megan_V2.04), activity factors (γ_i) updated (Megan_Gamma), PFTs emission factors updated (Megan_Gamma_PFT) and the isoprene emission factor updated (Megan_Gamma_PFTISO) (12 km x 12 km resolution).

Figure 16 and Figure 17 illustrate the spatial distribution of the BVOC emissions calculated with different MEGAN configurations, respectively for

isoprene and α-pinene emissions, as the weekly average emission flux (from August 10th 00:00 UTC to 16th 00:00 UTC, 2015) in the main domain of simulations (12 km x 12 km resolution). As described above, the changes to the MEGAN algorithm cause a significant increase in BVOC emissions. Observing the maps, the portion where emissions have a major increase is the Balkan Peninsula, the Apennine Mountain (Italy), and the Black Sea border (Turkey and Georgia) (from 15-25 to 50 mol/km^{2}hr for isoprene emissions; from 0.5-1.5 to 5 mol/km^{2}hr for α-pinene emissions). The Iberian Peninsula and central-east Europe show a minor difference, but still noteworthy (from 15-25 to 25-35 mol/km^{2}hr for isoprene; from 0.5-1.5 to 2.5-3.5 mol/km^2 hr for α-pinene).

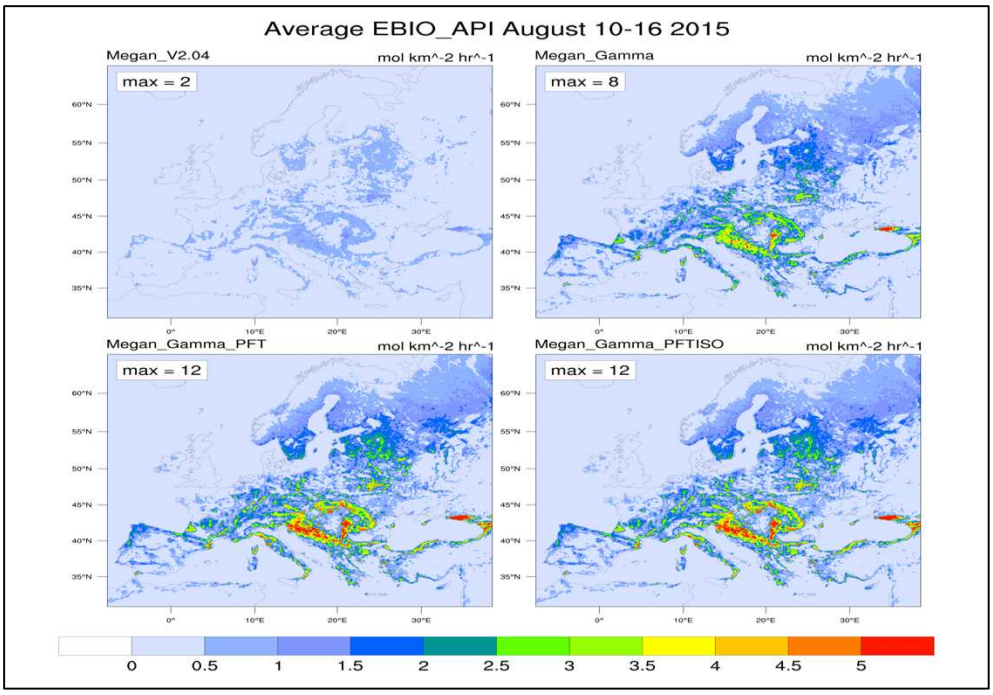

Figure 17: The spatial distribution of α-pinene emission calculated as weekly average (from August 10th 00:00 UTC to 16th 00:00 UTC, 2015) for the different MEGAN configurations: control simulation (Megan_V2.04), activity factors (γ_i) updated (Megan_Gamma), PFTs emission factors updated (Megan_Gamma_PFT) and the isoprene emission factor updated (Megan_Gamma_PFTISO) (12 km x 12 km resolution).

The PFTs percentage coverage (Figure 18), shows a high frequency of Needleleaf trees in northeastern Europe (Sweden, Finland, Lithuania, Latvia, Estonia and the north of Russia) with a values between 30-70 % and, with more staggered trend, in the north of Spain and Italy, Germany and in the most part of Balkans peninsula (i.e. from west to east along the mountain ranges of Cantabrian Mountains, Alps and Carpathian Mountains); the Broadleaf coverage has a similar comportment to the Needleleaf trees, but with a definitely lower values (from 10 to 40 %). The Shrub PFT is predominant in the arid areas as: Norway, north of Russia, southeastern part

of Spain, north Africa and Turkey, and finally, the Herbs covers the greatest number of central Europe countries with a very high percentage (from 70 to 100 %), since there are a substantial amount of plants that fall within that plant functional type (Grass and other - PFTP_HB). The isoprene emitting genera in this category include: Phragmites (a reed), Carex (a sedge), Stipa (a grass) and Sphagnum (a moss) (Guenther *et al.*, 2006).

Coming back to the BVOC emissions (Figure 14, Figure 15, Figure 16 and Figure 17), the city-point analyzed with the highest emission values is Zagreb followed by the city of Porto, Genoa and Kiev. This sorting highlights the strictly correlation between the biogenic emissions and the PFTs coverage. Zagreb and Porto areas are covered mainly by Needleleaf trees and Shrubs categories (the emission factor values for isoprene are, respectively: 1800 and 3333 $\mu g/m^2h$); Genoa has a prevalence of Broadleaf trees with an isoprene emission factor of 9000 $\mu g/m^2h$, and finally Kiev, with the lowest results, is mainly covers by the Herbs type with an isoprene emission factor of 866 $\mu g/m^2h$.

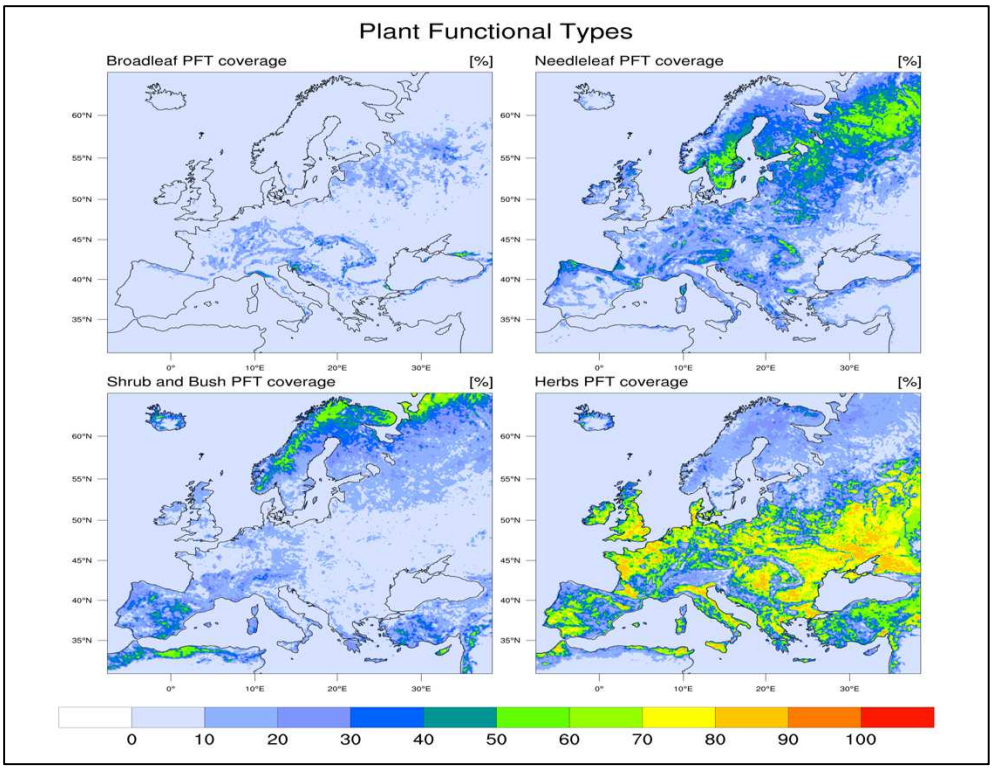

Figure 18: Percentage coverage [%] of plant functional type (PFTs) classification included into MEGAN database, computed on August 2015. Clockwise from the upper left picture: coverage of Broadleaf Trees (PFTP_HB), Needleleaf Trees (PFTP_NB), Grass and Other (PFTP_HB) and Broadleaf Shrubs (PFTP_SB).

After the evaluation above, is clear the various updates to the MEGAN equations cause a substantial increase in BVOC emissions; the algorithm change that creates the major gap is the emission activity factors update (γ_i) (Figure 14 and Figure 15) there is, therefore, a need for in deepen evaluation of those factors. Figure 19 represents the comparison of the emission activity factors γ_P, γ_T, γ_{age}, and γ_{LAI} (respectively accounts for photosynthetic photon flux density, temperature, leaf age and leaf area index) concerning MEGAN

version 2.04 (Guenther *et al.*, 2006) (green lines) and version 2.10 (Guenther *et al.*, 2012) (red lines). The factors are referred to the city of Genoa (44.40° N – 8.95° E; Figure 13) for August 13th (12:00 UTC), 2015 (Appendix A. 1, Appendix A. 2 and Appendix A. 3 show the emission activity factors, respectively, for Kiev, Porto and Zagreb). The overview picture is clear, the new emission activity factors are substantially higher than the previous MEGAN version; considering the emission factor for Genoa (Figure 19) the PPFD factor (γ_P - GAMMA_P) has an increment on average about 0.6 (e.g. isoprene = 1, α-pinene = 0.6). The light dependence (γ_T - GAMMA_T) parameter is more variable than the PPFD factor, but the result is similar: the average increment is about 0.3. The leaf age emission activity factor (γ_{age} - GAMMA_A) does not has profound changes, because its equation (equations from 14 to 25) remain unchanged between the two MEGAN versions; the only update of equation parameters, is the relative emission rates assigned to each compound class (A_{new}, A_{gro}, A_{mat}, and A_{old}) reported in the Table 5. Finally, the LAI (leaf area index) emission activity factor (γ_{LAI} - GAMMA_LAI) has a constant increase of factor 2 (about 0.80).

The Figure 20 shows the total emission activity factors between version 2.04 (green lines) and version 2.10 (red lines) of MEGAN equation. The factors are referred, clockwise from upper-left plot, to the city of Genoa (Italy), Kiev (Ukraine), Zagreb (Croatia) and Porto (Portugal), as the previous plot also this is for August 13th (12:00 UTC), 2015. The emission activity values shown cannot do anything else but confirm the state of Figure 19, they have increased significantly with an average value of about: 3 (Genoa), 0.45 (Kiev), 0.6 (Porto) and 3 (Zagreb).

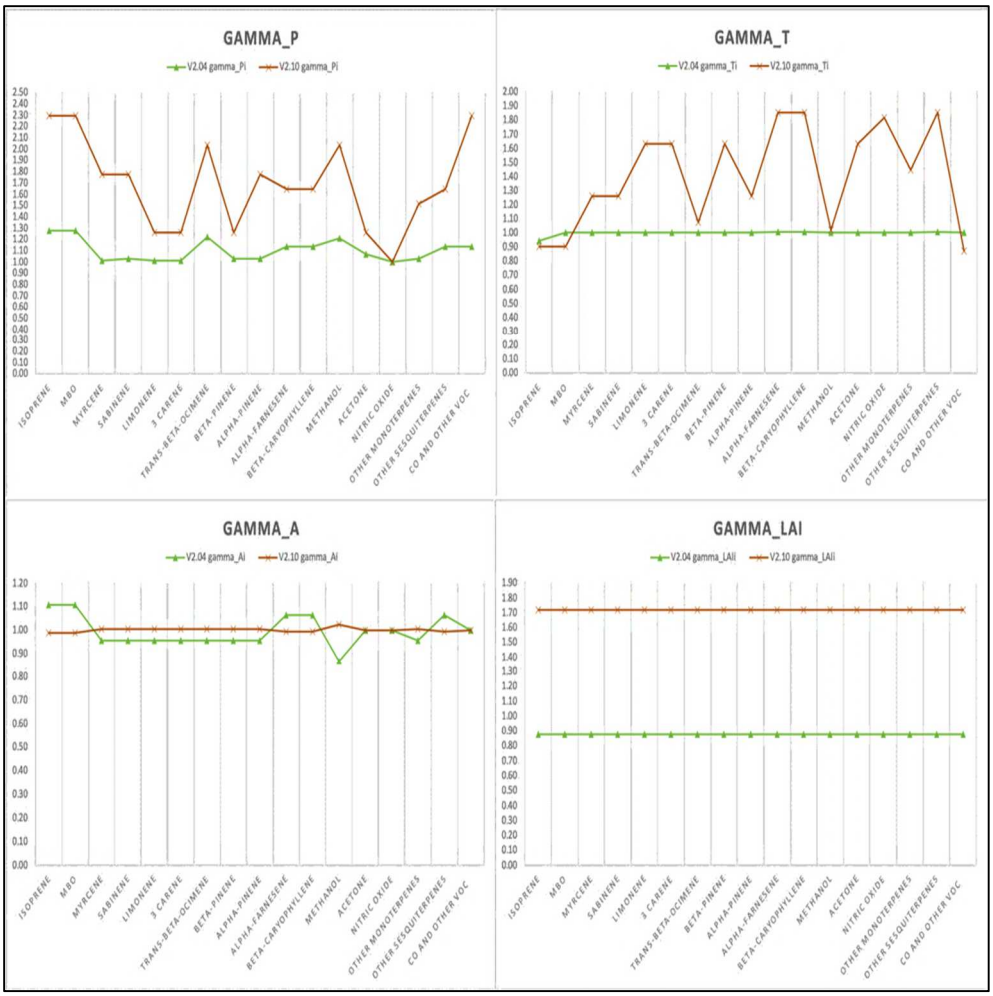

Figure 19: The comparison of the emission activity factors γ_P (GAMMA_P), γ_T (GAMMA_T), γ_{age} (GAMMA_A), and γ_{LAI} (GAMMA_LAI) between version 2.04 and version 2.10 of MEGAN equation, classified by classes compound (x-axis). The factors are referred to the city of Genoa (44.40° N – 8.95° E) for August 13th (12:00 UTC), 2015.

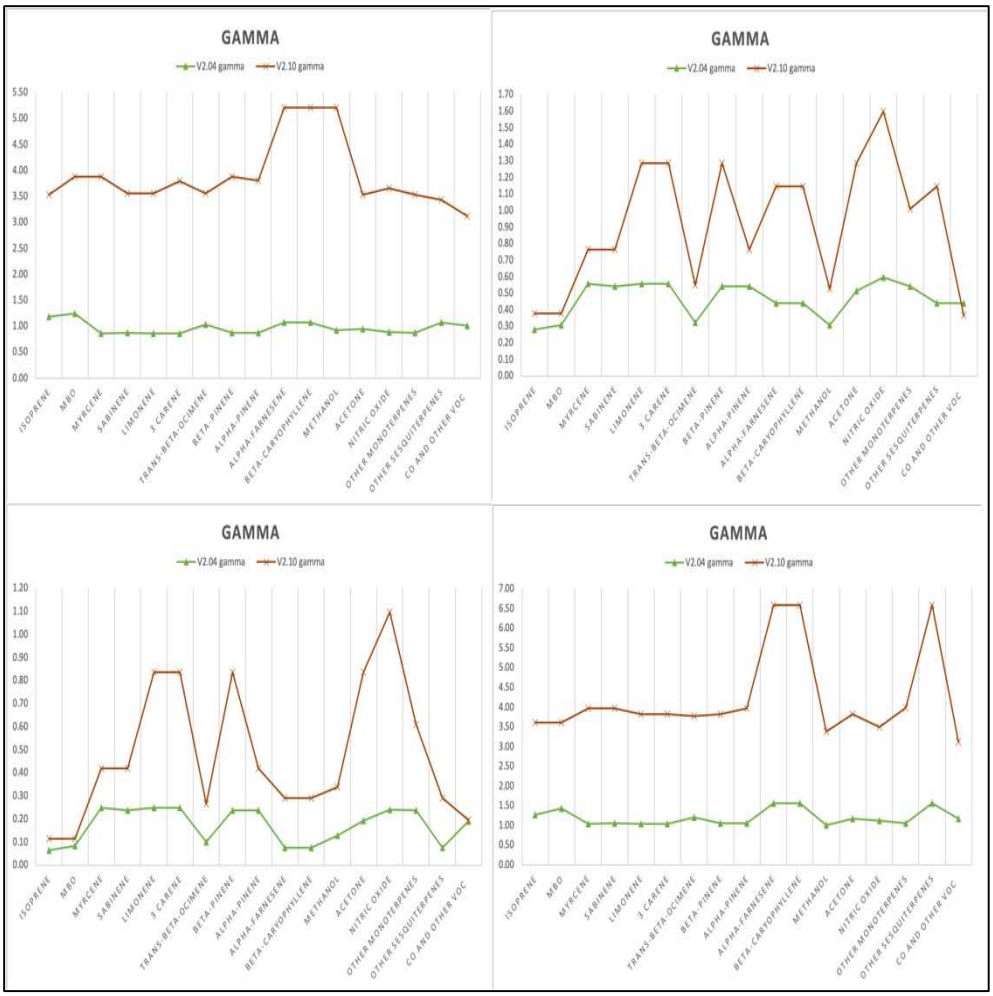

Figure 20: The comparison of the total emission activity factor between version 2.04 and version 2.10 of MEGAN equation. The factors are referred, clockwise from upper-left plot, to the city of Genoa (44.40° N – 8.95° E, Italy), Kiev (50.45° N – 30.50° E, Ukraine), Zagreb (45.80° N – 16° E, Croatia) and Porto (41.15° N – 8.63° W, Portugal) for August 13th (12:00 UTC), 2015.

2.3.4. Ozone event description: gas-phase

The experimental dataset retrieved to analyze the interaction between the BVOC emissions and the gas trace compounds as ozone and its precursors (carbon monoxide and nitrogen dioxide) is the AIRBASE database (European AIR quality dataBASE, https://www.eea.europa.eu/data-and-maps/data/aqereporting-8). The EEA's (European Environment Agency) air quality database consists of a multi-annual (2013-2015) time series of air quality measurement data and calculated statistics for a number of air pollutants. It also contains meta-information on the monitoring networks involved, their stations and measurements, as well as air quality zones. About 3000 surface units have been analyzed from the database (34 nations across the Europe - Figure 21) considering the pollutants as ozone (O_3), carbon monoxide (CO) and nitrogen dioxide (NO_2). Since discrepancies between modeled and measured values might be related to the type and location of a measurement station, the selected stations were also disaggregated into categories based on the study done by Henne *et al.*, 2010, which includes a more complete analysis of the surroundings of each station. The "alternative classification", explained in the Supplement S3 in Henne *et al.*, 2010, provides three class station types: urban, suburban and rural surface stations. Urban means a continuously built-up urban area (buildings with at least two floors), the built-up area is not mixed with non-urbanized areas; suburban area is largely built-up urban area, it means, contiguous settlement of detached buildings of any size, the built-up area is mixed with non-urbanized areas (e.g. agricultural, lakes, woods). All areas, that do not achieve the criteria for urban

or suburban areas, are defined as rural areas (Henne *et al.*, 2010; Knote *et al.*, 2011).

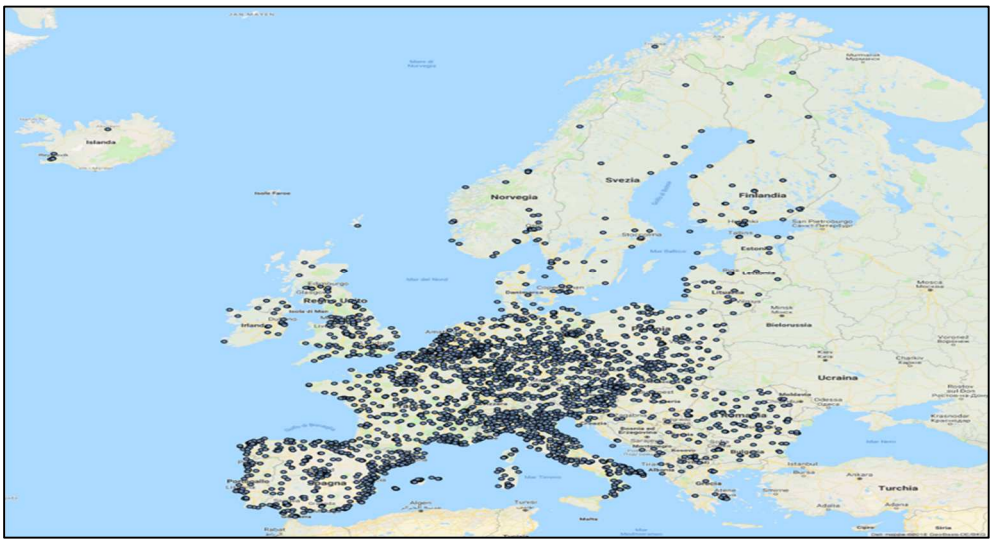

Figure 21: Surface station positions (about 3000) used to retrieve the trace gases compounds concentrations. The states included in the analysis are 34: Albania, Andorra, Austria, Belgium, Bulgaria, Croatia, Czech Republic, Denmark, Estonia, Finland, France, Germany, Greece, Hungary, Iceland, Ireland, Italy, Latvia, Lithuania, Montenegro, Netherlands, Norway, Poland, Portugal, Romania, Serbia, Slovakia, Slovenia, Spain, Sweden, Switzerland, Macedonia, United Kingdom and Hungary.

The second step was to calculate the distribution of averaged pollutant concentrations at all stations in the model domain over the simulations period (from August 10th 00:00 UTC to 16th 00:00 UTC, 2015). For each station the weekly mean of the values was calculated by means of the daily hours (from 7:00 am to 6:00 pm UTC time), after that the mean biases, the normalized root means square error and the coefficient correlation was calculated for the all compounds considered (O_3, NO_2 and CO) classified by the different station classes (urban, suburban and rural stations).

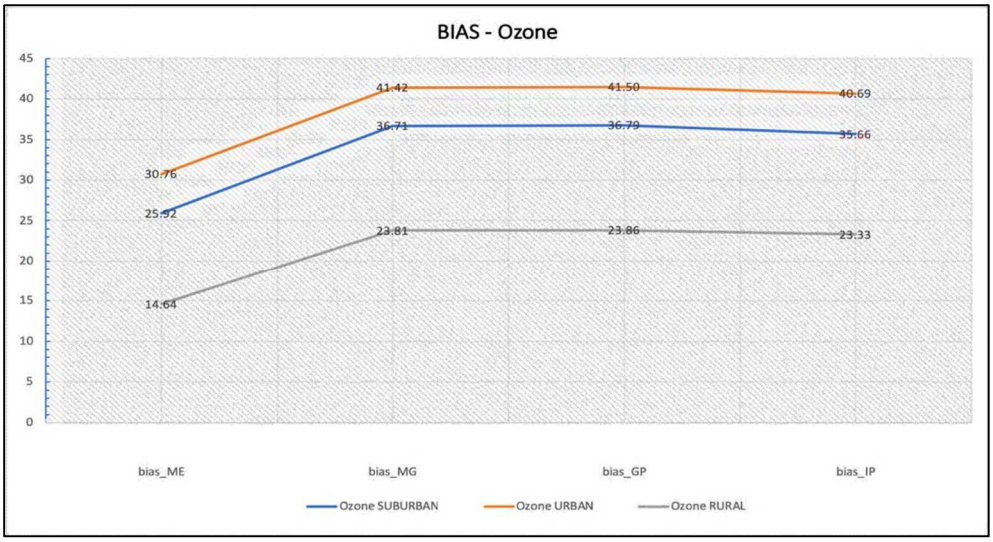

Figure 22: Ozone normalized mean bias [%] for AIRBASE datasets and WRF-Chem model (ME = "Megan_V2.04"; MG = "Megan_Gamma"; GP = "Megan_Gamma_PFT"; IP = "Megan_Gamma_PFTISO").

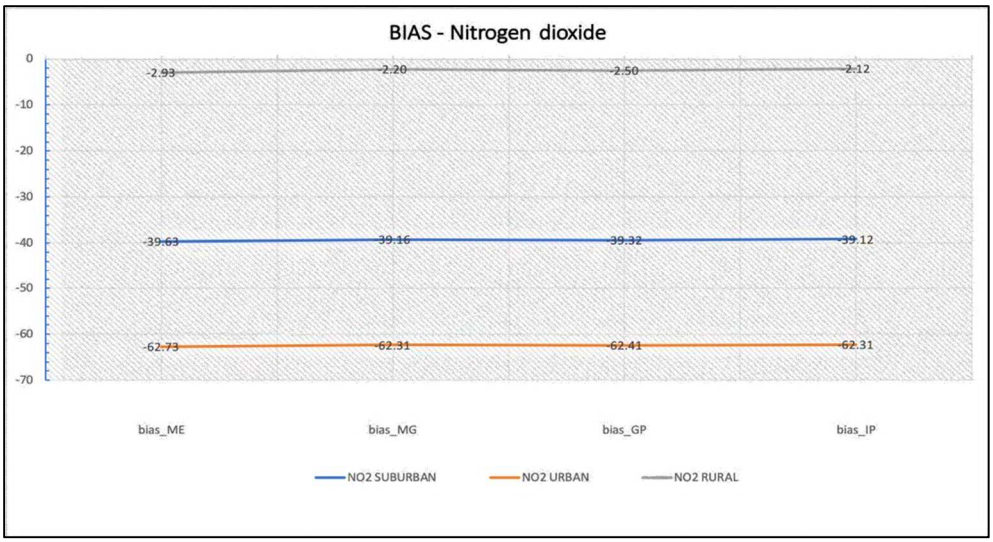

Figure 23: Nitrogen dioxide normalized mean bias [%] for AIRBASE datasets and WRF-Chem model (ME = "Megan_V2.04"; MG = "Megan_Gamma"; GP = "Megan_Gamma_PFT"; IP = "Megan_Gamma_PFTISO").

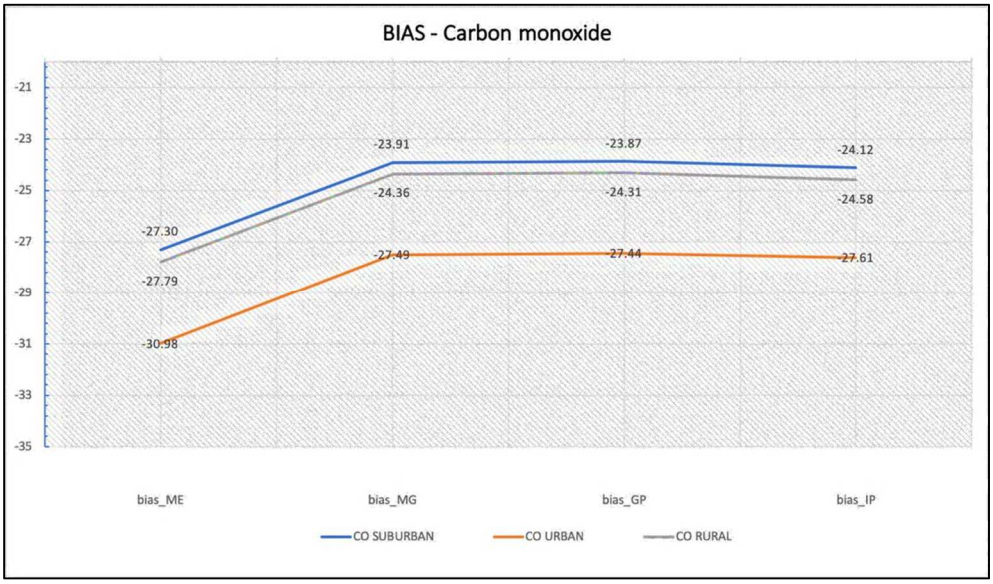

Figure 24: Carbon monoxide normalized mean bias [%] for AIRBASE datasets and WRF-Chem model (ME = "Megan_V2.04"; MG = "Megan_Gamma"; GP = "Megan_Gamma_PFT"; IP = "Megan_Gamma_PFTISO").

The ozone bias values fall within a range between 14.64 – 41.50% (Figure 22) highlighting a consistent model overestimation. The ozone concentrations in the rural area presents the lowest (positive) biases ("Megan_V2.04" = 14.64 %; "Megan_Gamma" = 23.81 %; "Megan_Gamma_PFT" = 23.86 %; "Megan_Gamma_PFTISO" = 23.33 %), while the highest (positive) values come from the urban scenario ("Megan_V2.04" = 30.76 %; "Megan_Gamma" = 41.42 %; "Megan_Gamma_PFT" = 41.50 %; "Megan_Gamma_PFTISO" = 40.69 %).

The result for the ozone highlighted that the MEGAN updates made in WRF-Chem code increase the mean biases by about 10 % regardless of the type of station studied. The nitrogen dioxide (Figure 23) in the urban scenario presents the highest (negative) mean biases showing a greatly underestimate of the model ($NO_{2,urban}$ = from -62 %); in the other stations type there is a greatly improvement from about -39 %, of the suburban area, up to -2.50 % of the rural stations. Finally, the carbon monoxide (Figure 24) means biases show a very limited (negative) variation, all the simulations have the values including in an interval that goes from -27 to -30 %. Other than the stations type classification, the most important thing to underline is that changes to the MEGAN algorithm have a small to negligible effect on NO_2 and CO (i.e. only carbon monoxide has an increase of 3 %, from the control simulation to the others concerning the updates).

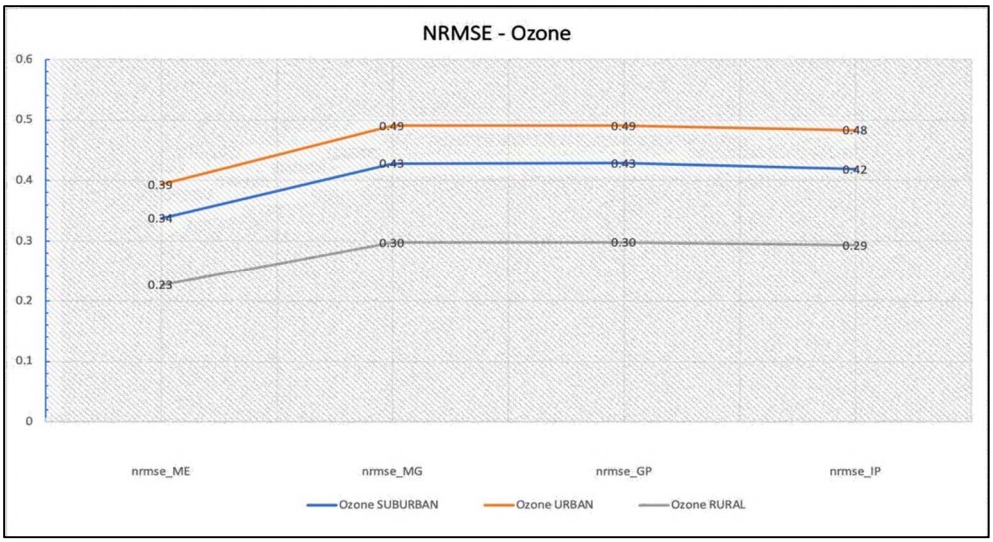

Figure 25: Ozone normalized roots mean square errors [dimensionless] concerning AIRBASE datasets and WRF-Chem model (ME = "Megan_V2.04"; MG = "Megan_Gamma"; GP = "Megan_Gamma_PFT"; IP = "Megan_Gamma_PFTISO").

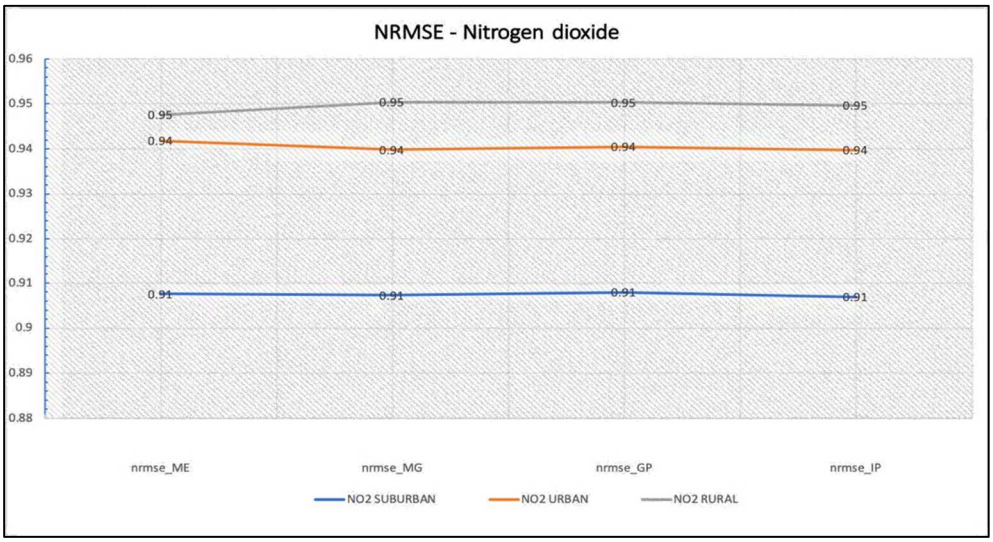

Figure 26: Nitrogen dioxide normalized roots mean square errors [dimensionless] concerning AIRBASE datasets and WRF-Chem model (ME = "Megan_V2.04"; MG = "Megan_Gamma"; GP = "Megan_Gamma_PFT"; IP = "Megan_Gamma_PFTISO").

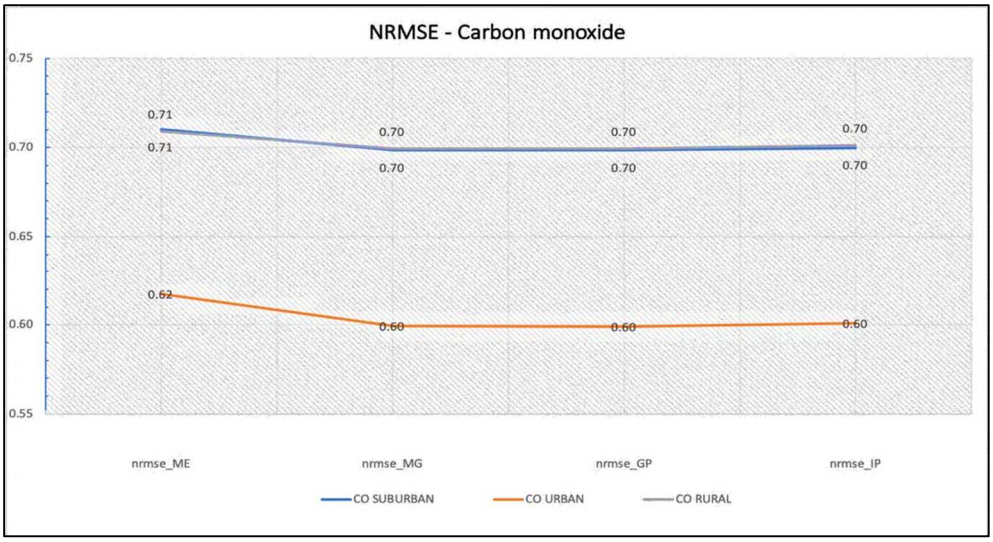

Figure 27: Carbon monoxide normalized roots mean square errors [dimensionless] concerning AIRBASE datasets and WRF-Chem model (ME = "Megan_V2.04"; MG = "Megan_Gamma"; GP = "Megan_Gamma_PFT"; IP = "Megan_Gamma_PFTISO").

The normalized root means square error (NRMSE) between the AIRBASE dataset and the model results has been computed and presented in Figure 25, Figure 26 and Figure 27, respectively, for Ozone, Nitrogen dioxide and Carbon monoxide. Ozone concentration model outputs, for rural stations (grey line), has the best fit, since they have the lowest NRMSE values ("Megan_V2.04" = 0.23; "Megan_Gamma" = 0.30; "Megan_Gamma_PFT" = 0.30; "Megan_Gamma_PFTISO" = 0.29); minimal differences exist between the NRMSE of the control simulation compared to the simulations completed to test the MEGAN code updates (i.e. 0.7). Considering the others station types the situation is almost the same but shifted up about of 0.10 - 0.15. Carbon monoxide NRMSE (Figure 27) is in a range between 0.60 - 0.71, where all the simulations for all type of stations are included; same situation

is for NO_2, the only variance is they have higher NRMSE values (Figure 26) (from 0.91 to 0.95). The last two compounds examined, do not have differences concerning the MEGAN configurations, NO_2 has a constant value for each of the station type (i.e. NO_2-$_{SUB}$ = 0.91, NO_2-$_{URB}$ = 0.94 and NO_2-$_{RUR}$ = 0.95), while CO has a NRMSE decrease of 0.1 from the control simulation (nrmse_ME - "Megan_V2.04") and the others (nrmse_MG - "Megan_Gamma"; nrmse_GP - "Megan_Gamma_PFT"; nrmse_IP - "Megan_Gamma_PFTISO").

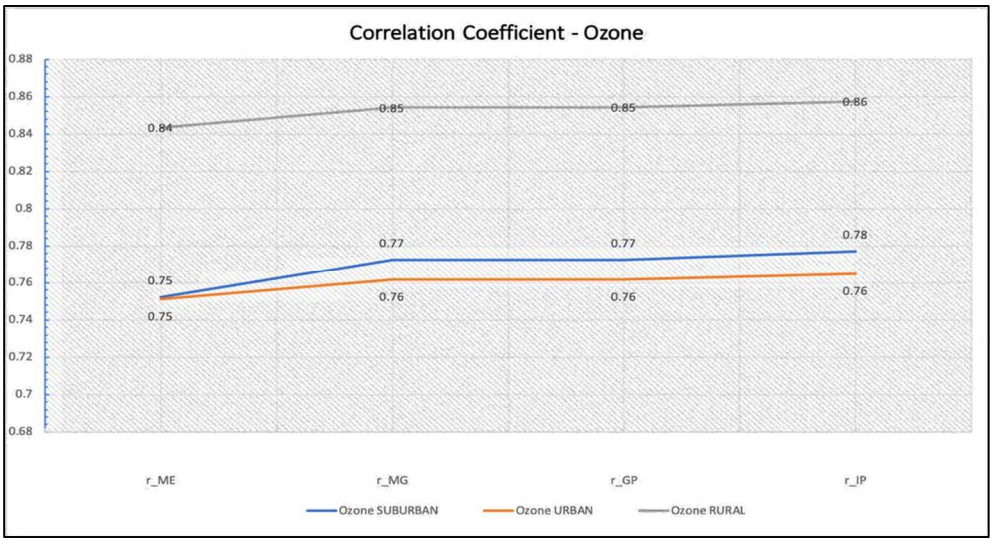

Figure 28: Ozone correlation coefficient [dimensionless] concerning AIRBASE datasets and WRF-Chem model (ME = "Megan_V2.04"; MG = "Megan_Gamma"; GP = "Megan_Gamma_PFT"; IP = "Megan_Gamma_PFTISO").

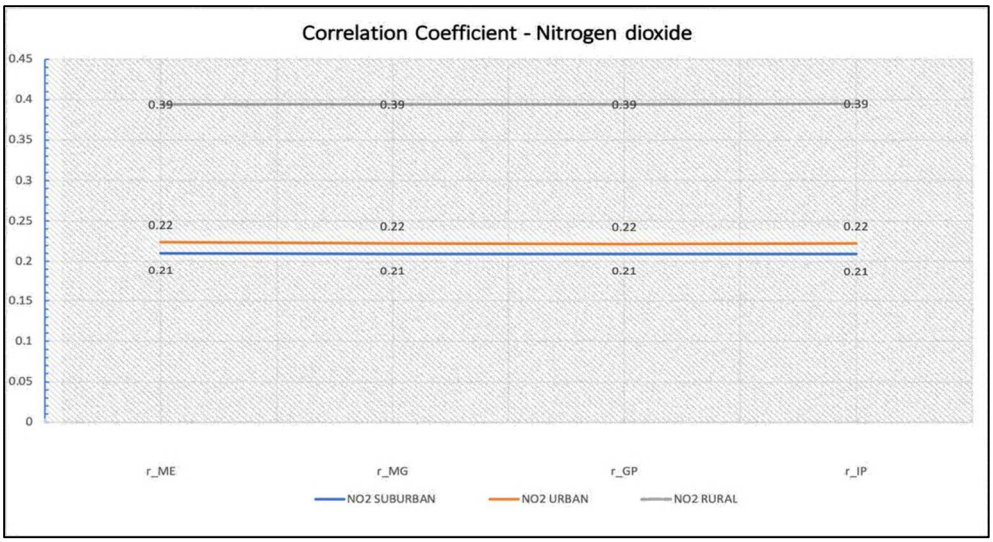

Figure 29: Nitrogen dioxide correlation coefficient [dimensionless] concerning AIRBASE datasets and WRF-Chem model (ME = "Megan_V2.04"; MG = "Megan_Gamma"; GP = "Megan_Gamma_PFT"; IP = "Megan_Gamma_PFTISO").

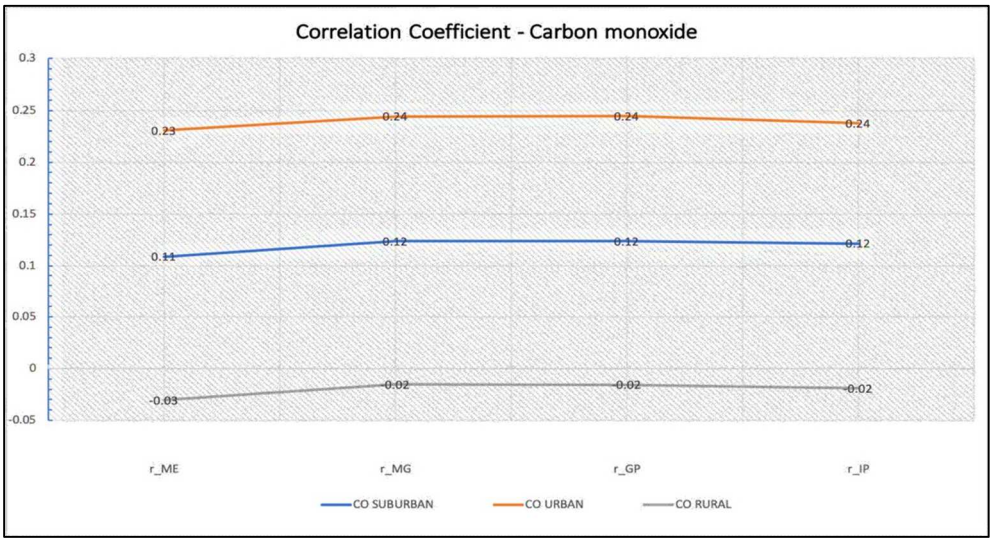

Figure 30: Carbon monoxide correlation coefficient [dimensionless] concerning AIRBASE datasets and WRF-Chem model (ME = "Megan_V2.04"; MG = "Megan_Gamma"; GP = "Megan_Gamma_PFT"; IP = "Megan_Gamma_PFTISO").

Finally, the correlation coefficient demonstrates that O_3 model results (Figure 28) has a strong positive correlation between model and observations, with values equivalent approximately to 0.75, for the urban and suburban area, near 0.85 for the rural area. Nitrogen dioxide (Figure 29) has more variability from ozone, with correlation values for the urban and suburban area of nearly 0.22, and for the rural stations of about 0.39. The CO (Figure 30) shows the worst correlation coefficients (CO_{SUB} = 0.11; CO_{URB} = 0.24; CO_{RUR} = -0.02) (i.e. this poor agreement suggests the anthropogenic emissions are out of date or the biomass burning emissions are not well represented by the model), which is also highlighted by the regression lines plotted in the scatter diagrams of Figure 31. There are not remarkable modifications with the different MEGAN changes simulations: O_3 and CO have an increase of 0.01 from the first simulations (r_ME - "Megan_V2.04") to the MEGAN changes simulations (r_MG - "Megan_Gamma"; r_GP - "Megan_Gamma_PFT"; r_IP - "Megan_Gamma_PFTISO"); Nitrogen dioxide coefficient correlation has literally no modifications.

Appendix A. 4, Appendix A. 5 and Appendix A. 6 tables show the normalized mean bias, the normalized root mean square error and the correlation coefficients respectively for O_3, NO_2 and CO.

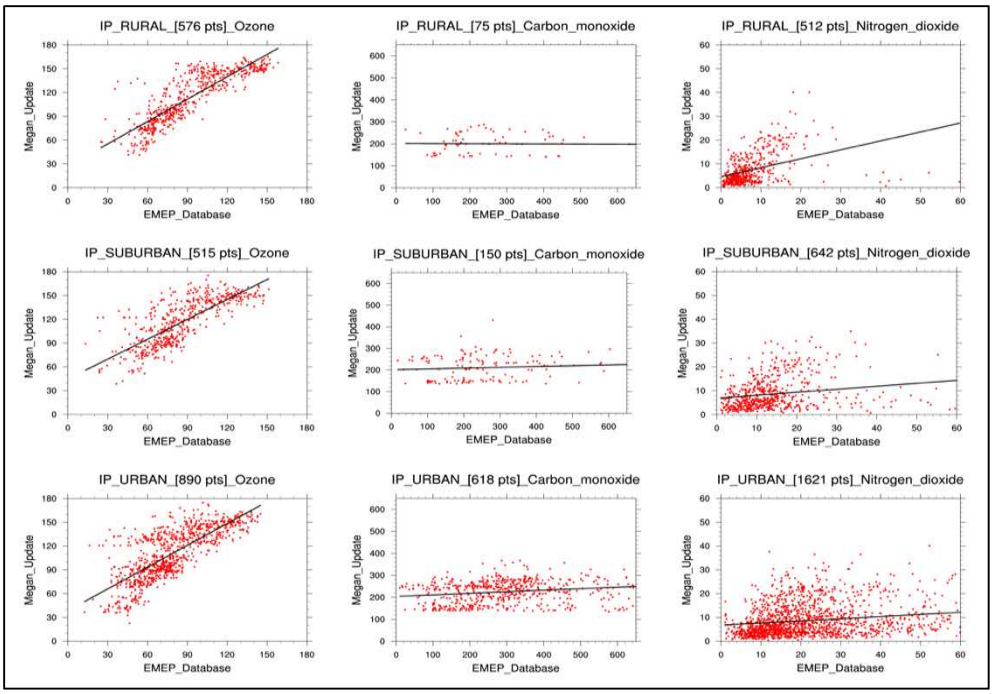

Figure 31: Scatter plot for the simulations IP ("Megan_Gamma_PFTISO"); each column represents respectively ozone, carbon monoxide and nitrogen dioxide [ug/m^3]; each row is respectively the rural, suburban and urban stations.

Maps of mean day time (7 am – 6 pm UTC) concentrations over the whole simulation period (from August 10th 00:00 UTC to 16th 00:00 UTC, 2015) were produced. Figure 33 and Figure 34 display the trace gases considered (ozone, carbon monoxide and nitrogen dioxide) for the control simulation (Figure 33 - ME_avg = "Megan_V2.04") and the last simulation done, with all the MEGAN code updates included (Figure 34 – IP_avg = "Megan_Gamma_PFTISO"), correlated to the spatial distribution of AIRBASE database. The spatial distribution of O_3 concentrations corresponds with observed values. Only magnitude differences are found, as

confirmed by the statistical analysis above, the model in both simulations, control and modified ("Megan_Gamma_PFTISO"), overestimates the AIRBASE data by a value, respectively, about 20 $\mu g/m^3$ (10 ppb) and near 40 $\mu g/m^3$ (20 ppb). The overestimate is clearly visible for most of Europe, but it is more concentrated in central Europe (France, Germany, Switzerland, Austria and Northern Italy) and along the south coast of the Iberian Peninsula.

The measured CO spatial distribution has a more chaotic pattern (Figure 33 and Figure 34), the WRF-Chem model underestimates CO by a factor 2 (from 240 to 500 $\mu g/m^3$ - approximately from 210 to 435 ppb) for most of the stations shown; the gap is more noticeable across Italy, from the south of Spain, Poland and Czech Republic. The magnitude of the gap in the eastern Europe could be a sign the model biomass burning emissions (FINN emissions - Wiedinmyer *et al.*, 2011) could not represent well the overview of the situation; Figure 32 shows CO concentration [$\mu g/m^3$] of the last simulation done, with all the MEGAN updates (left map - "Megan_Gamma_PFTISO"), and the same simulation without including the biomass burning emissions in the calculation (right map - "Megan_Gamma_PFTISO_noFINN"), as the weekly averages (from August 10^{th} 00:00 UTC to 16^{th} 00:00 UTC, 2015), extrapolating just concentrations from the AIRBASE station points and interpolating them over the coarse domain. In the east of Europe is clear a disparity between the two simulations: without including the biomass burning emissions (Figure 32 – right map) the CO concentration decreases from 240-320 to 160-240 [$\mu g/m^3$] interval (209-280 to 140-209 ppb). Conclusively, the disproportion could indicate a presence of wild fire in that area, captured by both the AIRBASE dataset and

the model, but probably, not well represent by biomass burning emissions and their computation in WRF-Chem.

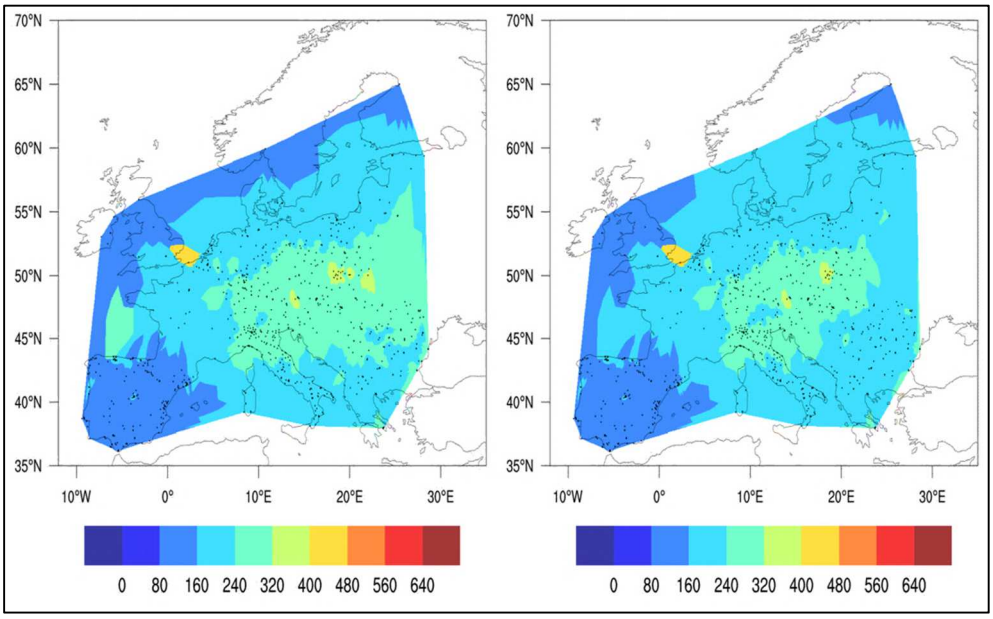

Figure 32: CO concentration [µg/m^3] of the last two simulations done: (1) with all the MEGAN updates (left map - "Megan_Gamma_PFTISO"), and (2) the same simulation without including the biomass burning emissions in the calculation (right map - "Megan_Gamma_PFTISO_noFINN"). The maps represent the weekly averages (from August 10th 00:00 UTC to 16th 00:00 UTC, 2015), extrapolating just concentrations from the AIRBASE station points and interpolating them over the coarse domain.

The NO_2 (Figure 33 and Figure 34) is the compound that show up in the highest number of surface stations (2791 stations - NO_2, 877 stations - CO and 1981 stations - O_3). Its spatial resolution is not well represented in WRF-Chem, especially in the north Europe (England, Belgium, Netherlands and North Germany), Northern Italy and the northeastern part of Spain. There is a huge underestimate of NO_2 by the model in Austria and Germany, where the difference has a factor about 10 (from 5 to 50 µg/m^3 - approximately from

2.5 to 5 ppb); the big dissimilarity might indicate the lack of update anthropogenic emissions since the nitrogen oxides (NO_X) are mainly emitted from anthropogenic sources (EDGAR-HTAP emissions) (e.g. road traffic).

The last notable information, emerging from Figure 33 and Figure 34, is the carbon monoxide, and nitrogen dioxide concentrations, do not have changes between the MEGAN update simulations, considering both, the spatial resolution and concentration magnitude; this notion is confirmation of the statistical analysis developed from the section above.

From Appendix A. 7 to Appendix A. 12 the remaining simulations maps (“Megan_Gamma”; “Megan_GammaPFT”).

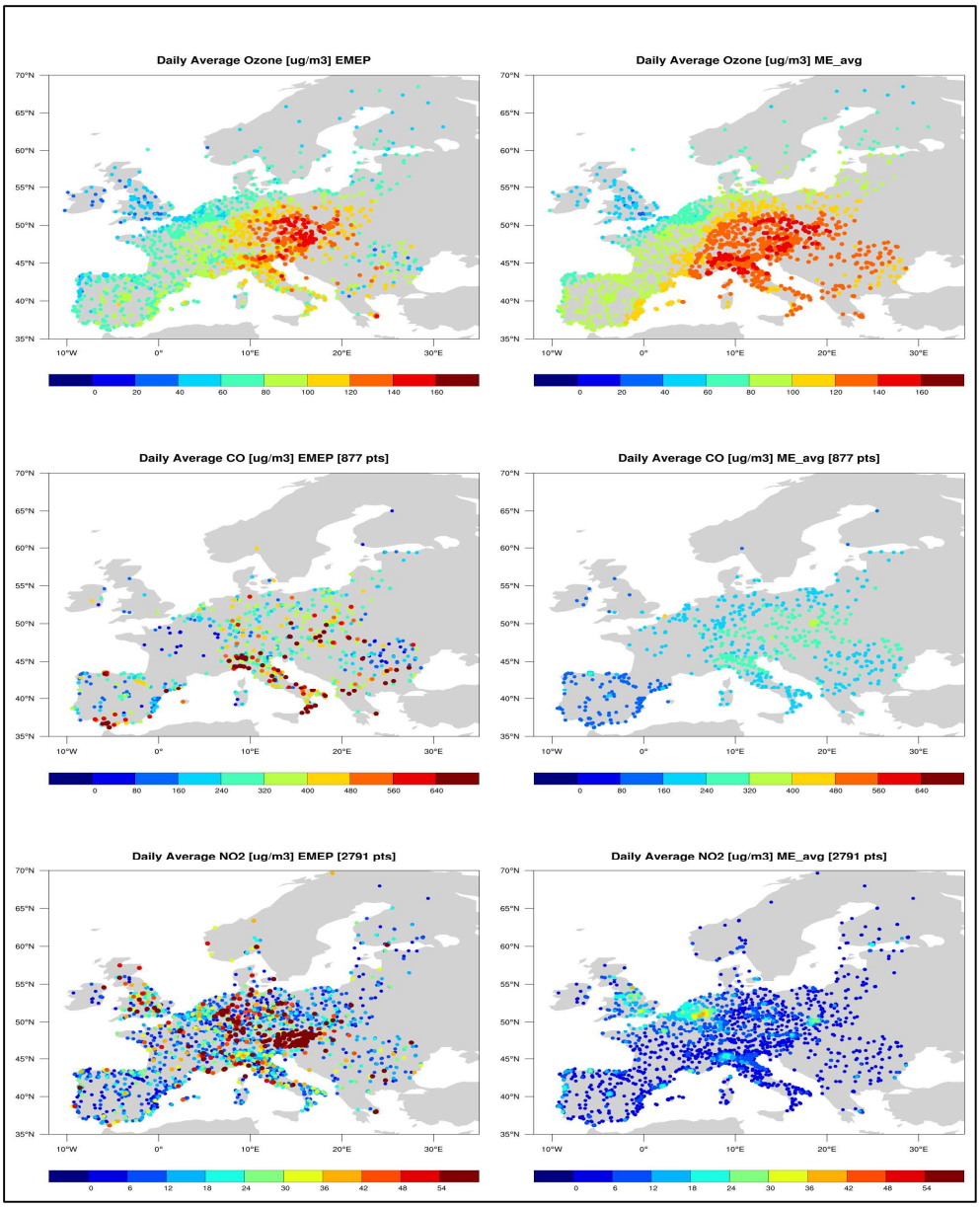

Figure 33: The spatial resolutions of the mean day time (7 am – 6 pm UTC) concentrations for O_3, CO and NO_2 over the whole simulation period (from August 10th 00:00 UTC to 16th 00:00 UTC, 2015) for control simulation ("Megan_V2.04") compared against the AIRBASE dataset (12 km x 12 km resolution).

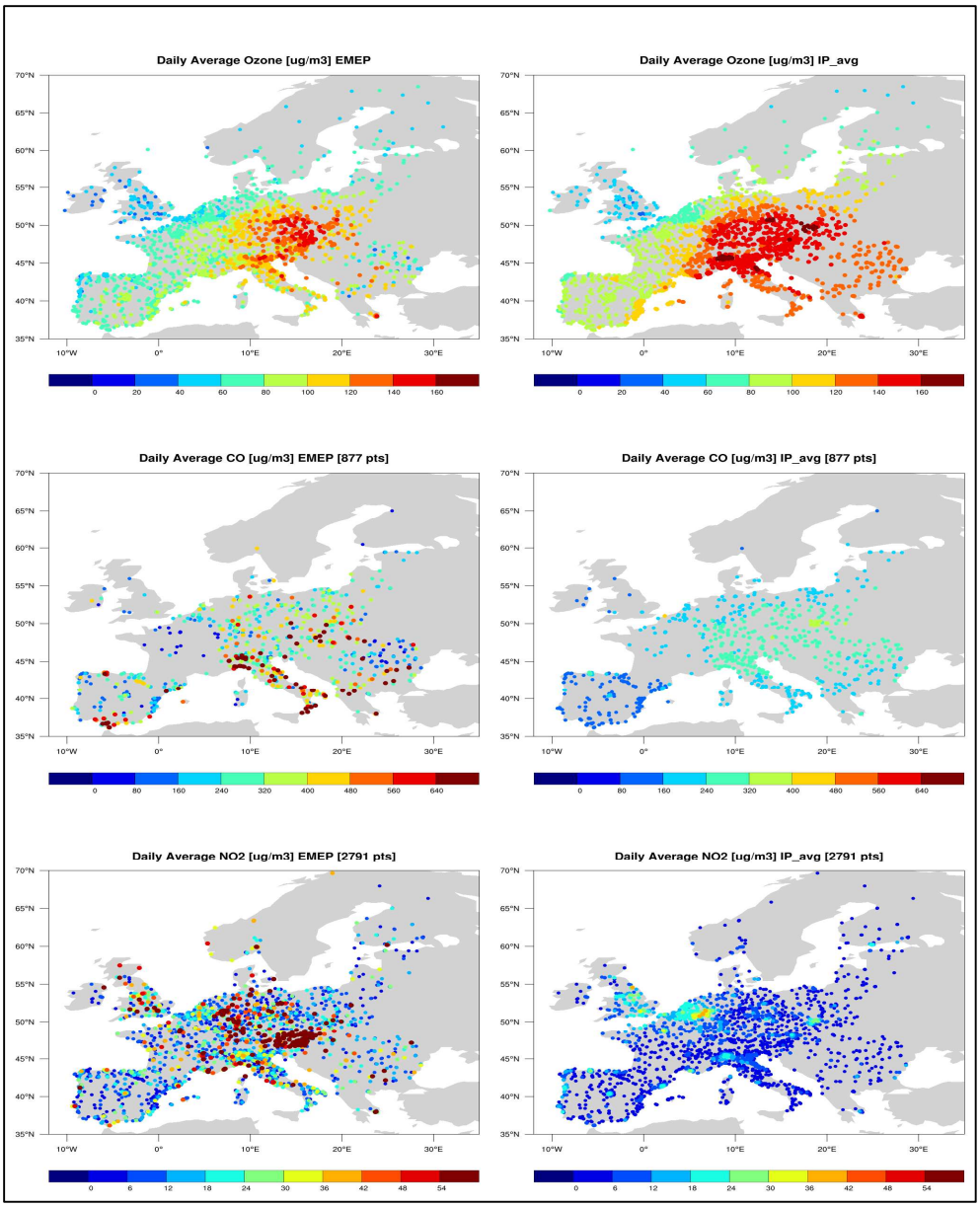

Figure 34: The spatial resolutions of the mean day time (7 am – 6 pm UTC) concentrations for O_3, CO and NO_2 over the whole simulation period (from August 10th 00:00 UTC to 16th 00:00 UTC, 2015) for simulations with all the MEGAN code updates included ("Megan_Gamma_PFTISO"), compared against the AIRBASE dataset (12 km x 12 km resolution).

2.3.5. NOMADSS field campaign: gas-phase

The mechanism reaction for producing ozone is complex, involving hundreds of chemical species interacting with transport on a different time and spatial scales. Chemical transport models tend to significantly overestimate surface ozone in the U.S. (Lin *et al.*, 2008; Fiore *et al.*, 2009; Brown-Steiner *et al.*, 2015), and as noticed from the results above, also in European scenario. The NOMADSS aircraft campaign, lasting from June to July 2013, provides an outstanding opportunity to improve our understanding of ozone chemistry. In this part of the study the MEGAN code updates have been compared with the NCAR C-130 flight tracks to acquire more the effects of these changes above the surface, yet primarily in the boundary layer.

Figure 35 and Figure 37 show the flight altitude [km], the temperature [K], the relative humidity [%] and the concentrations of ozone [ppb], NO_x (NO_2 + NO) [ppb], isoprene [ppt], MACR (methacrolein) [ppt] and MVK (methyl vinyl ketone) [ppt] for the first two flight tracks (rf01 – rf02) which occurred on June 3rd (14 – 19 UTC; 9 - 14 US central time zone) and June 5th, 2013 (14 – 21 UTC; 9 – 16 US central time zone); the flight tracks rf03, rf04 and rf05 are plotted in Appendix A. 13, Appendix A. 14 and Appendix A. 15. The black line represents the C-130 aircraft measurements, the green line indicates the WRF-Chem model results using MEGAN version 2.04 (control simulation - "Megan_V2.04") and the red line corresponds to the WRF-Chem simulation with MEGAN updated to the version 2.10 ("Megan_Gamma_PFTISO"). The resolution of the model domain is 12 km grid since the comparison is referred to the model coarse domain (Figure 10). On the other hand, Figure 36 represent the planetary boundary layer height

[km] extrapolated from WRF-Chem model using the time and position of the rf01and rf02 flight tracks.

Table 11: Gas-phase reactions involving ISOP (isoprene) to the formation of MVK (methacrolein) and MACR (methyl vinyl ketone) in MOZART-4 chemical mechanism. The table is adapted from the table 3 of Emmons *et al.*, 2010.

Reactants	**Products**
ISOP + OH	→ $ISOPO_2$
ISOP + O_3	→ 0.4·MACR + 0.2·MVK + 0.07·C_3H_6 + 0.27·OH + 0.06·HO_2 + 0.6·CH_2O + 0.3·CO + 0.1·O_3 + 0.2·MCO_3 + 0.2·CH_3COOH
$ISOPO_2$ + NO	→ 0.08·ONITR + 0.92·NO_2 + HO_2 + 0.55·CH_2O + 0.23·MACR + 0.32·MVK + 0.37·HYDRALD
$ISOPO_2$ + NO_3	→ HO_2 + NO_2 + 0.6·CH_2O + 0.25·MACR + 0.35·MVK + 0.4·HYDRALD
$ISOPO_2$ + HO_2	→ ISOPOOH
ISOPOOH + OH	→ 0.5·XO_2 + 0.5·$ISOPO_2$
$ISOPO_2$ + CH_3O_2	→ 1.2·CH_2O + 0.19·MACR + 0.26·MVK + 0.3·HYDRALD + 0.25·CH_3OH + HO_2
$ISOPO_2$ + CH_3CO_3	→ 0.6·CH_2O + 0.25·MACR + 0.35·MVK + 0.4·HYDRALD + CH_3O_2 + HO_2 + CO_2
ISOP + NO_3	→ $ISOPNO_3$
$ISOPNO_3$ + NO	→ 10.206·NO_2 + 0.072·CH_2O + 0.167·MACR + 0.039·MVK + 0.794·ONITR + 0.794·HO_2
$ISOPNO_3$ + NO_3	→ 10.206·NO_2 + 0.072·CH_2O + 0.167·MACR + 0.039·MVK + 0.794·ONITR + 0.794·HO_2
$ISOPNO_3$ + HO_2	→ 0.206·NO_2 + 0.008·CH_2O + 0.167·MACR
ISOPOOH + hν	→ 0.402·MVK + 0.288·MACR + 0.69·CH_2O + HO_2
TERPOOH + hν	→ OH + 0.1·CH_3COCH_3 + HO_2 + MVK + MACR

The measurements in the rf01 flight track (Figure 35) clearly show higher O_3 concertation at higher altitudes in the free troposphere (e.g. in the interval concerning 14-15 and 17-19 UTC time) compared to the ozone in the

planetary boundary layer, modeled results do not represent this type of vertical profile; indeed, the model results at about 4 km altitude are certainly distant from the flight track values (i.e. with an overestimated of about 40 ppb). In order to analyze the PBL ozone evolution, the second flight measurements (Figure 37) show, from 17 to19 UTC time (10 - 15 US central time zone), a clear time frame where the flight track height is lower than the planetary boundary layer height; the state is clear too, the rf02 flight track ozone concentrations are closer to the MEGAN version 2.04 results (control simulation) than the other simulation ("Megan_Gamma_PFTISO"), showing, the updates made to the MEGAN algorithm, taking the model results away from those measured. Even the isoprene measurements are closer to the control simulation results (green line) then updated simulation (red line) in planetary boundary layer: the isoprene concentrations overestimate the NOMADSS considerably up to a factor of 5 (about 1000 ppt - rf01; about 10000 ppt - rf02; about 5000 ppt - rf03; about 8000 ppt - rf04; about 15000 ppt - rf05). Conclusively, NO_x is not really changed by the MEGAN changes, on the other hand, it shows an overestimate between the model results and the flight track data. The methacrolein (MACR), a long-life compound where isoprene is involved in its formation reaction (Table 11), confirms the same development of its precursor: in the PBL, the flight track measurements are closer to the control simulation than the updated simulation (up to a factor of 4). Finally, the methyl vinyl ketone (MVK), an isoprene-depended compound, demonstrate an inverse trend of isoprene, since the NOMADSS track values are similar to the simulation with the MEGAN code updated than control one.

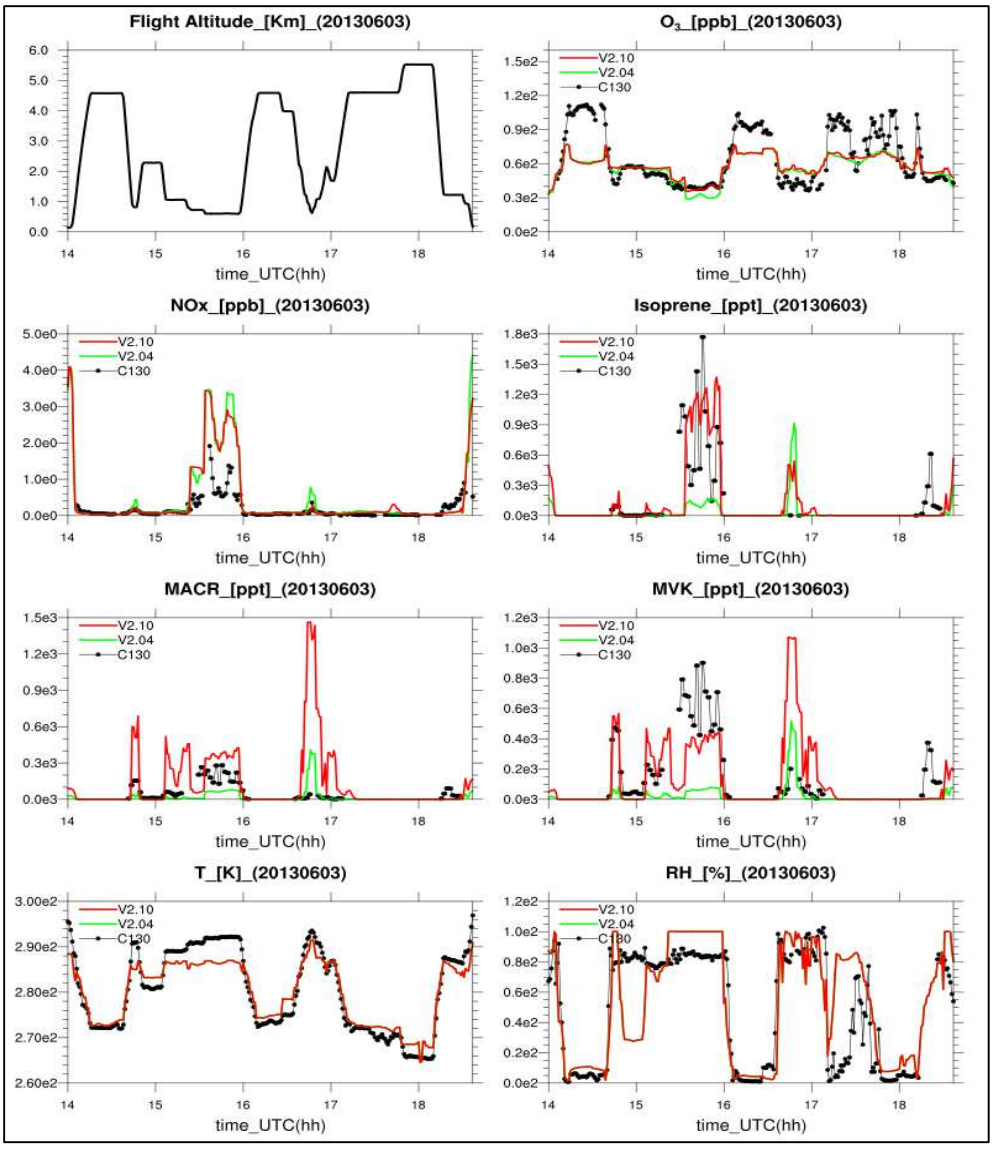

Figure 35: The flight altitude [km], the temperature [K], the relative humidity [%] and the concentrations of ozone [ppb], NO_x (NO_2 + NO) [ppb], isoprene [ppt], MACR (methacrolein) [ppt] and MVK (methyl vinyl ketone) [ppt] for the first NOMADSS flight (rf01). The black line is referred to the C-130 aircraft measurements, the green one indicates the WRF-Chem model results using MEGAN version 2.04 (control simulation - "Megan_V2.04") and the red line is the WRF-Chem simulation with MEGAN updated to the version 2.10 ("Megan_Gamma_PFTISO").

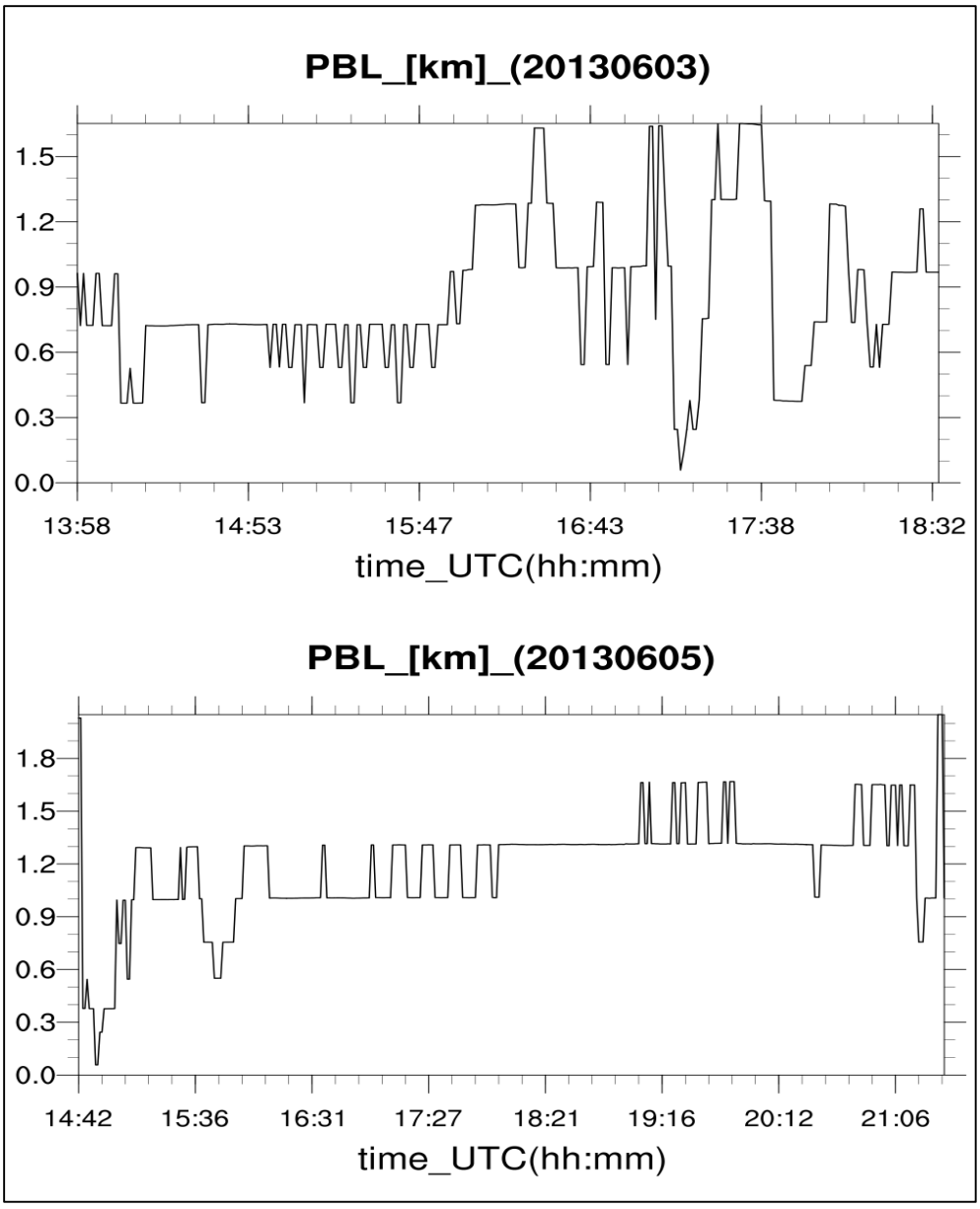

Figure 36: PBL altitude [km], for rf01 and rf02 NOMADSS flights track. They occurred, respectively, on June 3th (14 – 19 UTC; 9 - 14 US central time zone) and June 5th (14 – 21 UTC; 9 – 16 US central time zone), 2013.

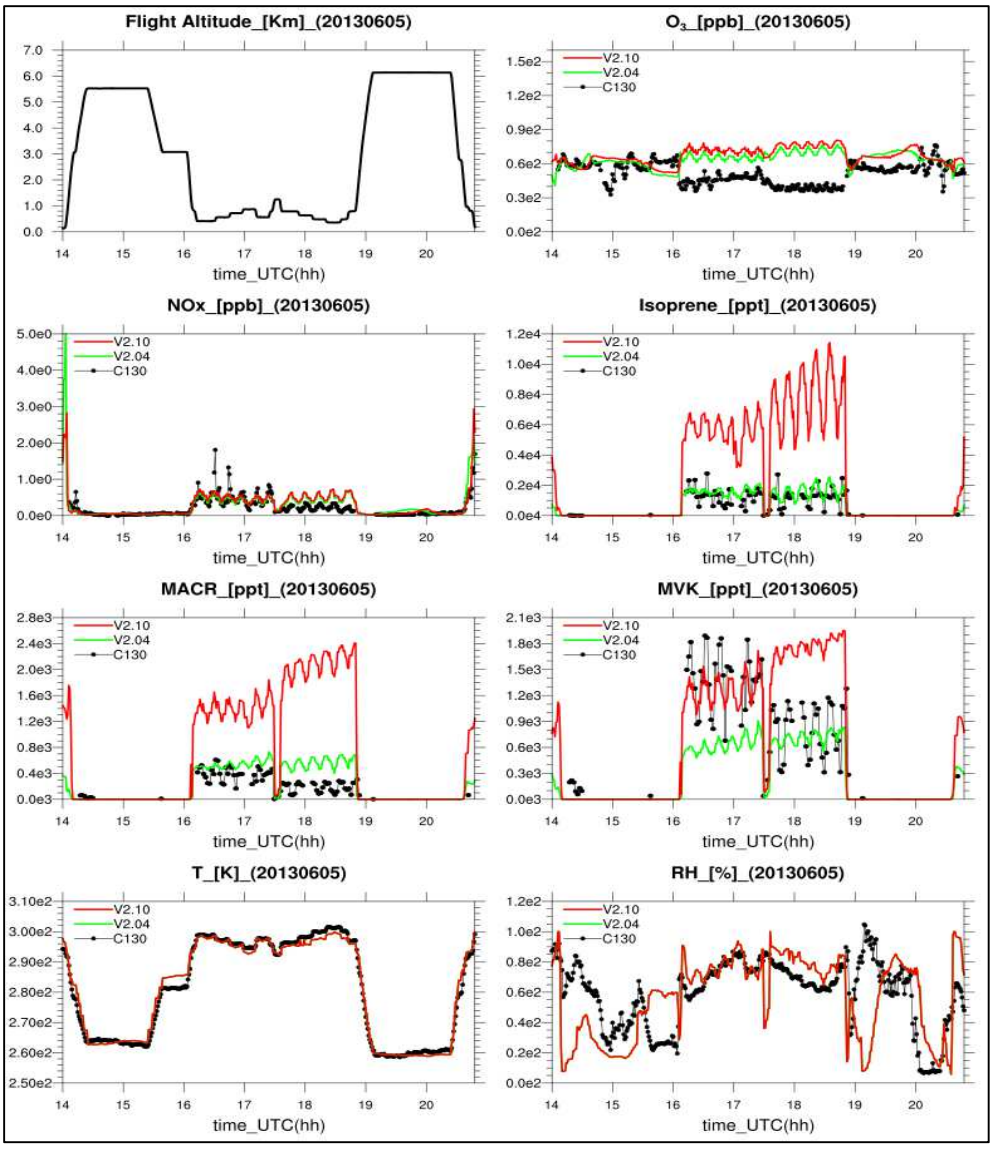

Figure 37: The flight altitude [km], the temperature [K], the relative humidity [%] and the concentrations of ozone [ppb], NO_x (NO_2 + NO) [ppb], isoprene [ppt], MACR (methacrolein) [ppt] and MVK (methyl vinyl ketone) [ppt] for the second NOMADSS flight (rf02). The black line is referred to the C-130 aircraft measurements, the green one indicates the WRF-Chem model results using MEGAN version 2.04 (control simulation - "Megan_V2.04") and the red line is the WRF-Chem simulation with MEGAN updated to the version 2.10 ("Megan_Gamma_PFTISO").

2.4. Conclusions

The main goal of the study was to examine and test the BVOC emission model MEGAN and the updates made in the emission equation with four simulations, one of each code changes, using the WRF-Chem chemical transport model (CTM). Two sets of simulations were conducted, the first one is in Europe where an ozone high concentration event of 6 days was chosen (from August 10th 00:00 UTC to 16th 00:00 UTC, 2015), from a three-year analysis, and the second one is in U.S. concurrently with the NOMADSS field campaign (from June 1th 00:00 UTC to June 15th 00:00 UTC, 2013).

In the European case of study, the meteorological conditions are very well simulated, however there is room left for improvements through nudging or data assimilation of meteorology. Results for isoprene and α-pinene emissions demonstrate that by updating the MEGAN code, the BVOC emissions increase considerably, unfortunately there are not an experimental database to compare the emissions with, so it is not possible to say which configuration is more realistic. The fact that in some cities we have a higher increase of isoprene then the other (i.e. Zagreb has an increase about 100 mol/km^2 hr and Kiev about 50 mol/km^2 hr) suggests a development for the future: discover and tune the driving parameters inside the equation in order shed light in the question. For example, the emission activity factors are one of the major responsible of the biogenic emission; they have increased notably with an average value up to 3 (e.g. Genoa, Zagreb). Results for trace gases are still preliminary, only the temporal and spatial distribution of the O_3 are in good agreement with the observations, however, the concentration values are overestimated for all type of stations (rural, urban and suburban).

The control simulation has the better results for ozone, since the updates simulations increase the ozone concentration by 20 to 40 ppb. The NO_2 and CO model results are very underestimate, respectively by -50 % and -30 %. The spatial resolution for those compounds are less clear and more disordered, perhaps for the deviation of the model results from the real data, but also because the anthropogenic emissions used (EDGAR-HTAP) are referred to 2010 may be out of date.

The NOMADSS field campaign settle the overestimate of the isoprene and ozone concentrations analyzed by the emissions over the Europe, confirming the theory that the changes made to MEGAN increase greatly the concentrations instead of adapting (decreasing) them. In this case, the NO_x concentrations, have a better agreement with the aircraft then what see in the European case of study, but they are overestimate too; the better agreement with real data, can be given by the different database of the anthropogenic emissions (NEI emissions) used.

3. Sources and transport of natural and anthropogenic aerosols to southern Europe: evaluation of WRF-Chem model

3.1. Saharan mineral dust

In recent decades, various studies have shown the influence of anthropogenic and natural aerosols on the atmospheric, hydrological and terrestrial systems, increasing interest in climate processes. Atmospheric aerosols, along with clouds, have a considerable effect over the radiative energy balance of the Earth's ecosystem. Considering the aerosols total mass, the mineral dust is the main atmospheric natural aerosol, it includes up to 75% of the global aerosol mass, and therefore, plays a very important role in the earth radiative system (Ginoux *et al.*, 2012). The aerosol particles interact with the atmosphere through two type of effects: direct and indirect effects. The direct effects are due to the particles scattering and absorption capacity, they could have consequences in the net heating rate. The indirect effects are due to the interaction of particles with clouds, and can affect the radiative budget via altered cloud properties, such as cloud drop size, cloud lifetime, and cloud thickness (Twomey, 1977; Baker, *et al.*, 1980; Albrecht, 1989).

The Sahara desert is the main source of mineral dust on the planet: about half of the total emission is generated in the Sahara desert (Ginoux *et al.*, 2004). The convection produced by strong surface heating can lift dust particles for several kilometers into the free troposphere and transported over

large distances. An extensive dust fraction produced by the Sahara remains in Africa, as it is transported and stored in the Sahel countries. Another significant fraction is transported westward across the Atlantic Ocean, but large quantities of mineral dust are also transported across the Mediterranean Sea to Europe in episodic events (outbreaks) (Engelstaedter *et al.*, 2006) (Rizza, *et al.*, 2017). During the outbreaks, mineral dust particles can be considered as the major source of PM_{10} in urban and rural sites of the Mediterranean basin, contributing to a significant percentage of the episodes of exceeding the average daily limit of PM_{10} 50 $\mu g/m^3$ with peaks up to 80% of the total mass; on European level, the areas most affected by the presence of aerosols emissions are Italy, Greece and Spain (Gobbi *et al.*, 2007).

The studies of the mineral dust transport are getting increasing attention from the scientific community allowing better investigation of its impact on the terrestrial radiation budget, on the microphysics of clouds, as well as, on air quality and human health. The mineral dust emissions parameterization, and the relative transport, is still difficult to determine due to the uncertainties related to the extensive nature of emissions, the nature of the soil, the aerosols chemistry complexity and the meteorological conditions. However, intensive measurement campaigns have been conducted to increase our understanding of the effects of dust pollution (Deroubaix *et al.*, 2013). In addition to the measurement campaigns, satellite observations provide crucial information on the global distribution of dust (e.g. MODIS - MODerate resolution Imaging Spectro-Radiometer). Finally, the AERONET network (Aerosol Robotic NETwork) provides considerable information on the optical and physical properties of aerosols (Dubovik and King, 2000). Furthermore,

thanks to the simulations of dust intrusions, by global and regional chemical and climate models, e.g. GEOS-CHEM (Bey *et al.*, 2001), CAM-CHEM (Lamarque *et al.*, 2012), MERRA-2 (Gelaro *et al.*, 2017) and WRF-Chem (Grell *et al.*, 2005; Fast *et al.*, 2006), a more accurate understanding of the aerosols parametrization and transport can be obtained. The numerical models applied in previous studies, to simulate the Saharan episodes over the Mediterranean Basin, present a wide diversity in simulating the transport of dust, as also evident in a recent study concerning a comparison of a set of 9 simulations of regional models of mineral dust on Europe (Basart *et al.*, 2016). This can be attributed to different parameterizations of emission models and to different deposition schemes, as well as, to various model configurations and soil surface properties (Huneeus *et al.*, 2011; Rizza, Miglietta, *et al.*, 2017).

Most of the mineral dust sources are in arid and semi-arid regions that extend from the west coast of North Africa, the Middle East and into the Central Asia. The global mineral dust emission rates are estimated in a range between 1000 to 3000 Tg/yr, 80% of that are generated in the northern hemisphere (Tanaka and Chiba, 2006). As mentioned before, the world's largest source of mineral dust is the Sahara Desert. The dust emissions from the Sahara Desert range between 500 and 1400 Tg/yr contributing about 50%-70% of total emission (Ginoux *et al.*, 2001; Prospero *et al.*, 2002). The Bodélé depression, the lowest point in Chad (south of the Tibesti Mountains - 21°N 18°E), is one of the driest places on earth and one of the most important point for dust emissions in the Sahara Desert, due to the erodibility of the surface material and the wind erosion potential (Washington *et al.*, 2006). It

is estimated that small area produces about 50% of Saharan mineral dust deposited in the Amazon rainforest (Koren *et al.*, 2006).

Figure 38, reproduced from Ginoux *et al.*, 2012, shows the average annual distribution of the percentage of days per year in which the M-DB2 DOD (MODIS Deep Blue Level 2 Dust Optical Depth) is higher than 0.2. A large dust source is found on southern Sahel (black rectangular outline A), it is predominantly of anthropogenic origin; reported measures showing that ephemeral lakes were reactivated from intensive grazing and cultivation in Senegal (position 1), as well as, in Mali (blue spot in position 3). Mahowald and Kiehl 2003 demonstrated the importance of the hydrological cycle on modulation of dust emission in the Chotts area (position from 19 to 22). Finally, position 7 shows the depression of Bodélé, whose frequency and intensity of the emissions has been correlated to a Venturi effect of the Harmattan winds passing between the Ennedi mountains (position C) and Tibesti (position D) (Washington *et al.*, 2006).

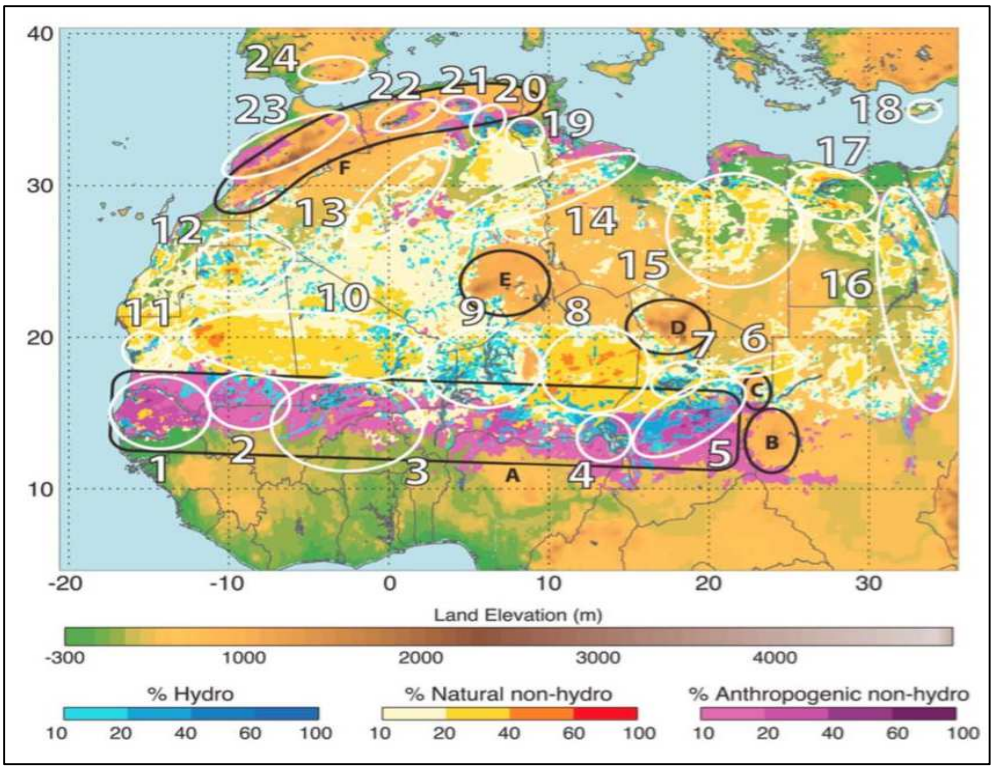

Figure 38: Distribution of the percentage number of days per year M-DB2 DOD > 0.2 (MODIS Deep Blue Level 2 Dust Optical Depth). The frequencies associated with (hydro) and without (non-hydro) ephemeral water bodies and with less (natural) and more (anthropogenic) than 30% of grid cell (MODIS with 0,01° resolution database) land use are shaded in blue; yellow, red, and orange; and magenta, respectively (Ginoux *et al.*, 2012).

Satellite images and measurements of atmospheric dust concentration confirm that the mineral dust emitted from the Sharan Desert can be transported at great distances in the atmosphere away from the sources. Usually, there are three main transport trajectories from the North African sources, dust particles can be transported: across the Atlantic Ocean (to the United States, the Caribbean and South America), toward the Mediterranean

(central and southern Europe) (Kallos et al. 2009 shows that the amount of dust transported is of the order of 100 t/yr) and finally, to the Eastern Mediterranean (Middle East) (Tanaka and Chiba, 2006).

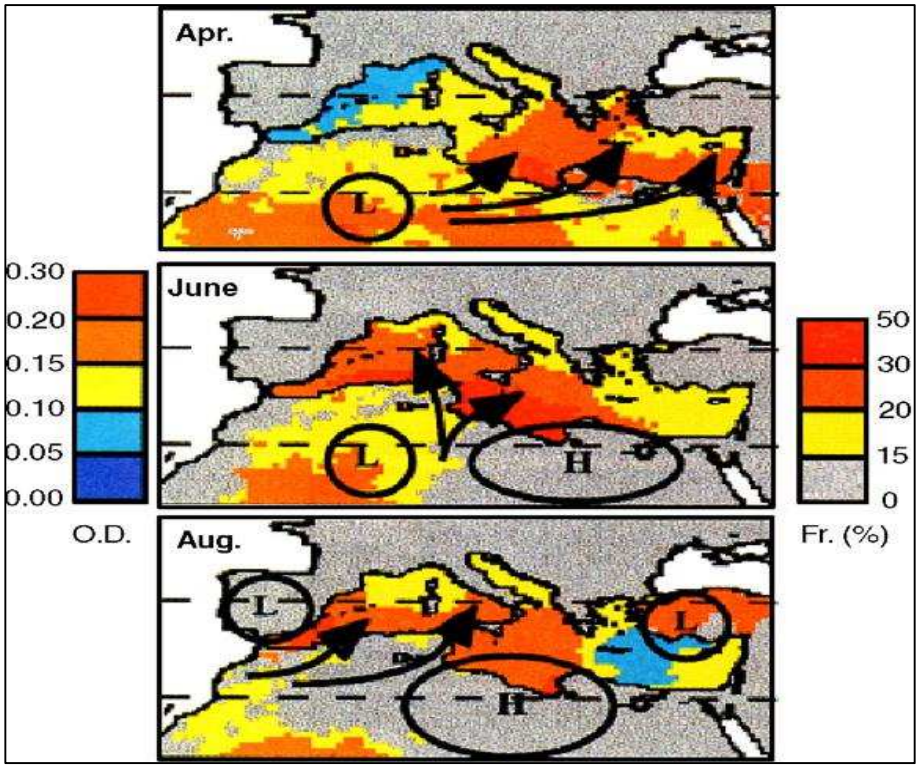

Figure 39: Main meteorological synoptic situation for dust generation and transport during spring and summer in the Mediterranean. The frequency (Fr.) of dust mobilization over North Africa has been estimated from IDDI derived Meteosat images. Dust optical depth (O.D.) is estimated also from available Meteosat (Moulin *et al.*, 1998).

In spring/summer the air over North Africa is loaded by a considerable amount of mineral dust, low-pressure systems called “Sharav cyclones” activate the suspended mineral dust and transport it to north and east along the Mediterranean coast. Storms of mineral dust begin to appear in the western Mediterranean and move eastward, most of them travel at least to the eastern Mediterranean coast. Moulin et al. 1998, using Aerosol Optical Depth (AOD) Meteosat analysis, shows that the Sharan dust transport to the north follows a seasonal trend, moving from east to west, of the Mediterranean basin, between March and August. Three different main cyclogenesis situations are responsible for this situation (Figure 39). The figure shows “Sharav cyclones” in April (top), the coupling between a low pressure on the Sahara and a high pressure over Libya in June (in the middle), and the omega-like configuration caused by the cyclogenesis in the Atlantic coasts of Spain/Portugal in August (bottom).

3.2.Materials and Methods

3.2.1. Domains and simulations settings

To perform the assessment of Sharan dust outbreaks to the Mediterranean basin (especially to the Italian peninsula), the CTM model WRF-Chem 3.9 (Grell *et al.*, 2005; Fast *et al.*, 2006) was employed for the whole year 2017 (from January 1st 2017 00:00 UTC to January 1st 2018 00:00 UTC), in order to outline the seasonal changes and the mineral dust outbreaks occurred during this period (e.g. March 2017 and August 2017). Figure 40 shows the model domain, which cover most part of northern Africa and southern Europe that could be affected from the Saharan dust outbreaks (Italy, Spain, Portugal and Greece). The domain has 430×330 grid points centered at 30° N and 10° E with a horizontal grid spacing of 15 km for both directions (west-east and south-north) and 40 vertical levels up to 50 hPa.

The initial and boundary meteorological conditions are provided by ERA-Interim (ds627.0): the latest global atmospheric reanalysis produced by the European Centre for Medium-Range Weather Forecasts (ECMWF). The system includes a 4-dimensional variational analysis (4D-Var) with a 12-hours analysis window, the spatial resolution of the data set is approximately 80 km (T255 spectral) on 60 vertical levels from the surface up to 0.1 hPa (Dee *et al.*, 2011). The static geographical fields, such as terrain height, soil properties, vegetation fraction, land use and albedo are interpolated from 30-arc-second (~ 900 m) (United States Geological Survey (USGS) data) to the model domain by using the WRF preprocessing system (WPS).

Four-dimensional data assimilation (FDDA) technique is also applied to limit the model errors in the simulated meteorological fields because the production and transport of dust aerosols depend crucially on the accuracy of simulated meteorology. The horizontal winds, moisture and temperature are nudged at all vertical levels and PBL (Kumar *et al.*, 2014).

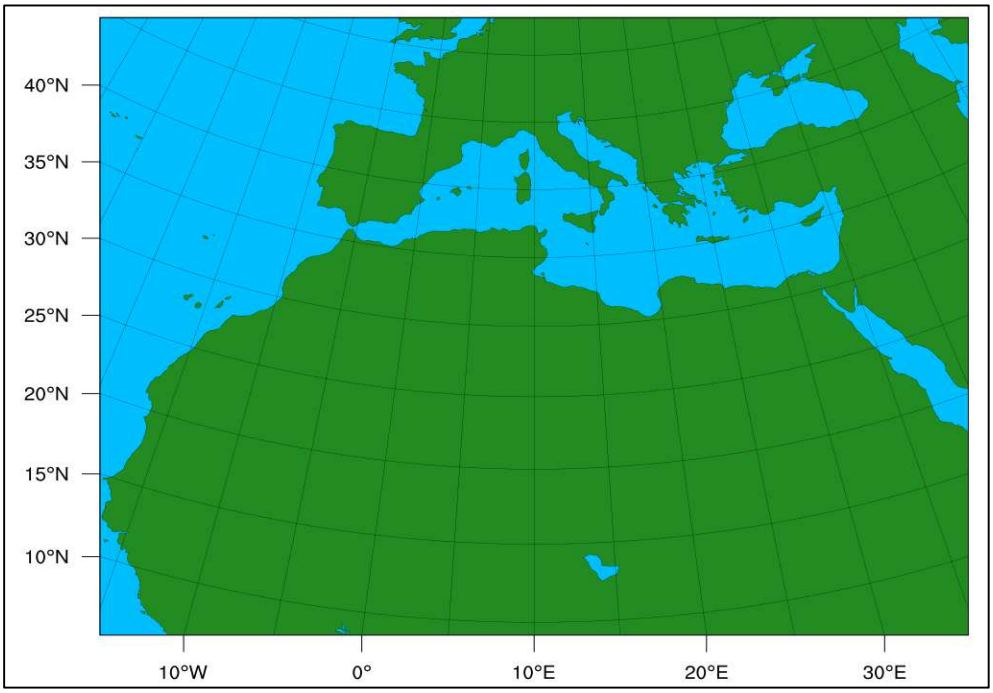

Figure 40: The numerical domains of the simulations: the coarse domain has 430×330 grid points with 15 Km grid cells.

The Table 12 summarizes the physical schemes used for the simulations done. The Morrison double-moment scheme (mp_physics=10) is adopted for the treatment of the microphysics processes (Morrison, Thompson and Tatarskii, 2009). The Rapid Radiative Transfer Model (RRTMG), for both shortwave (ra_sw_physics = 4) and longwave

(ra_lw_physics = 4) radiation, is used for the aerosol direct radiative effect (Iacono *et al.*, 2008). The Mellor–Yamada–Nakanishi and Niino (MYNN) 2.5 level turbulent kinetic energy (TKE) parameterization is used to describe the planetary boundary layer (Nakanishi and Niino, 2006). The Noah-MP (multi-parametrization options) land-surface model (sf_surface_physics = 4) is chosen to represent the land surface interaction because it uses multiple options for key land-atmosphere interaction processes, contains a separate vegetation canopy defined by a canopy top and bottom and includes a multi-layer snow pack with liquid water storage (Niu *et al.*, 2011). The Grell-Freitas scheme (cu_physics = 3) is considered for the cumulus parameterization scheme: the scheme tries to smooth the transition to cloud-resolving scales (Grell and Freitas, 2014).

Table 12: Namelist settings of the physical parameterizations used in the WRF-Chem setup simulations.

	Number and option variable		**Model scheme**
Microphysics	10	mp_physics	Morrison two moment
Longwave radiation	4	ra_lw_physics	RRTMG
Shortwave radiation	4	ra_sw_physics	RRTMG
PBL model	5	bl_pbl_physics	MYNN 2.5 level TKE
Land surface	4	sf_surface_physics	Noah-MP land-surface
Cumulus parameterization	3	cu_physics	Grell-Freitas

Two simulations were conducted to assess the impact of the Saharan dust outbreaks on the Mediterranean basin: the first one, with the "dust only" chemical option (chem_opt = 401), and the second one, with the chemical option (chem_opt = 201) with MOZART (Model for Ozone and Related chemical Tracers – version 4) (Emmons *et al.*, 2010), for the trace gases part, and MOSAIC (Model for Simulating Aerosol Interactions and Chemistry) (Zaveri *et al.*, 2008) for the aerosol-phase species. In the first simulation, no other emissions have been added (anthropogenic, biomass burning and biogenic emission), only the aerosol chemical boundary were provided (dust_1, dust_2, dust_3, dust_4, dust_5,) with the MOZBC preprocessor (MOZART Boundary Conditions). The second simulation is a more comprehensive simulation, the EDGAR-HTAP (Emission Database for Global Atmospheric Research) emission inventory are used to provide the anthropogenic emissions, the biomass burning emissions are obtained from the database FINN (Fire Inventory from NCAR) (Wiedinmyer *et al.*, 2011), the biogenic emissions from MEGAN database (Guenther et al. 2006) and the chemical boundary data for both, gas and aerosol, were provided through the MOZBC preprocessor. Table 13 summarizes the simulations done, for the whole 2017, on the domain above (Figure 40).

Table 13: The two simulations done with the relative chemical option.

DUST simulations	
DUST ONLY	**chem_opt = 401**
MOZART_MOSAIC_4bins	**chem_opt = 201**

It is important to point out that the two simulations have in common the dust emission scheme (dust_opt = 1), the Georgia Tech/Goddard Global Ozone Chemistry Aerosol Radiation and Transport (GOCART) (Chin, *et al.,* 2000). Dust uplifting flux (F_p) [μg/m^2] is calculated as

$$F_p = C \cdot S \cdot s_p \cdot u_{10m}^2 \cdot (u_{10m} - u_t) \quad (47)$$

$$S = \left(\frac{z_{max} - z_i}{z_{max} - z_{min}}\right)^5 \quad (48)$$

where:

- **C** is a dimensional factor equal to 1 [μg s^2/m^5] (previous studies over Sahara (Zhao *et al.*, 2010) suggested a ranging from 0.4 to 0.65);
- **S** is the probability to have accumulated sediments in the grid cell i-th of altitude $\mathbf{Z_i}$ [m];
- $\mathbf{Z_{max}}$ and $\mathbf{Z_{min}}$ are the maximum and minimum elevations in the surrounding 10° x 10° topography [m];
- U_{10m} is the horizontal wind speed at 10 m [m/s];
- U_t is threshold velocity [m/s];
- $\mathbf{S_p}$ is the fraction of each size class of dust in the emission.

The WRF-Chem model includes, in addition to the module described above (GOCART), two alternative packages for mineral dust emission, GOCART/AFWA (Georgia Tech/Goddard Global Ozone Chemistry - Aerosol Radiation and Transport Air Force Weather Agency) (dust_opt = 3)

and DUSTUOC (from the University of Cologne) (dust_opt = 4). The last option is further divided into three emission parameterizations (dust_schme = 1, dust_schme = 2 and dust_schme=3) (Shao, 2001, 2004; Shao *et al.*, 2011). The first emission scheme, GOCART AFWA, was developed based on the Marticorena-Bergametti scheme (Marticorena and Bergametti, 1995) in the GOCART model. It calculates the saltation flux (Q) [μg/m^2] from the surface, for a particular dust size as (White, 1979)

$$Q = C\frac{\rho_a}{g}u_*^3\left(1 + \frac{u_{*t}}{u_*}\right)\left(1 - \frac{u_{*t}^2}{u_*^2}\right) \quad u_* \geq u_{*t} \tag{49}$$

$$Q = 0 \qquad u_* < u_{*t} \tag{50}$$

where:

- **C** is a tunable empirical proportionality constant [μg s^2/m^5] (same as equation 47);
- $\boldsymbol{\rho_a}$ is air density [kg/m^3];
- $\boldsymbol{g}$ is gravitational acceleration (9.822) [m/s^2],
- $\boldsymbol{U_*}$ is friction velocity [m/s]
- $\boldsymbol{U_{*t}}$ is threshold friction velocity [m/s] (is a function of particle size, air, particle density and soil moisture).

The bulk vertical dust flux (F) [μg/m^{2}s] is then calculated as (Marticorena and Bergametti, 1995)

$$F = \alpha\, Q\, E \tag{51}$$

$$\alpha = 10^{[0.134\,(\%clay)]-6} \tag{52}$$

where:

- ***α*** sandblasting efficiency, is an empirical function of soil properties;
- ***E*** is the dust erodibility factor as shown in (Ginoux *et al.*, 2001).

The AFWA scheme uses the theoretical particle size distribution developed by Kok, 2011 for dust simulation and it considers five dust size bins: 0–2.0, 2.0–3.6, 3.6–6.0, 6.0–12.0, and 12.0–20.0 μm. In the last emissiondust emission scheme, Shao 2004, proposed a new size-resolved dust emission scheme (S04):

$$F\,(d_i, d_s) = c_y \eta_f \left[(1-\gamma) + \gamma\sigma_p\right]\left(1+\sigma_p\right) g \frac{Q_{ds}}{u_*^2} \tag{53}$$

$$\gamma = exp[-(u_* - u_{*t})^3] \tag{54}$$

where:

- ***F (d$_i$, d$_s$)*** [μg/m^2] is the dust emission rate for particles of size ***d$_i$*** [μm] generated by the saltation of particles of size ***d$_s$*** [μm];
- ***c$_y$*** is an empiric coefficient [dimensionless];
- ***η$_f$*** is the fraction of dust that can be emitted;
- ***σ$_m$*** is the bombardment efficiency [dimensionless];

- $\boldsymbol{\sigma_p}$ is the ratio between the fraction of free dust and that of aggregated dust that can be released [dimensionless];
- $\boldsymbol{Q_{ds}}$ is the saltation flux [μg/m^2] of particles of size $\boldsymbol{d_s}$ [μm];
- $\boldsymbol{u_*}$ is the friction velocity [m/s];

In Shao's emission scheme, the erodibility factor is only used to constrain the potential emission regions instead of being used to scaling the dust emission directly as in AFWA scheme. The emission of dust of size d_i can be estimated as a weighted average over the particle size range restricted by d_1 and d_2 as

$$F\ (d_i) = \int_{d_1}^{d_2} F\ (d_i, d_s)\ p_s\ (d)\ \delta d \qquad (55)$$

This scheme makes use of the minimally disturbed particle size distribution $p_m\,(d)$ and the fully disturbed particle size distribution $p_f\,(d)$ of the parent soil to constrain the size distribution of the airborne sand and dust particles as

$$p_s(d) = \gamma\ p_m(d) + (1 - \gamma)\ p_f(d) \qquad (56)$$

Finally, Shao *et al.*, 2011 (S11) scheme is a simplification of S04 with γ equal to 1, which means that $p_f\,(d)$ is no longer necessary in the simplified scheme. Both the S04 and the S11 schemes consider four dust size bins: 0 – 2.5, 2.5 – 5.0, 5.0 – 10, and 10.0 – 20.0 μm.

3.3. Results evaluation

3.3.1. Main objectives

The role played by aerosols is one of the main sources of uncertainty in our understanding of climate variability (IPCC, 2007), since the related uncertainty greatly exceeds that of the other mechanisms. Mineral dust in the Earth ecosystem includes the interactions with other physical, chemical, and biogeochemical processes in different scales (Shao *et al.*, 2011). It affects the Earth's climate in distinctive ways, but one of the main effects, is that it influences the atmosphere–Earth system balance by scattering and absorbing short and long wave radiation interfering with the net heating rates balance (Balkanski *et al.*, 2007); the uncertainties in the direct radiative forcing are mainly attributed to their optical properties and their chemical composition (Bi *et al.*, 2010). Furthermore, in addition to direct effects, aerosol indirectly affects the radiative balance by modifying cloud properties (Twomey, 1977; Baker, *et al.*, 1980; Albrecht, 1989; Wang *et al.*, 2010; Huang *et al.*, 2014). Despite the uncertainties related with the wide character of the emissions, the complexity of aerosol chemistry and meteorological conditions, which strongly influence dust outbreaks and its transport, the mineral dust transport modeling is getting increasing attention, allowing for better ascertaining its impact on radiation budget, clouds, air quality and human health, also supported by the improvements in characterizing dust source regions thanks to satellite products (e.g. Ginoux *et al.*, 2012; Rizza, *et al.*, 2017).

The aim of this study is an evaluation of the WRF-Chem model capability to properly simulate the Saharan mineral dust transport episodes

that occurred over the central Mediterranean along a whole year (2017), by a set of two simulations with high spatial resolution of 15 x 15 km. The first simulation included only the dust emissions, in order to quantify the amount of dust optical depth that contributes to the change of local pollution and/or meteorological conditions (e.g. in Italy), while the second simulation, included anthropogenic emissions, to discriminate the relative contribution of the natural and the anthropogenic aerosol sources.

3.3.2. Evaluation of WRF-Chem model: meteorological fields

The evaluation of meteorological parameters have been divided in two steps: the first step considers NCEP/NCAR (Kalnay *et al.*, 1996) reanalysis products to examine spatial patters (i.e. wind speed at 10 m, temperature and relative humidity at 2 m). The second step uses part of the North Africa inland meteorological surface stations, belonging to the global network elaborated by University of Wyoming (Figure 44 - Appendix B. 1), to evaluate winds quantitatively (http://weather.uwyo.edu/surface/meteorogram/europe.shtml).

The following maps show the spatial distribution of the monthly average for parameters at 2 m, as temperature [°C] and relative humidity [%], and the wind speed [m/s] and direction at 10 m (respectively Figure 41, Figure 42 and Figure 43). The left column represents the modeled values (WRF-Chem results - 15 Km grid cells), on the right column instead, are shown the NCEP/NCAR reanalysis products (horizontal resolution of 2.5° × 2.5°). The plots are divided (rows) by month in order to show the four annual seasons development; from top to the bottom, winter (January), spring (April), summer (July) and autumn (October). The WRF-Chem monthly average temperature (Figure 41), compares well with the reanalysis data and its spatial trend. Overall for all season, model and reanalysis results are in a good agreement, showing the same temperature development from the central-east European area to the Mediterranean Sea, near the North Africa coast, emphasizing a temperature-rise in the southeastern direction. There is a slightly quantitative discrepancies between WRF-Chem and the reanalysis, i.e. in July, but mainly October, the modeled temperature displays a minor

overestimate in the western area of Sahel (Senegal, Mauritania and Mali) of about 5 °C (from 25 - 30 °C to 30 - 35 °C interval).

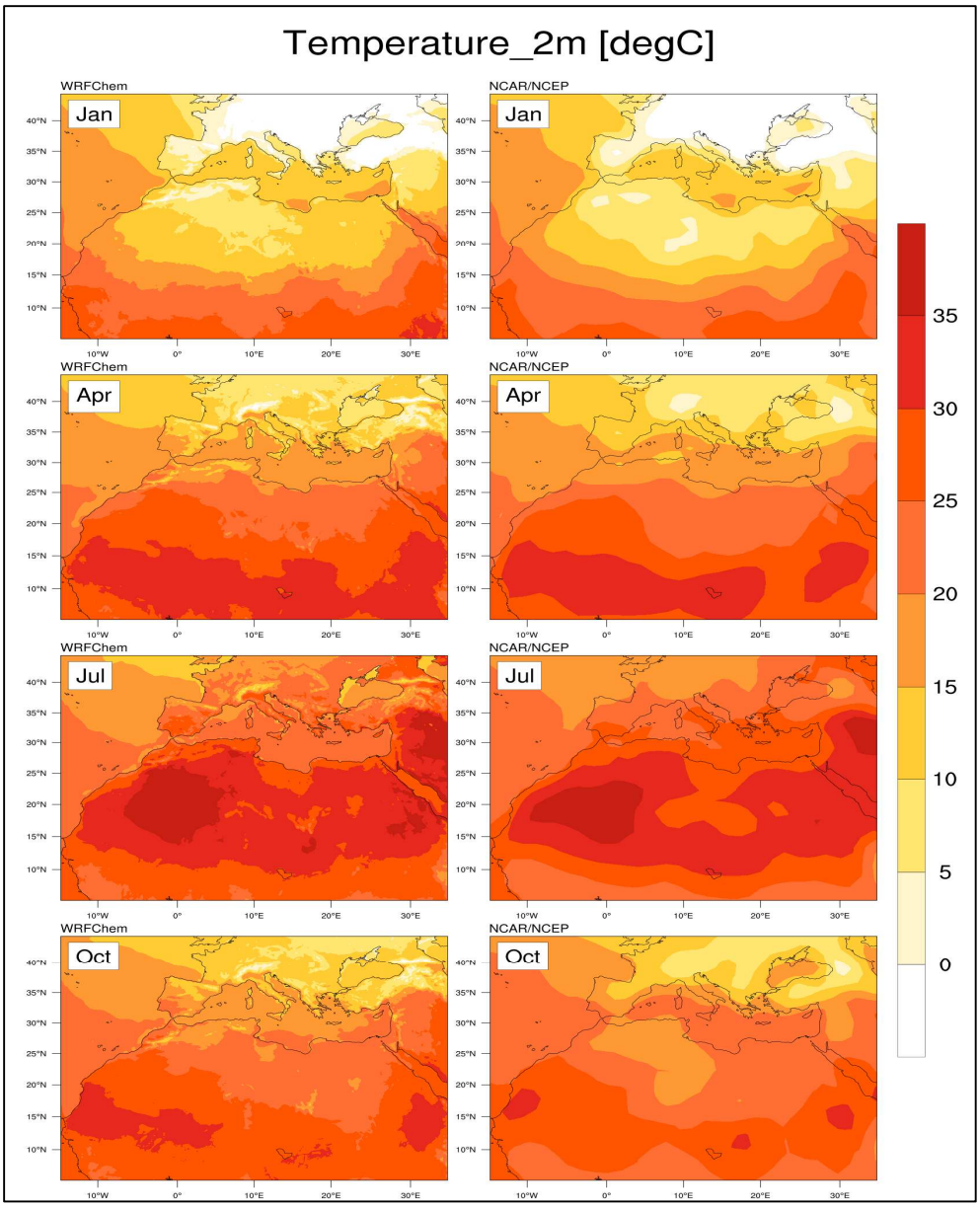

Figure 41: Spatial distribution of monthly average temperature at 2 m [°C] for January (winter), April (spring), July (summer) and October (autumn) 2017. Comparison between the NCAR/NCEP reanalysis (horizontal resolution of 2.5° × 2.5°) (Kalnay *et al.*, 1996) *and the WRF-Chem results on the coarse domain (430×330 grid points - 15 Km grid cells).*

The monthly average of relative humidity, presented in the Figure 42, shows a really suitable correlation, and a very similar spatial tendency, between the model and the reanalysis data; likewise, the changes in the relative humidity magnitude related to the seasonal development, is well represented. As the temperature described in the section before, the two sets of data show a marginally quantitative divergences; the differences are noteworthy in winter (January) and autumn time (October). In the first case, WRF-Chem results overpredict the NCEP/NCAR data by about 10 % (from 10 - 20 to 20 - 30 % interval) in the central-western region of North-Africa (Niger, Mali and south of Algeria), and in the north-western corner of domain (in front of the coast of France and Spain) (from 70 - 80 to 80 - 90 % interval). In October, existing the same situation over the Saharan area as winter time, modeled results overpredict the reanalysis data by about 10 % (from 10 - 20 to 20 - 30 % interval), but in addition, they show an overprediction above the Mediterranean basin always by about 10 % (from 70 - 80 to 80 - 90 % interval). Finally, even the modeled wind speed (black arrows – reference vector = 5 m/s) and wind direction (color contour map) of Figure 43, show an appropriate agreement with the NCEP/NCAR reanalysis, furthermore, the wind direction is better captured than the wind speed; the south-eastern corner of the domain, extending alongside the Middle East (Libya, Egypt, Sudan and Chad), displays a systematic WRF-Chem wind speed overprediction during the different months analyzed. The modeled values show bigger brown area (from 3 to 5 m/s interval), with more red-purple (from 5 to 7 m/s interval) parts within it than the NCEP/NCAR data, as a result of the WRF-Chem overprediction by about 2-4 m/s.

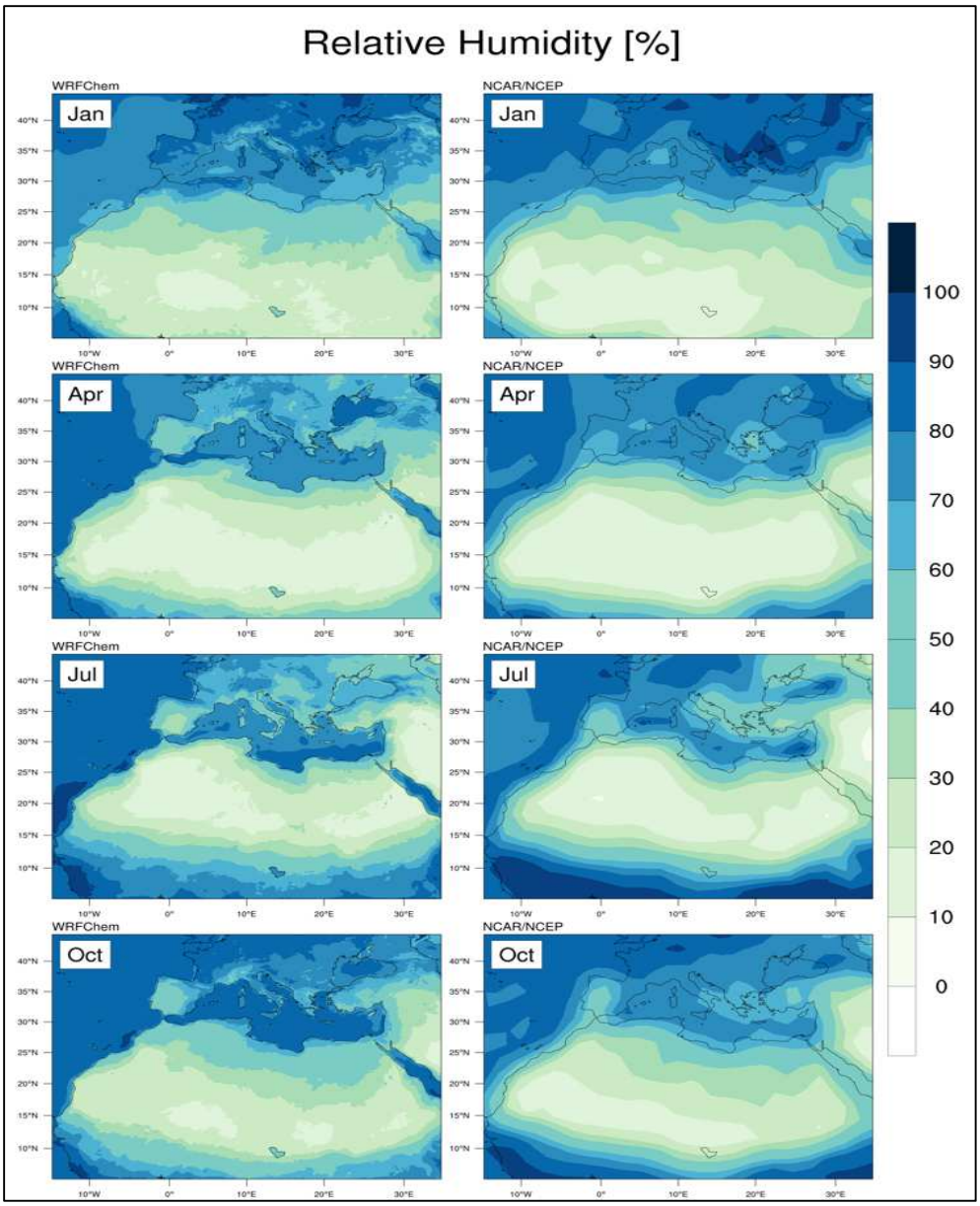

Figure 42: Spatial distribution of monthly relative humidity at 2 m [%] for January (winter), April (spring), July (summer) and October (autumn) 2017. Comparison between the NCAR/NCEP reanalysis (horizontal resolution of 2.5° × 2.5°) (Kalnay *et al.*, 1996) *and the WRF-Chem results on the coarse domain (430×330 grid points - 15 Km grid cells).*

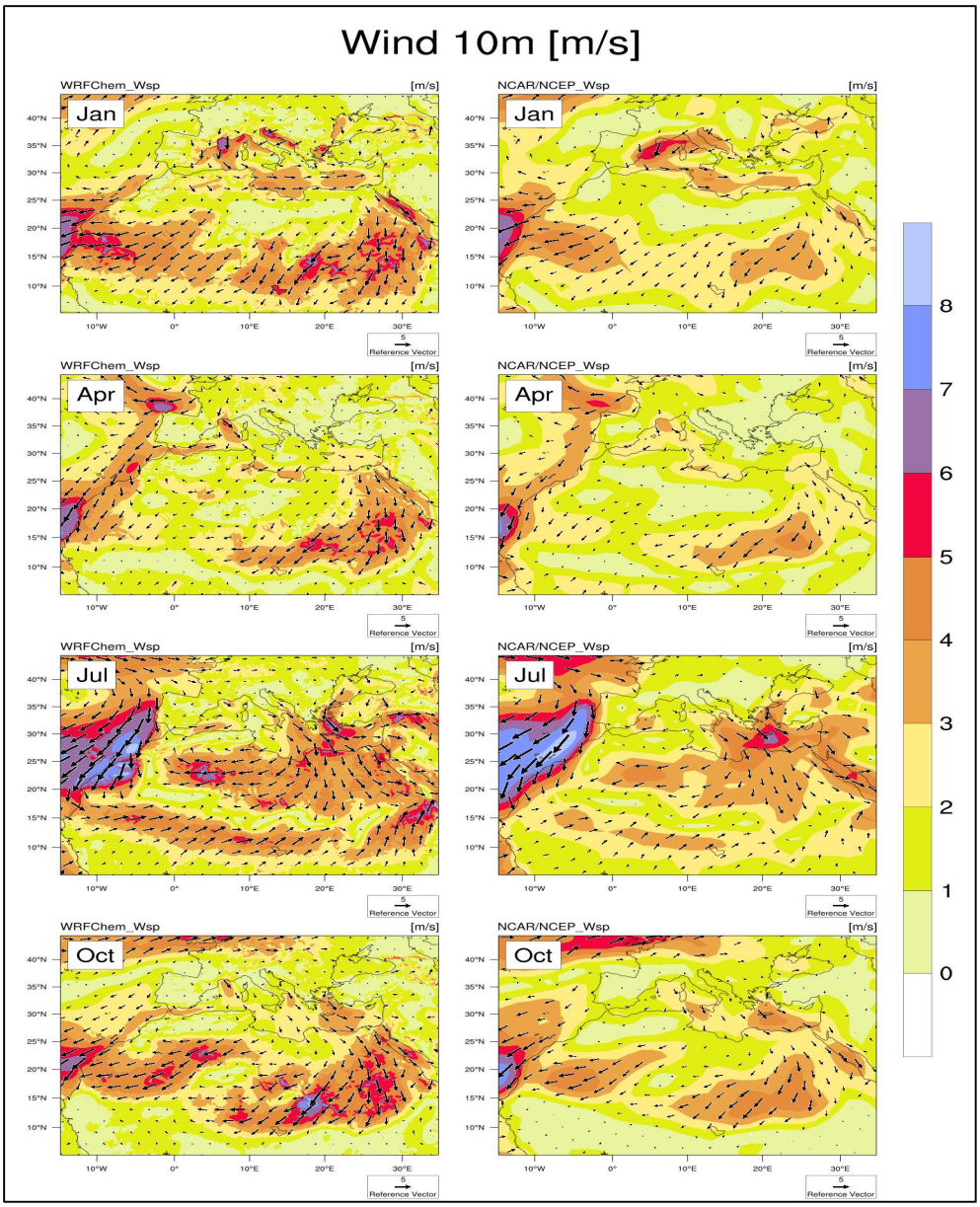

Figure 43: Spatial distribution of winds at 10 m (color contour maps – wind speed [m/s]; black arrows – wind direction – reference vector of 5 m/s) for January (winter), April (spring), July (summer) and October (autumn) 2017. Comparison between the NCAR/NCEP reanalysis (horizontal resolution of 2.5° × 2.5°) (Kalnay *et al.*, 1996) *and the WRF-Chem results on the coarse domain (430×330 grid points - 15 Km grid cells).*

The meteorological parameters examined in the section above (temperature, relative humidity and winds), have been analyzed since the aeolian erosion in semi-arid regions occurs only when a threshold value of the surface friction velocity is reached (U_t – equation 47), its depends on the soil moisture surface features then to the land surface scheme used (Fécan, *et al*, 1999; Rizza, *et al.*, 2017), thus the production and transport of dust aerosols depend crucially on the accuracy of simulated meteorology and the land surface scheme. Assumed that, the Figure 44 reports the nineteen North-Africa inland meteorological surface stations selected to calculate the normalized root mean square error (NRMSE - dimensionless), the correlation coefficient (r - dimensionless) and the normalized mean bias (BIAS - %) of the daily mean of wind speed.

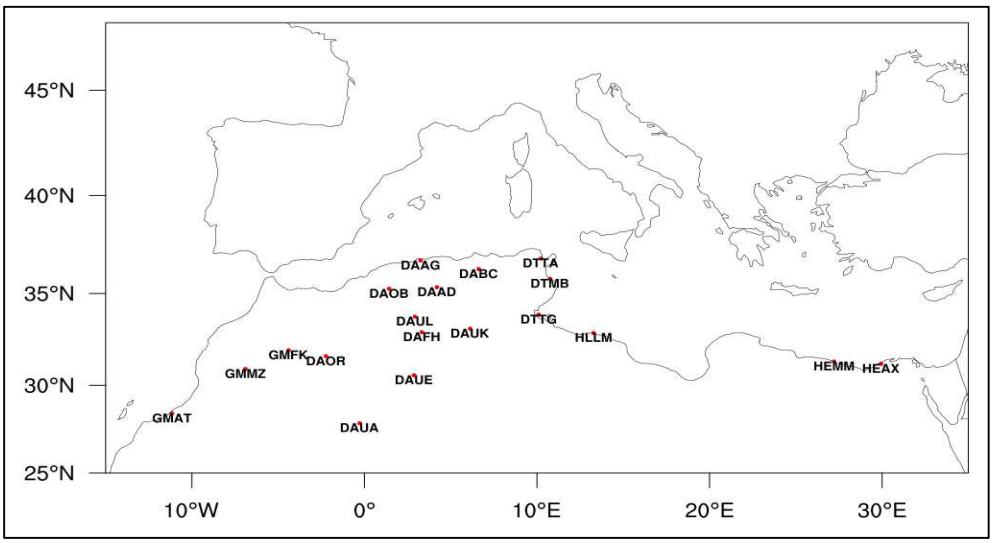

Figure 44: North-Africa meteorological surface stations (elaborated by University of Wyoming) selected to prepare the wind speed statistical analysis (the Appendix B. 1 reports the name, country, code name, longitude, latitude and elevation of the stations).

The bias values fall within a great range between -52 – 60 % (respectively for the stations, DTTG - Gabes, Tunisia and GMMZ - Ouarzazat, Morocco) (Table 14) showing an excessive WRF-Chem wind speed variability compared to the measured data. The best bias results are for the stations named DAUL (Laghouat, Algeria) and DTMB (Habib Bourguiba, Tunisia) with a value of -1.26 and -0.56 %. The normalized root means square error (NRMSE) wind speed model outputs confirm the poor agreement of the bias (Table 14); they show a very high values, all the stations fall within an interval between 51 and 115 (respectively for the stations, DAUA - Adrar Touat, Algeria and GMMZ - Ouarzazat, Morocco), the development is complete by the NRMSE mean that is still a high value as it is about 75. Finally, the correlation coefficient (r) highlights that for every increase, there isn't a positive or negative increase, the two data series just are not related since the all r-values are very close to zero (Table 14), indeed, all the coefficient correlations results fall in an interval between -0.09 (GMAT – Tan-Tan Civ Mil – Morocco) and 0.15 (DTTA - Tunis Carthage, Tunisia).

Table 14: The normalized mean biases [%], the normalized root means square errors [dimensionless] and the correlations coefficients [dimensionless] regarding North-Africa meteorological surface stations (Figure 44 - Appendix B. 1) and WRF-Chem model results. The wind speed values are expressed as daily average values.

	BIAS	**NRMSE**	**r**
DAAD	42.39	104.28	0.10
DAAG	55.30	95.11	0.12
DABC	37.69	91.54	0.10
DAFH	-18.17	65.07	0.08
DAOB	4.58	69.90	0.07
DAOR	15.03	69.70	0.09
DAUA	-9.96	51.73	0.03
DAUE	29.40	80.79	-0.04
DAUK	5.51	59.33	0.09
DAUL	-1.26	71.79	0.04
DTMB	-0.56	65.92	0.15
DTTA	-15.39	57.88	0.15
DTTG	-52.58	70.98	0.02
GMAT	-33.05	56.93	-0.09
GMFK	-17.14	67.04	-0.04
GMMZ	60.53	115.87	0.00

3.3.3. Evaluation of WRF-Chem model: aerosol-phase

The aerosol spatial distribution of the WRF-Chem model is compared in term of total mass distribution with MERRA-2 (Gelaro *et al.*, 2017) reanalysis and optical properties with both MODIS (Salomonson *et al.*, 1989) retrievals and AERONET (Holben *et al.*, 1998) data. The Modern-Era Retrospective Analysis for Research and Applications, version 2 (MERRA-2), is the newest atmospheric reanalysis of the modern satellite era produced by NASA's Global Modeling and Assimilation Office (GMAO) with a spatial resolution of about 50 km in the latitudinal direction. The MERRA-2 covers the period 1980-present, continuing as an ongoing climate analysis. Aerosol assimilation is included throughout the period, using MODIS (MODerate resolution Imaging SpectroRadiometer), MISR (Multi-angle Imaging Spectro Radiometer) and AERONET (Aerosol Robotic NETwork). The aerosols are integrated by using GOCART model, which interact directly with the radiation parameterization, and radiatively coupled with atmospheric model dynamics in the Goddard Earth Observing System Model, Version 5 (GEOS-5) (Shen, Ostrenga and Vollmer, 2015).

Table 15: Dust size bins in WRF-Chem (bin1, bin2, bin3, bin4 and bin5), with the relative interval and effective radius [μm] and the density [kg/m^3].

Type	r-interval	r-eff	Density
bin1	0-1.0	0.73	2500
bin2	1.0-1.8	1.4	2650
bin3	1.8-3.0	2.4	2650
bin4	3.0-6.0	4.5	2650
bin5	6.0-10.0	8	2650

In this study, the MERRA-2 dust column mass density has been compared with the dust column mass density from the "dust only" simulation. The three-month average of the dust column mass density is represented in Figure 45; the months chosen for the average are April, May and June, which are the most active for the dust transport (Ginoux *et al.*, 2012). The modeled dust column results ("TOTDust" is the dust column summed over all the size bins: bin1, bin2, bin3, bin4 and bin5 - Table 15). AS showed in Figure 45 WRF-Chem overpredicts the MERRA-2 reanalysis data by a factor of ten in the most part of North Africa (Sahara Desert) (MERRA-2 = $2x10^{-4}$ kg/m^2; WRF-Chem = $2x10^{-3}$ kg/m^2). This overestimate is also present in the Mediterranean basin with a factor about 2 (MERRA-2 = $2x10^{-4}$ kg/m^2; WRF-Chem = $4x10^{-4}$ kg/m^2).

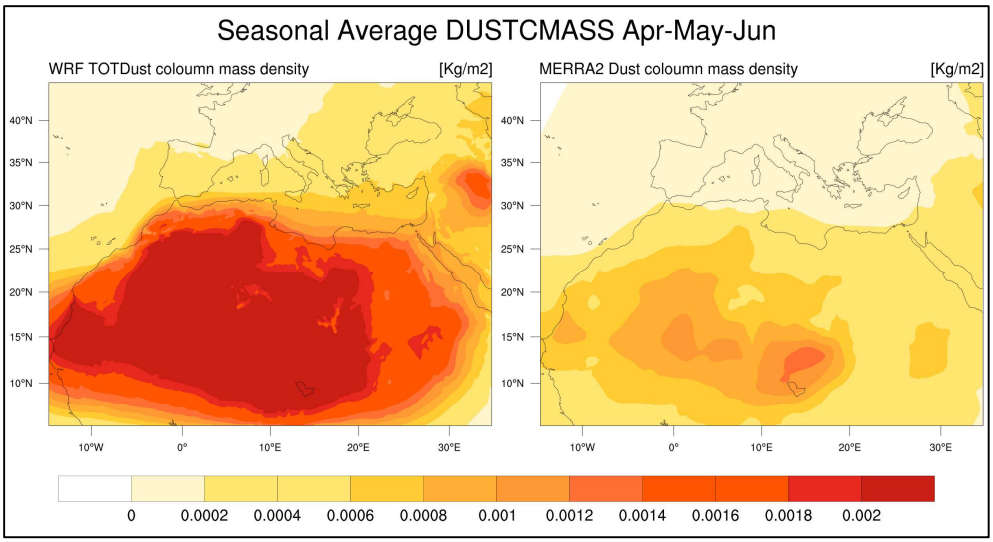

Figure 45: Spatial distribution of three-month average (April, May, June) of the dust column mass density [kg/m^2]; WRF-chem "dust only" (15 x 15 km grid resolutions) simulation evaluated with MERRA-2 (50 x 50 km grid resolutions) dust outputs (Gelaro et al.*, 2017).*

Since the WRF-Chem "dust only" chemistry option (chem_option = 401), does not explicity calculate the aerosol optical properties option (e.g., aer_op_opt, opt_pars_out), its wrfout files do not contain the EXTCOEF fields (extinction coefficient); the vertical sum of each EXTCOEF field multiplied by the layer depth is the computed Aerosol Optical Depth (AOD) at a particular wavelength. In order to calculate the AOD the equation (15) of the Chang *et al.*, 1987, adapted to dust load, have been used

$$\tau_i = \left[\frac{3 \cdot DL_{bin,i}}{2 \cdot \rho_{bin,i} \cdot r_{eff-bin,i}}\right] \qquad (57)$$

where

- $\boldsymbol{DL_{bin,i}}$ is the dust load of the bin i-th [kg/m^2] ;
- $\boldsymbol{\rho_{bin,i}}$ is the density of the bin i-th [kg/m^3];
- $\boldsymbol{r_{eff\text{-}bin,i}}$ is the effective radius of the bin i-th [m].

The AOD value considered to assess the model performances in reproducing dust optical properties, is the sum of the individual contributions (τ_i) for the size bins distribution showed in Table 15. Figure 46, Figure 47 and Figure 48 show the comparison between monthly average AOD of the "dust only" simulation calculated with equation 57 (Figure 46-a, Figure 47-a, and Figure 48-a), the AOD at 550 nm for the simulation considering the EDGAR-HTAP anthropogenic emissions and the MOZART-MOSAIC chemical option (Figure 46-b, Figure 47-b, and Figure 48-b) and MODIS (Figure 46-c, Figure 47-c, and Figure 48-c) product (MOD08_M3 v6.1 - Combined Dark Target and Deep Blue AOD at 0.55 micron for land and ocean) respectively for April (Figure 46), May (Figure 47) and June (Figure 48). The maps show difference in the AOD values between the two WRF-Chem model configurations, since the different emissions type (dust emissions and dust-anthropogenic emissions) and the chemical option used (dust only and MOZART-MOSAIC scheme). The AOD values differences over Europe are noteworthy; i.e. in April and May, less than in June, the circulation shows an increasing of AOD toward the countries, as Greece and Turkey, with a different of 0.1 (AOD_{dust} = 0.2-0.3; AOD_{mozmos} = 0.3-0.4), and in the norther area of the Spain with a difference of 0.3 (AOD_{dust} < 0.1; AOD_{mozmos} = 0.3-0.4). A remarkable similarity is the AOD spatial distribution, all maps ("DUSTONLY", "MOZMOSAIC" and "MODIS") look very related over

North-Africa and regions dominated by dust, showing the same spatial AOD development with higher value located to the well-known dust emitting points (i.e. Bodélé depression and Sahel belt) (Ginoux *et al.*, 2012). In the other hand, a notable difference is the AOD overprediction of the modeled results, in the Saharan region, regardless of the month considered, the WRF-Chem model overestimates AOD by a factor 2 (i.e. ($AOD_{dust/mozmos}$ = 0.2 - 0.5; AOD_{modis} = 0.4 - 1.0). Appendix B. 3, Appendix B. 4 and Appendix B. 5 show the same maps for June, July and August.

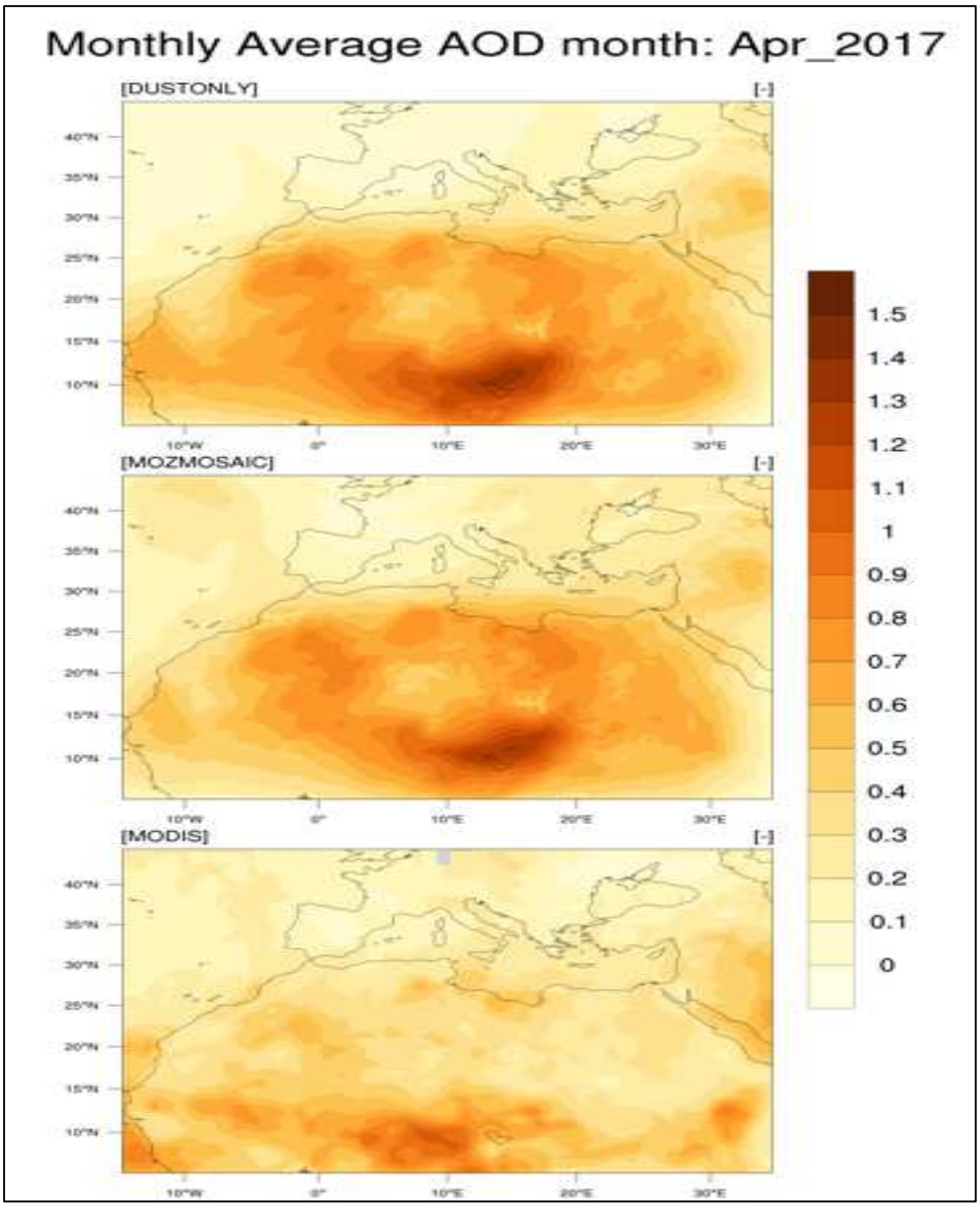

Figure 46: Monthly average AOD [dimensionless] spatial distributions of the "DUSTONLY" simulation (top), the AOD at 550 nm for the simulation considering the "MOZART-MOSAIC" chemical option (center) (15 x 15 km grid resolutions) and MODIS AOD product (1° x 1° grid resolution) for April 2017.

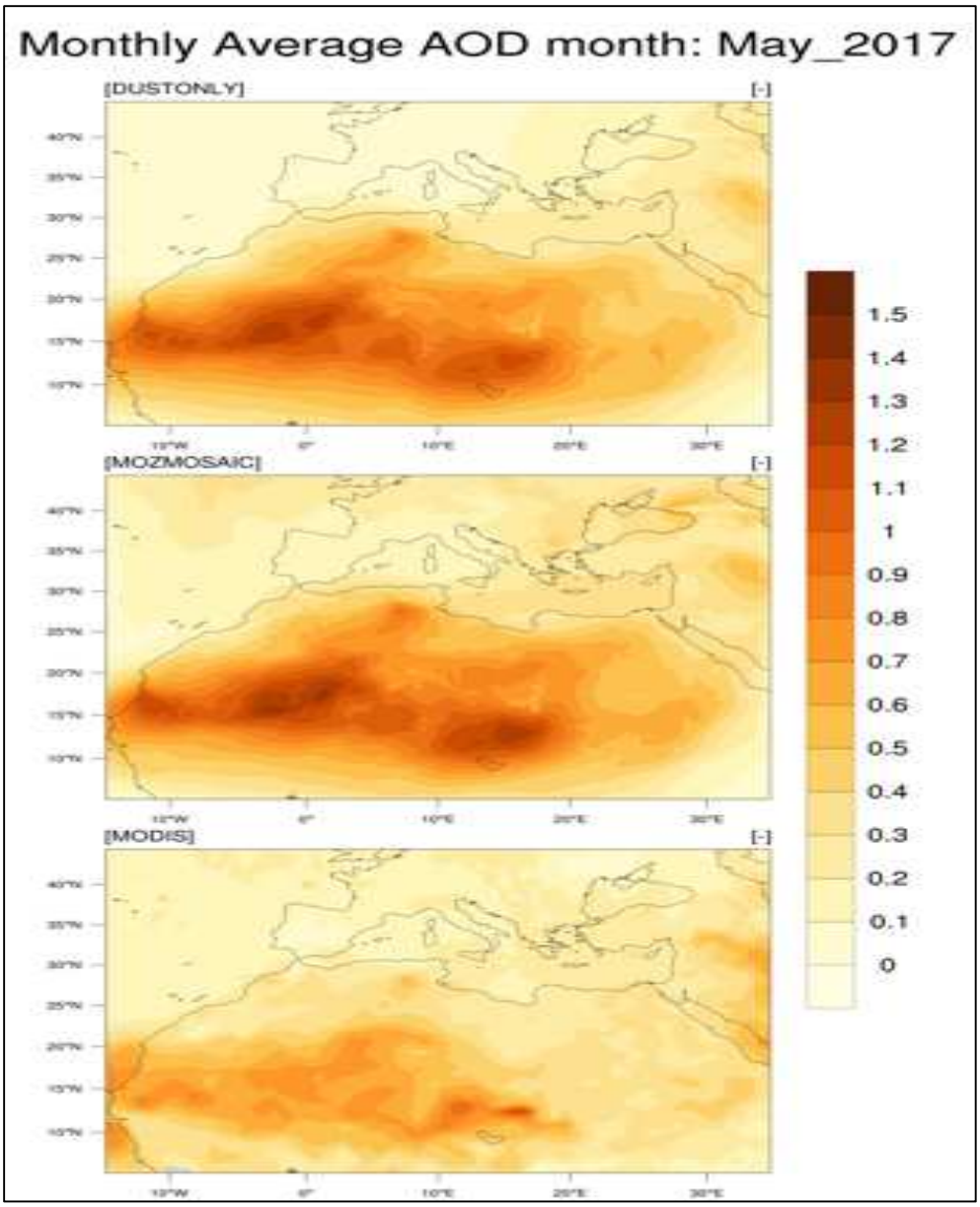

Figure 47: Monthly average AOD [dimensionless] spatial distributions of the "DUSTONLY" simulation (top), the AOD at 550 nm for the simulation considering the "MOZART-MOSAIC" chemical option (center) (15 x 15 km grid resolutions) and MODIS AOD product (1° x 1° grid resolution) for May 2017.

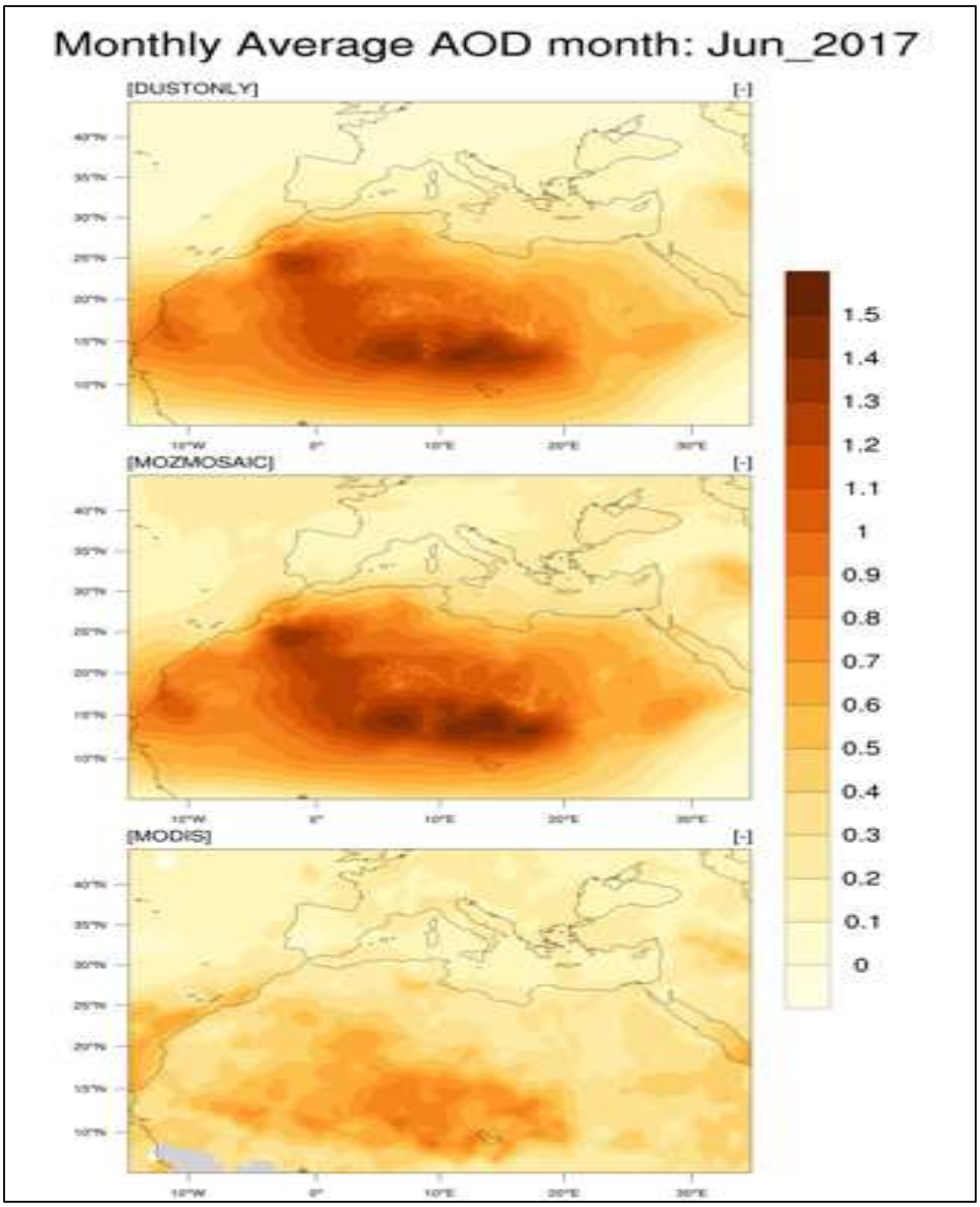

Figure 48: Monthly average AOD [dimensionless] spatial distributions of the "DUSTONLY" simulation (top), the AOD at 550 nm for the simulation considering the "MOZART-MOSAIC" chemical option (center) (15 x 15 km grid resolutions) and MODIS AOD product (1° x 1° grid resolution) for June 2017.

Our consideration regarding these preliminary results, showed in Figure 45, Figure 46, Figure 47 and Figure 48, indicate that: (1) "DUSTONLY" and "MOZMOSAIC" runs show a comparable distribution of mass and AOD optical properties, (2) both distributions evidence a great overprediction in term of mass when compared with MERRA-2 reanalysis, and optical properties when compared with MODIS retrievals. This means that the different chemistry/aerosol phases, GOCART/GOCART for dust-only and MOZART/MOSAIC for the other is producing only small differences in the advection of dust for the period considered in both simulations. This indicate that the amount of dust that is emitted by the GOCART scheme should be in some way reduced.

The last stage of the present study is the evaluation of the daily average of AOD, at 550 nm, of the two simulations described above with the AERONET AOD level 2 (i.e. cloud-screened and quality-assured) at those stations localized in the central and southern Italy, regions where the dust outbreaks are more intense (e.g. Rizza *et al.*, 2016; Rizza, *et al.*, 2017), accomplishing the following requirements: stations that had at least 6 months of level 2 AERONET AOD data. The resulting five stations are: Rome (40.90° N, 12.51° E - Figure 50), Naples (40.83° N, 14.30° E - Figure 51), Lecce (40.33° N, 18.11° E - Figure 52), Aquila (42.36° N, 13.51° E - Appendix B. 6) and Potenza (40.60° N, 15.72° E - Appendix B. 7.) (Figure 49). The black, red and green dots are respectively for AERONET experimental data, "dust only" simulation and "MOZART-MOSAIC" simulation. At Rome station (Figure 50), both simulations overpredict the AOD value specifically in May (AOD_{D17} = 0.9; AOD_{M17} = 1.2; AOD_{AER} =

0.3) August (AOD_{D17} = 0.9; AOD_{M17} = 0.9; AOD_{AER} = 0.3) and December (AOD_{D17} = 0.9; AOD_{M17} = 0.7; AOD_{AER} = 0.2). Naples AERONET station (Figure 51) shows the same trend as Rome but shows the largest overprediction in the beginning of the year (from January to April), where Rome AERONET station has no measurements (AOD_{D17} about 0.3; AOD_{M17} up to 1.2; AOD_{AER} about 0.2). In 4th week of April, Lecce station, shows a noteworthy episode in which all the data are very close (AOD_{D17} = 1.2; AOD_{M17} = 0.9; AOD_{AER} = 1), caused by a dust intrusion in southern Italy (https://worldview.earthdata.nasa.gov) occurred during 26-30 April. The over-prediction discussed above is confirmed also for the AERONET data.

Figure 49: The AERONET stations with at least 6 months of level 2 AERONET AOD data: Rome (40.90° N, 12.51° E - Figure 50), Naples (40.83° N, 14.30° E - Figure 51), Lecce (40.33° N, 18.11° E - Figure 52), Aquila (42.36° N, 13.51° E) and Potenza (40.60° N, 15.72° E).

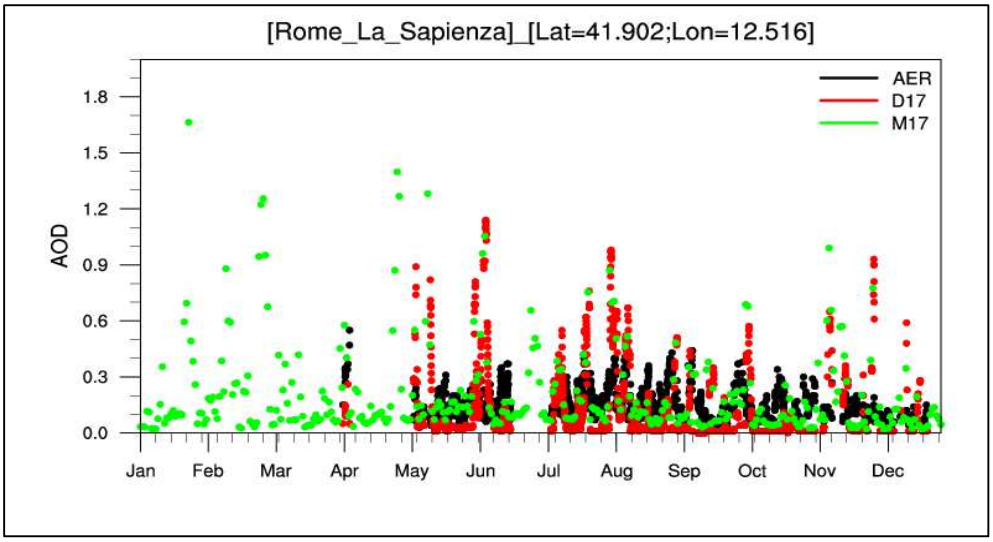

Figure 50: Comparison of the daily average of AOD [dimensionless], at 550 nm, of the two simulations done "dust only" (D17) and "MOZART-MOSAIC" (M17) with the AERONET AOD level 2 at Rome station (AER) (40.90° N, 12.51° E).

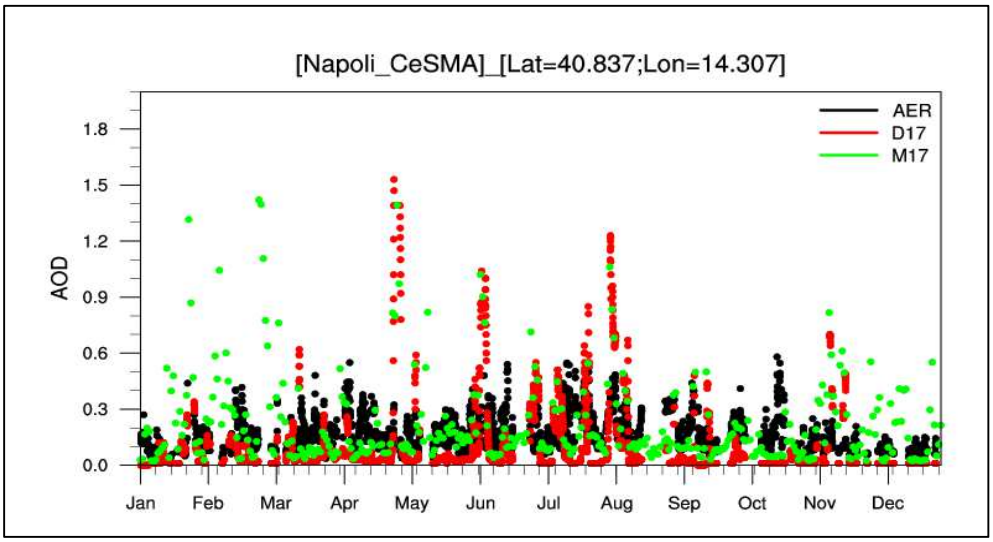

Figure 51: Comparison of the daily average of AOD [dimensionless], at 550 nm, of the two simulations done "dust only" (D17) and "MOZART-MOSAIC" (M17) with the AERONET AOD level 2 at Naples station (AER) (40.83° N, 14.30° E).

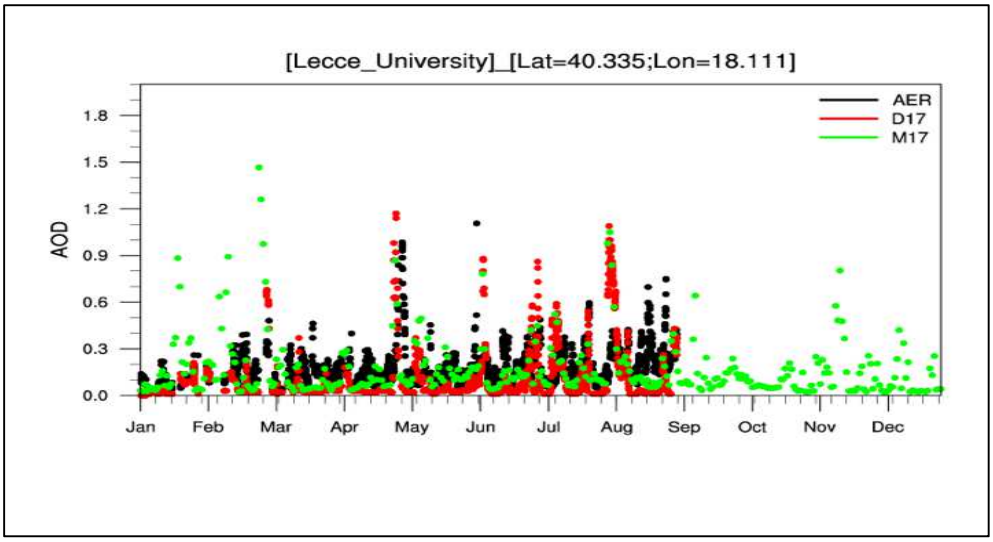

Figure 52: Comparison of the daily average of AOD [dimensionless], at 550 nm, of the two simulations done "dust only" (D17) and "MOZART-MOSAIC" (M17) with the AERONET AOD level 2 at Lecce station (AER) (40.33° N, 18.11° E).

3.4. Conclusions

The aim of the present study was the assessment of Saharan dust intrusion to southern Europe and its effect on air quality in selected Italian cities. This is realized considering two WRF-Chem simulations over one year (from January 1st, 2017 00:00 UTC to January 1st, 2018 00:00 UTC). The model experiment's configuration was to have a first simulation, where only the dust emissions are considered and computed ("dust_only") and then a second, more comprehensive, simulation where the anthropogenic emissions are added to the aerosol loading ("MOZART_MOSAIC").

The evaluation of meteorological parameters has been done by two set of experimental datasets: (1) the NCEP/NCAR reanalysis product has been considered to assess the spatial distribution of simulations results (i.e. the temperature and relative humidity at 2m and the winds at 10 m), and (2) the University of Wyoming surface stations network, to validate one of the most important driving parameters for dust source, the wind speed. The monthly average of temperature, relative humidity and wind showed a great capability of the model to reproduce the experimental data and its spatial trend, realistically reproducing the meteorological parameters within the domain studied; a little difference is present mainly due to the resolution difference between the NCAR/NCEP reanalysis and the resolution of the model; a future development, to avoid those discrepancies, is to use the maps for the comparison with same grid resolution. The FDDA (Four-dimensional data assimilation) technique, used to nudge the meteorological parameters each six hours, is fundamental for a simulation with a time resolution of one year, this is specific by the fact that, despite in this study the nudge was used, the model

wind speed tends to overestimate the experimental data (i.e. daily wind speed bias values fall within a range between -52 – 60 %).

Mineral dust source and transport assessment is based mainly on datasets such as: (1) Modern-Era Retrospective Analysis for Research and Applications, version 2 (MERRA-2), (2) MODerate resolution Imaging SpectroRadiometer product (MODIS) and finally (3) ground-based sun photometer network AERONET (AErosol RObotic NETwork). On the regional scale, the comparison between the modeled AOD, and the dust column mass density, and the field with the corresponding MODIS retrivals and MERRA-2 reanalysis showed that both WRF-Chem simulations ("DUSTONLY" and "MOZMOSAIC") to satisfactorily resolve the spatial evolution, and the Sharan dust sources, but have a great overestimation of dust load and AOD over the North-Africa regions (i.e. by a factor of 10 for the column mass density and by a factor of 2 for the AOD), reflecting a lower overestimate also over the Mediterranean countries. The dust modeled overestimate is also evident in the comparison of both simulations with the daily average of AERONET AOD (550 nm); i.e. Rome and Naples stations have nearly the same year trend where different AOD peaks are captured (May, August and December), but overestimated from both simulations (e.g. May - $AOD_{D17} = 0.9$; $AOD_{M17} = 1.2$; $AOD_{AER} = 0.3$). In the first two months of 2017, M17 ("MOZMOSAIC") simulation shows quite high AOD values in all the AERONET stations considered. This is not evident in the D17 ("DUSTONLY") simulation while AERONET measurements at Lecce and Naples stations recorded lower values. This could be caused by a dust intrusion that is off-set by the M17 simulation; in order to examine this

question, it is necessary to analyze AOD maps for that period (MOODIS/MISR/OMI/MERRA-2). The future developments are quite wide, since the assessment of the (natural and anthropogenic) aerosols in this study is still preliminary; for example, it is essential to evaluate type of data not used by now (e.g. AOD from MERRA-2 and MISR, Aerosol Index from OMI), to better understand the dust outbreaks occurred during the period considered in this study. On the other side, the dust emission mechanisms that are actually implemented in WRF-Chem, namely the GOCART/AFWA and dust-UOC, should be evaluated as well. Other possibility is simply utilizing more AERONET station in order to extrapolate more robust statistical parameters (e.g. RMSE, BIAS and correlation coefficient), but also a more comprehensive experimental dataset, or field campaigns, with a aerosols speciation to discriminate the contribution of natural and anthropogenic aerosols over the Mediterranean basin.

References

Albrecht, B. A. (1989) ‘Aerosols, cloud microphysics, and fractional cloudiness.’, *Science (New York, N.Y.)*. American Association for the Advancement of Science, 245(4923), pp. 1227–30. doi: 10.1126/science.245.4923.1227.

Baker, M. B., Corbin, R. G. and Latham, J. (1980) ‘The influence of entrainment on the evolution of cloud droplet spectra: I. A model of inhomogeneous mixing’, *Quarterly Journal of the Royal Meteorological Society*, 106(449), pp. 581–598. doi: 10.1002/qj.49710644914.

Balkanski, Y. *et al.* (2007) ‘Reevaluation of Mineral aerosol radiative forcings suggests a better agreement with satellite and AERONET data’, *Atmospheric Chemistry and Physics*, 7(1), pp. 81–95. doi: 10.5194/acp-7-81-2007.

Basart, S. *et al.* (2016) ‘Extensive Comparison Between a Set of European Dust Regional Models and Observations in the Western Mediterranean for the Summer 2012 Pre-ChArMEx/TRAQA Campaign’, in *Air Pollution Modeling and its Application XXIV*. Springer, Cham, pp. 79–83. doi: 10.1007/978-3-319-24478-5_13.

Bey, I. *et al.* (2001) ‘Global modeling of tropospheric chemistry with assimilated meteorology: Model description and evaluation’, *Journal of Geophysical Research Atmospheres*. Wiley-Blackwell, 106(D19), pp. 23073–23095. doi: 10.1029/2001JD000807.

Bi, J. *et al.* (2010) ‘Toward characterization of the aerosol optical properties over Loess Plateau of Northwestern China’, *Journal of*

Quantitative Spectroscopy and Radiative Transfer, 112, pp. 346–360. doi: 10.1016/j.jqsrt.2010.09.006.

Brown-Steiner, B., Hess, P. G. and Lin, M. Y. (2015) 'On the capabilities and limitations of GCCM simulations of summertime regional air quality: A diagnostic analysis of ozone and temperature simulations in the US using CESM CAM-Chem', *Atmospheric Environment*. Pergamon, 101, pp. 134–148. doi: 10.1016/j.atmosenv.2014.11.001.

Chameides, W. L. *et al.* (1988) 'The role of biogenic hydrocarbons in urban photochemical smog: Atlanta as a case study.', *Science (New York, N.Y.)*, 241(4872), pp. 1473–5. Available at: http://www.ncbi.nlm.nih.gov/pubmed/3420404 (Accessed: 30 November 2018).

Chang, J. S. *et al.* (1987) 'A three-dimensional Eulerian acid deposition model: Physical concepts and formulation', *Journal of Geophysical Research*. John Wiley & Sons, Ltd, 92(D12), p. 14681. doi: 10.1029/JD092iD12p14681.

Chen, F. and Dudhia, J. (2001) 'Coupling an Advanced Land Surface–Hydrology Model with the Penn State–NCAR MM5 Modeling System. Part I: Model Implementation and Sensitivity', *Monthly Weather Review*, 129(4), pp. 569–585. doi: 10.1175/1520-0493(2001)129<0569:CAALSH>2.0.CO;2.

Curci, G. *et al.* (2009) 'Modelling study of the impact of isoprene and terpene biogenic emissions on European ozone levels', *Atmospheric Environment*. Elsevier Ltd, 43(7), pp. 1444–1455. doi: 10.1016/j.atmosenv.2008.02.070.

'Decreto Legislativo 13 agosto 2010, n. 155' (2010). Available at:

http://moniqa.dii.unipi.it/DLgs-155-del-13-08-2010.pdf (Accessed: 14 November 2018).

Dee, D. P. *et al.* (2011) 'The ERA-Interim reanalysis: Configuration and performance of the data assimilation system', *Quarterly Journal of the Royal Meteorological Society*. Wiley-Blackwell, 137(656), pp. 553–597. doi: 10.1002/qj.828.

Derognat, C. *et al.* (2003) 'Effect of biogenic volatile organic compound emissions on tropospheric chemistry during the Atmospheric Pollution Over the Paris Area (ESQUIF) campaign in the Ile-de-France region', *Journal of Geophysical Research*. John Wiley & Sons, Ltd, 108(D17), p. 8560. doi: 10.1029/2001JD001421.

Deroubaix, A. *et al.* (2013) 'Suitability of OMI aerosol index to reflect mineral dust surface conditions: Preliminary application for studying the link with meningitis epidemics in the Sahel', *Remote Sensing of Environment*, 133, pp. 116–127. doi: 10.1016/j.rse.2013.02.009.

Duane, M. *et al.* (2002) 'Isoprene and its degradation products as strong ozone precursors in Insubria, Northern Italy', *Atmospheric Environment*. Pergamon, 36(24), pp. 3867–3879. doi: 10.1016/S1352-2310(02)00359-X.

Dubovik, O. and King, M. D. (2000) 'A flexible inversion algorithm for retrieval of aerosol optical properties from Sun and sky radiance measurements', *Journal of Geophysical Research Atmospheres*, 105(D16), pp. 20673–20696. doi: 10.1029/2000JD900282.

Duhl, T. *et al.* (2015) 'MEGAN and WRF-CHEM', *Power Point*.

Emmons, L. K. *et al.* (2010) 'Description and evaluation of the Model

for Ozone and Related chemical Tracers, version 4 (MOZART-4)', *Geoscientific Model Development*, 3(1), pp. 43–67. doi: 10.5194/gmd-3-43-2010.

Engelstaedter, S., Tegen, I. and Washington, R. (2006) 'North African dust emissions and transport', *Earth-Science Reviews*, 79(1–2), pp. 73–100. doi: 10.1016/j.earscirev.2006.06.004.

Fast, J. D. *et al.* (2006) 'Evolution of ozone, particulates, and aerosol direct radiative forcing in the vicinity of Houston using a fully coupled meteorology-chemistry-aerosol model', *Journal of Geophysical Research Atmospheres*. John Wiley & Sons, Ltd, 111(21), p. D21305. doi: 10.1029/2005JD006721.

Fécan, F., Marticorena, B. and Bergametti, G. (1999) 'Parametrization of the increase of the aeolian erosion threshold wind friction velocity due to soil moisture for arid and semi-arid areas', *Annales Geophysicae*, 17(1), pp. 149–157. doi: 10.1007/s00585-999-0149-7.

Fiore, A. M. *et al.* (2009) 'Multimodel estimates of intercontinental source-receptor relationships for ozone pollution', *Journal of Geophysical Research Atmospheres*. John Wiley & Sons, Ltd, 114(4), p. D04301. doi: 10.1029/2008JD010816.

Gelaro, R. *et al.* (2017) 'The modern-era retrospective analysis for research and applications, version 2 (MERRA-2)', *Journal of Climate*, 30(14), pp. 5419–5454. doi: 10.1175/JCLI-D-16-0758.1.

Ginoux, P. *et al.* (2001) 'Sources and distributions of dust aerosols simulated with the GOCART model', *Journal of Geophysical Research Atmospheres*. John Wiley & Sons, Ltd, 106(D17), pp. 20255–20273. doi:

10.1029/2000JD000053.

Ginoux, P. *et al.* (2004) 'Long-term simulation of global dust distribution with the GOCART model: Correlation with North Atlantic Oscillation', in *Environmental Modelling and Software*. Elsevier, pp. 113–128. doi: 10.1016/S1364-8152(03)00114-2.

Ginoux, P. *et al.* (2012) 'Global-Scale Attribution of Anthropogenic and Natural Dust Sources and Their Emission Rates Based on Modis Deep Blue Aerosol Products', pp. 1–36. doi: 10.1029/2012RG000388.1.INTRODUCTION.

Gobbi, G. P. *et al.* (2007) 'Classification of aerosol properties derived from AERONET direct sun data', *Atmospheric Chemistry and Physics*, 7(2), pp. 453–458. doi: 10.5194/acp-7-453-2007.

Graedel, T. E. *et al.* (1993) 'A compilation of inventories of emissions to the atmosphere', *Global Biogeochemical Cycles*. Wiley-Blackwell, 7(1), pp. 1–26. doi: 10.1029/92GB02793.

Grell, G. A. *et al.* (2005) 'Fully coupled "online" chemistry within the WRF model', *Atmospheric Environment*, 39(37), pp. 6957–6975. doi: 10.1016/j.atmosenv.2005.04.027.

Grell, G. A. and Freitas, S. R. (2014) 'A scale and aerosol aware stochastic convective parameterization for weather and air quality modeling', *Atmospheric Chemistry and Physics*, 14(10), pp. 5233–5250. doi: 10.5194/acp-14-5233-2014.

Guenther, A. *et al.* (1995) 'A global model of natural volatile organic compound emissions', *Journal of Geophysical Research*, 100(D5), p. 8873. doi: 10.1029/94JD02950.

Guenther, A. *et al.* (1999) 'Isoprene emission estimates and uncertainties for the central African EXPRESSO study domain', *Journal of Geophysical Research: Atmospheres*. Wiley-Blackwell, 104(D23), pp. 30625–30639. doi: 10.1029/1999JD900391.

Guenther, A. *et al.* (2006) 'Estimates of global terrestrial isoprene emissions using MEGAN', *Atmospheric Chemistry and Physics Discussions*, 6(1), pp. 107–173. doi: 10.5194/acpd-6-107-2006.

Guenther, A. *et al.* (2012) 'The model of emissions of gases and aerosols from nature version 2.1 (MEGAN2.1): An extended and updated framework for modeling biogenic emissions', *Geoscientific Model Development*, 5(6), pp. 1471–1492. doi: 10.5194/gmd-5-1471-2012.

Guenther, A. B. *et al.* (1993) 'Isoprene and monoterpene emission rate variability: Model evaluations and sensitivity analyses', *Journal of Geophysical Research*. Wiley-Blackwell, 98(D7), p. 12609. doi: 10.1029/93JD00527.

HEALD, C. L. *et al.* (2009) 'Response of isoprene emission to ambient CO_2 changes and implications for global budgets', *Global Change Biology*. Wiley/Blackwell (10.1111), 15(5), pp. 1127–1140. doi: 10.1111/j.1365-2486.2008.01802.x.

Henne, S. *et al.* (2010) 'Assessment of parameters describing representativeness of air quality in-situ measurement sites', *Atmospheric Chemistry and Physics*, 10(8), pp. 3561–3581. doi: 10.5194/acp-10-3561-2010.

Holben, B. N. *et al.* (1998) 'AERONET—A Federated Instrument Network and Data Archive for Aerosol Characterization', *Remote Sensing of*

Environment. Elsevier, 66(1), pp. 1–16. doi: 10.1016/S0034-4257(98)00031-5.

Huang, J. *et al.* (2014) 'Climate effects of dust aerosols over east asian arid and semiarid regions', *Journal of Geophysical Research*, p. 11,398-11,416. doi: 10.1002/2014JD021796.

Huneeus, N. *et al.* (2011) 'Global dust model intercomparison in AeroCom phase i', *Atmospheric Chemistry and Physics*, 11(15), pp. 7781–7816. doi: 10.5194/acp-11-7781-2011.

Iacono, M. J. *et al.* (2008) 'Radiative forcing by long-lived greenhouse gases: Calculations with the AER radiative transfer models', *Journal of Geophysical Research Atmospheres*. Wiley-Blackwell, 113(13), p. D13103. doi: 10.1029/2008JD009944.

Janjić, Z. I. (1994) 'The Step-Mountain Eta Coordinate Model: Further Developments of the Convection, Viscous Sublayer, and Turbulence Closure Schemes', *Monthly Weather Review*, 122(5), pp. 927–945. doi: 10.1175/1520-0493(1994)122<0927:TSMECM>2.0.CO;2.

Janssens-Maenhout G., Dentener F., Van Aardenne J., Monni S., Pagliari V., Orlandini L., Klimont Z., Kurokawa J., Akimoto H., Ohara T., Wankmueller R., Battye B., Grano D., Zuber A., K. T. . (2012) *EDGAR-HTAP: a Harmonized Gridded Air Pollution Emission Dataset Based on National Inventories, Ispra (Italy): European Commission Publications Office*. doi: ISBN 978-92-79-23122-0, ISSN 1831-9424.

Jiang, X. *et al.* (2018) 'Isoprene emission response to drought and the impact on global atmospheric chemistry', *Atmospheric Environment*. Elsevier, 183(January), pp. 69–83. doi: 10.1016/j.atmosenv.2018.01.026.

Kallos, G. *et al.* (2009) 'Ten-year operational dust forecasting – Recent model development and future plans', *IOP Conference Series: Earth and Environmental Science*. IOP Publishing, 7(1), p. 012012. doi: 10.1088/1755-1307/7/1/012012.

Kalnay, E. *et al.* (1996) 'The NCEP/NCAR 40-year reanalysis project', *Bulletin of the American Meteorological Society*. American Meteorological Society, 77(3), pp. 437–471. doi: 10.1175/1520-0477(1996)077<0437:TNYRP>2.0.CO;2.

Knote, C. *et al.* (2011) 'Towards an online-coupled chemistry-climate model: evaluation of trace gases and aerosols in COSMO-ART', *Geoscientific Model Development*, 4(4), pp. 1077–1102. doi: 10.5194/gmd-4-1077-2011.

Kok, J. F. (2011) 'A scaling theory for the size distribution of emitted dust aerosols suggests climate models underestimate the size of the global dust cycle.', *Proceedings of the National Academy of Sciences of the United States of America*. National Academy of Sciences, 108(3), pp. 1016–21. doi: 10.1073/pnas.1014798108.

Koren, I. *et al.* (2006) 'The Bodélé depression: A single spot in the Sahara that provides most of the mineral dust to the Amazon forest', *Environmental Research Letters*. IOP Publishing, 1(1), p. 014005. doi: 10.1088/1748-9326/1/1/014005.

Von Kuhlmann, R. *et al.* (2004) 'Atmospheric Chemistry and Physics Sensitivities in global scale modeling of isoprene', *Atmos. Chem. Phys*, 4, pp. 1–17. doi: 10.5194/acpd-3-3095-2003.

Kumar, R. *et al.* (2014) 'WRF-Chem simulations of a typical pre-

monsoon dust storm in northern India: Influences on aerosol optical properties and radiation budget', *Atmospheric Chemistry and Physics*, 14(5), pp. 2431–2446. doi: 10.5194/acp-14-2431-2014.

Lamarque, J. F. *et al.* (2012) 'CAM-chem: Description and evaluation of interactive atmospheric chemistry in the Community Earth System Model', *Geoscientific Model Development*, 5(2), pp. 369–411. doi: 10.5194/gmd-5-369-2012.

Leff, B., Ramankutty, N. and Foley, J. A. (2004) 'Geographic distribution of major crops across the world', *Global Biogeochemical Cycles*. Wiley-Blackwell, 18(1), p. n/a-n/a. doi: 10.1029/2003GB002108.

Lin, J. T. *et al.* (2008) 'Global model simulation of summertime U.S. ozone diurnal cycle and its sensitivity to PBL mixing, spatial resolution, and emissions', *Atmospheric Environment*. Pergamon, 42(36), pp. 8470–8483. doi: 10.1016/j.atmosenv.2008.08.012.

Liu, L. *et al.* (2007) 'Photochemical modelling in the Po basin with focus on formaldehyde and ozone', *Atmospheric Chemistry and Physics*, 7(1), pp. 121–137. doi: 10.5194/acp-7-121-2007.

Mahowald, N. M. and Kiehl, L. M. (2003) 'Mineral aerosol and cloud interactions', *Geophysical Research Letters*. John Wiley & Sons, Ltd, 30(9), p. 1475. doi: 10.1029/2002GL016762.

Marticorena, B. and Bergametti, G. (1995) 'Modeling the atmospheric dust cycle: 1. Design of a soil-derived dust emission scheme', *Journal of Geophysical Research*. John Wiley & Sons, Ltd, 100(D8), p. 16415. doi: 10.1029/95JD00690.

Morrison, H., Thompson, G. and Tatarskii, V. (2009) 'Impact of

Cloud Microphysics on the Development of Trailing Stratiform Precipitation in a Simulated Squall Line: Comparison of One- and Two-Moment Schemes', *Monthly Weather Review*, 137(3), pp. 991–1007. doi: 10.1175/2008MWR2556.1.

Moulin, C. *et al.* (1998) 'Satellite climatology of African dust transport in the Mediterranean atmosphere', *Journal of Geophysical Research Atmospheres*. John Wiley & Sons, Ltd, 103(D11), pp. 13137–13144. doi: 10.1029/98JD00171.

Nakanishi, M. and Niino, H. (2006) 'An improved Mellor-Yamada Level-3 model: Its numerical stability and application to a regional prediction of advection fog', *Boundary-Layer Meteorology*. Springer Netherlands, 119(2), pp. 397–407. doi: 10.1007/s10546-005-9030-8.

National Centers for Environmental Prediction - National Weather Service NOAA U. S. Department of Commerce (2005) 'NCEP North American Regional Reanalysis (NARR)'. UCAR/NCAR - Research Data Archive. Available at: https://rda.ucar.edu/datasets/ds608.0/ (Accessed: 25 November 2018).

Ncep (2000) 'NCEP FNL Operational Model Global Tropospheric Analyses, continuing from July 1999', *Dataset ds083. 2 published by the CISL Data Support …*. Boulder, CO: Research Data Archive at the National Center for Atmospheric Research, Computational and Information Systems Laboratory, p. doi: 10.5065/D6M043C6.

Niu, G. Y. *et al.* (2011) 'The community Noah land surface model with multiparameterization options (Noah-MP): 1. Model description and evaluation with local-scale measurements', *Journal of Geophysical Research*

Atmospheres. John Wiley & Sons, Ltd, 116(12), p. D12109. doi: 10.1029/2010JD015139.

NOMADSS (2013) 'NOMADSS-Operations Plan', pp. 1–35.

Pegoraro, E. *et al.* (2004) 'Effect of elevated CO2 concentration and vapour pressure deficit on isoprene emission from leaves of Populus deltoides during drought', *Functional Plant Biology*, 31(12), pp. 1137–1147. doi: 10.1071/FP04142.

Pierce, T. *et al.* (1998) 'Influence of increased isoprene emissions on regional ozone modeling', *Journal of Geophysical Research: Atmospheres*. Wiley-Blackwell, 103(D19), pp. 25611–25629. doi: 10.1029/98JD01804.

Pierce, T. E. and Waldruff, P. S. (1991) 'PC-BEIS: A Personal Computer Version of the Biogenic Emissions Inventory System', *Journal of the Air & Waste Management Association*. Taylor & Francis Group, 41(7), pp. 937–941. doi: 10.1080/10473289.1991.10466890.

Prospero, J. M. *et al.* (2002) 'Environmental characterization of global sources of atmospheric soil dust identified with the Nimbus 7 Total Ozone Mapping Spectrometer (TOMS) absorbing aerosol product', *Reviews of Geophysics*. John Wiley & Sons, Ltd, 40(1), p. 1002. doi: 10.1029/2000RG000095.

Rizza, U. *et al.* (2016) 'WRF-CHEM SIMULATION OF A SAHARAN DUST OUTBREAK OVER THE MEDITERRANEAN REGIONS', *Ciência e Natura*, 38(0), p. 330. doi: 10.5902/2179460X20249.

Rizza, U., Miglietta, M. M., *et al.* (2017) 'Sensitivity of WRF-Chem model to land surface schemes: Assessment in a severe dust outbreak episode in the Central Mediterranean (Apulia Region)', *Atmospheric Research*.

Elsevier, 201(August 2017), pp. 168–180. doi: 10.1016/j.atmosres.2017.10.022.

Rizza, U., Barnaba, F., *et al.* (2017) 'WRF-Chem model simulations of a dust outbreak over the central Mediterranean and comparison with multi-sensor desert dust observations', *Atmospheric Chemistry and Physics*, 17(1), pp. 93–115. doi: 10.5194/acp-17-93-2017.

Sakulyanontvittaya, T. *et al.* (2008) 'Monoterpene and sesquiterpene emission estimates for the United States', *Environmental Science and Technology*, 42(5), pp. 1623–1629. doi: 10.1021/es702274e.

Salomonson, V. V. *et al.* (1989) 'MODIS: advanced facility instrument for studies of the Earth as a system', *IEEE Transactions on Geoscience and Remote Sensing*, 27(2), pp. 145–153. doi: 10.1109/36.20292.

Shao, Y. (2001) 'A model for mineral dust emission', *Journal of Geophysical Research Atmospheres*. John Wiley & Sons, Ltd, 106(D17), pp. 20239–20254. doi: 10.1029/2001JD900171.

Shao, Y. (2004) 'Simplification of a dust emission scheme and comparison with data', *Journal of Geophysical Research*. John Wiley & Sons, Ltd, 109(D10), p. D10202. doi: 10.1029/2003JD004372.

Shao, Y. *et al.* (2011) 'Dust cycle: An emerging core theme in Earth system science', *Aeolian Research*. Elsevier, 2(4), pp. 181–204. doi: 10.1016/J.AEOLIA.2011.02.001.

Shao, Y. *et al.* (2011) 'Parameterization of size-resolved dust emission and validation with measurements', *Journal of Geophysical Research*. John Wiley & Sons, Ltd, 116(D8), p. D08203. doi: 10.1029/2010JD014527.

Shen, S., Ostrenga, D. and Vollmer, B. (2015) 'Long-Term Global Aerosol Products from NASA Reanalysis MERRA-2 Available at GES DISC', *American Geophysical Union, Fall Meeting 2015, abstract id. A31D-0095*. Available at: http://adsabs.harvard.edu/abs/2015AGUFM.A31D0095S (Accessed: 13 February 2019).

Simpson, D. *et al.* (1999) 'Inventorying emissions from nature', *Journal of Geophysical Research*, 104(D7), pp. 8113–8152.

Solmon, F. *et al.* (2004) 'Isoprene and monoterpenes biogenic emissions in France: modeling and impact during a regional pollution episode', *Atmospheric Environment*. Pergamon, 38(23), pp. 3853–3865. doi: 10.1016/J.ATMOSENV.2004.03.054.

Tanaka, T. Y. and Chiba, M. (2006) 'A numerical study of the contributions of dust source regions to the global dust budget', *Global and Planetary Change*. Elsevier, 52(1–4), pp. 88–104. doi: 10.1016/j.gloplacha.2006.02.002.

Trainer, M. *et al.* (1987) 'Models and observations of the impact of natural hydrocarbons on rural ozone', *Nature*. Nature Publishing Group, 329(6141), pp. 705–707. doi: 10.1038/329705a0.

Twomey, S. (1977) 'The Influence of Pollution on the Shortwave Albedo of Clouds', *Journal of the Atmospheric Sciences*, 34(7), pp. 1149–1152. doi: 10.1175/1520-0469(1977)034<1149:TIOPOT>2.0.CO;2.

Velikova, V. *et al.* (2005) 'Isoprene decreases the concentration of nitric oxide in leaves exposed to elevated ozone', *New Phytologist*. Wiley/Blackwell (10.1111), 166(2), pp. 419–425. doi: 10.1111/j.1469-8137.2005.01409.x.

Wagner, W. P., Nemecek-Marshall, M. and Fall, R. (1999) *Three Distinct Phases of Isoprene Formation during Growth and Sporulation of Bacillus subtilis*, *JOURNAL OF BACTERIOLOGY*. Available at: http://jb.asm.org/ (Accessed: 18 October 2018).

Wang, W. *et al.* (2010) 'Dusty cloud properties and radiative forcing over dust source and downwind regions derived from A-Train data during the Pacific Dust Experiment', *Journal of Geophysical Research Atmospheres*. John Wiley & Sons, Ltd, 115(24), p. D00H35. doi: 10.1029/2010JD014109.

Wang, W., Li, T. and Li, Y. P. (2000) 'Hybrid algorithm for the design of DOE in uniform illumination', *Optics Communications*, 181(4), pp. 261–265. doi: 10.5194/acp-17-93-2017.

Washington, R. *et al.* (2006) 'African climate change: Taking the shorter route', *Bulletin of the American Meteorological Society*. American Meteorological Society, 87(10), pp. 1355–1366. doi: 10.1175/BAMS-87-10-1355.

White, B. R. (1979) 'soil transport by winds on Mars', *Journal of Geophysical Research*. John Wiley & Sons, Ltd, 84(B9), p. 4643. doi: 10.1029/JB084iB09p04643.

Wiedinmyer, C. *et al.* (2011) 'The Fire INventory from NCAR (FINN): A high resolution global model to estimate the emissions from open burning', *Geoscientific Model Development*, 4(3), pp. 625–641. doi: 10.5194/gmd-4-625-2011.

Zaveri, R. A. *et al.* (2008) 'Model for Simulating Aerosol Interactions and Chemistry (MOSAIC)', *Journal of Geophysical Research Atmospheres*, 113(13), pp. 1–29. doi: 10.1029/2007JD008782.

Zhao, C. *et al.* (2010) 'The spatial distribution of mineral dust and its shortwave radiative forcing over North Africa: modeling sensitivities to dust emissions and aerosol size treatments', *Atmos. Chem. Phys*, 10, pp. 8821–8838. doi: 10.5194/acp-10-8821-2010.

Appendix A.

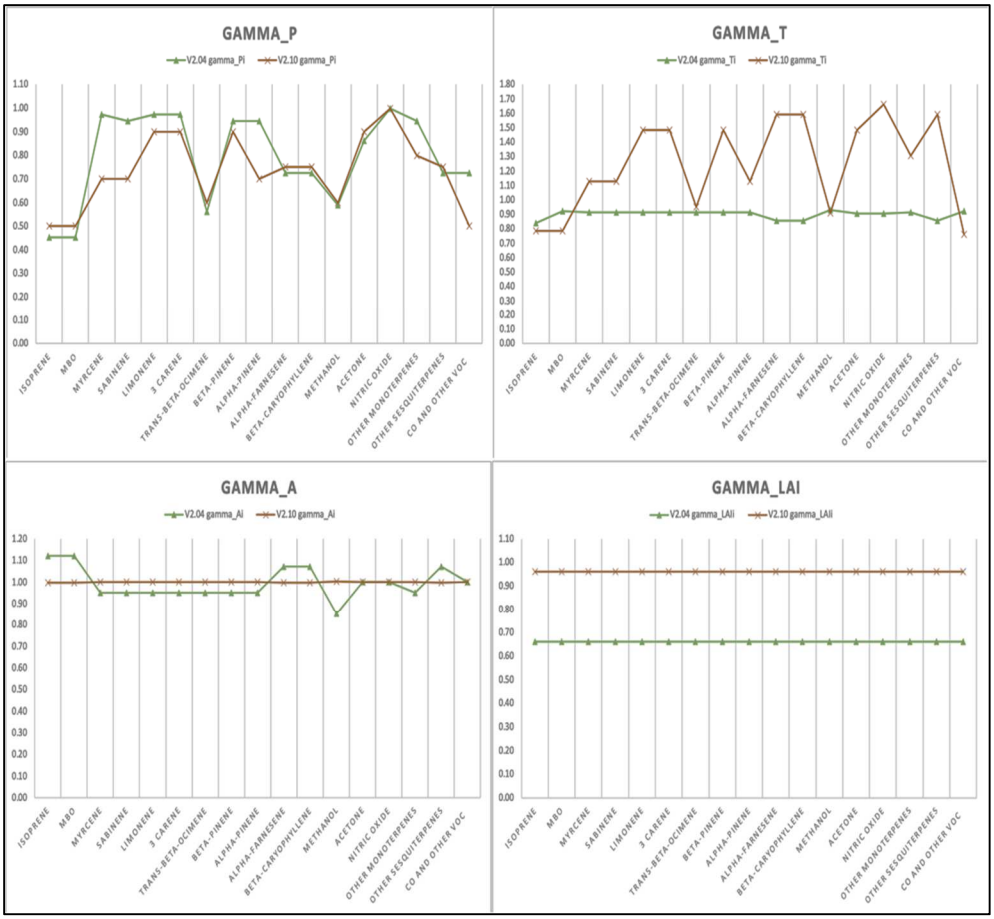

Appendix A. 1: The comparison of the emission activity factors γ_P (GAMMA_P), γ_T (GAMMA_T), γ_{age} (GAMMA_A), and γ_{LAI} (GAMMA_LAI) between version 2.04 and version 2.10 of MEGAN equation. The factors are referred to the city of Kiev (50.45° N – 30.50° E) for August 13th (12:00 UTC), 2015.

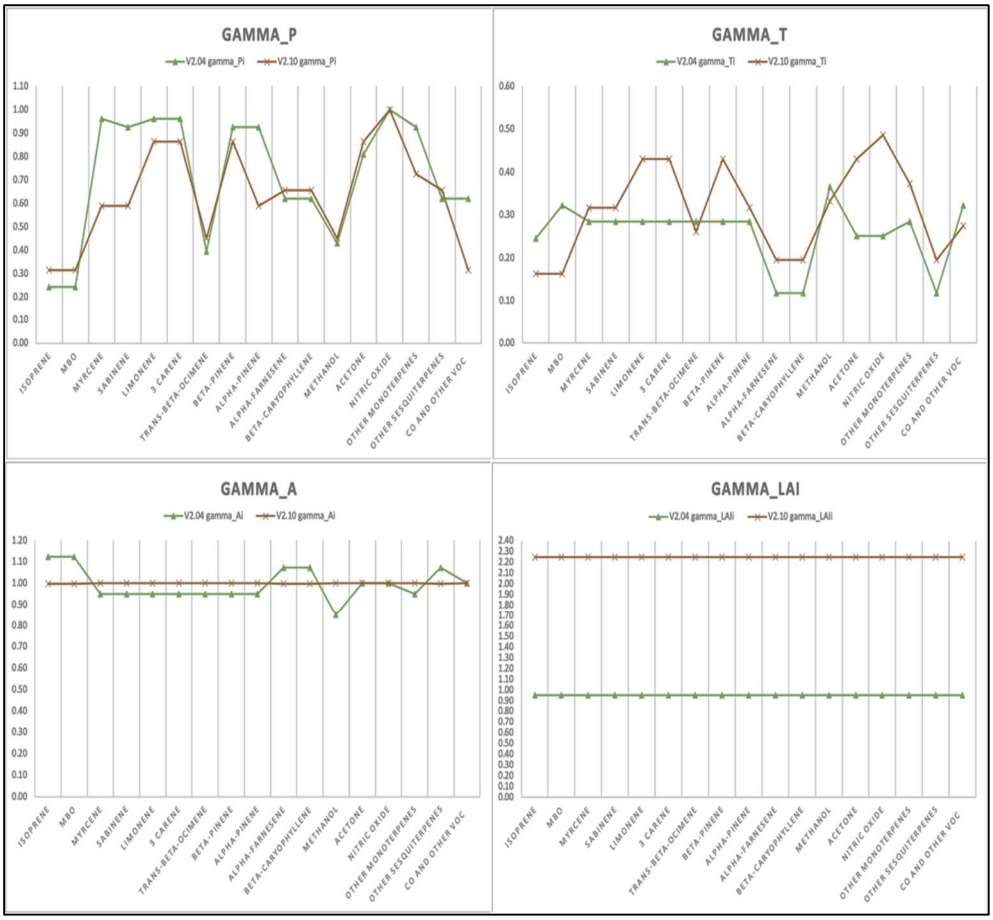

Appendix A. 2: The comparison of the emission activity factors γ_P (GAMMA_P), γ_T (GAMMA_T), γ_{age} (GAMMA_A), and γ_{LAI} (GAMMA_LAI) between version 2.04 and version 2.10 of MEGAN equation. The factors are referred to the city of Porto (41.15° N – 8.63° W) for August 13th (12:00 UTC), 2015.

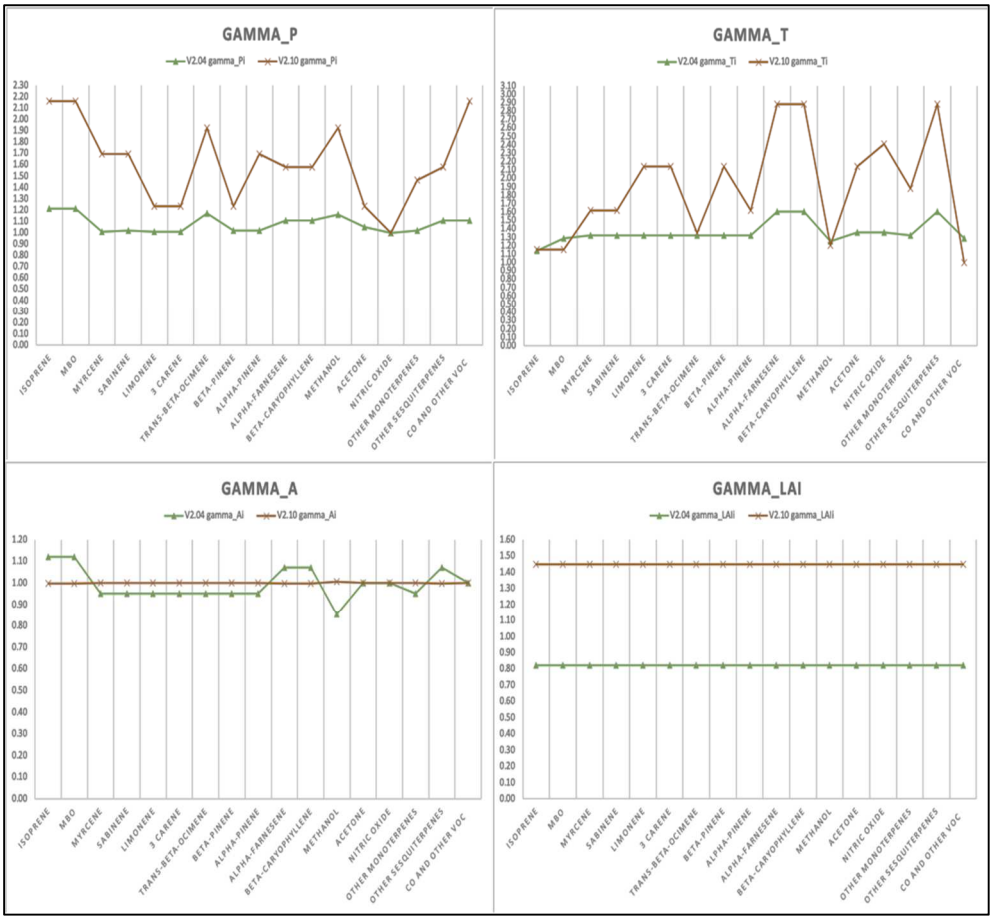

Appendix A. 3: The comparison of the emission activity factors γ_P (GAMMA_P), γ_T (GAMMA_T), γ_{age} (GAMMA_A), and γ_{LAI} (GAMMA_LAI) between version 2.04 and version 2.10 of MEGAN equation. The factors are referred to the city of Zagreb (45.80° N – 16° E) for August 13th (12:00 UTC), 2015.

Appendix A. 4: The normalized mean biases [%], the normalized root means square errors [dimensionless] and the correlations coefficients [dimensionless] regarding AIRBASE datasets and WRF-Chem model. The ozone concentrations are the daytime (from 7 am to 6 pm) weekly average from August 1st (00:00 UTC) to August 16th (00:00 UTC), 2015. (ME = "Megan_V2.04"; MG = "Megan_Gamma"; GP = "Megan_Gamma_PFT"; IP = "Megan_Gamma_PFTISO").

	O_3		
	SUBURBAN	**URBAN**	**RURAL**
N_stations	**515**	**890**	**576**
bias_ME	25.9	30.8	14.6
bias_MG	36.7	41.4	23.8
bias_GP	36.8	41.5	23.9
bias_IP	35.7	40.7	23.3
nrmse_ME	0.338	0.393	0.227
nrmse_MG	0.428	0.490	0.298
nrmse_GP	0.429	0.491	0.298
nrmse_IP	0.419	0.483	0.293
r_ME	0.752	0.751	0.843
r_MG	0.773	0.762	0.854
r_GP	0.773	0.762	0.854
r_IP	0.777	0.765	0.857

Appendix A. 5: The normalized mean biases [%], the normalized root means square errors [dimensionless] and the correlations coefficients [dimensionless] regarding AIRBASE datasets and WRF-Chem model. The nitrogen dioxide concentrations are the daytime (from 7 am to 6 pm) weekly average from August 1st (00:00 UTC) to August 16th (00:00 UTC), 2015. (ME = "Megan_V2.04"; MG = "Megan_Gamma"; GP = "Megan_Gamma_PFT"; IP = "Megan_Gamma_PFTISO").

	NO_2		
	SUBURBAN	**URBAN**	**RURAL**
N_stations	642	1621	512
bias_ME	-39.63	-62.73	-2.93
bias_MG	-39.16	-62.31	-2.20
bias_GP	-39.32	-62.41	-2.50
bias_IP	-39.12	-62.31	-2.12
nrmse_ME	0.908	0.942	0.948
nrmse_MG	0.907	0.940	0.950
nrmse_GP	0.908	0.941	0.950
nrmse_IP	0.907	0.940	0.950
r_ME	0.210	0.224	0.394
r_MG	0.209	0.222	0.394
r_GP	0.209	0.222	0.394
r_IP	0.209	0.222	0.395

Appendix A. 6: The normalized mean biases [%], the normalized root means square errors [dimensionless] and the correlations coefficients [dimensionless] regarding AIRBASE datasets and WRF-Chem model. The carbon monoxide concentrations are the daytime (from 7 am to 6 pm) weekly average from August 1st (00:00 UTC) to August 16th (00:00 UTC), 2015. (ME = "Megan_V2.04"; MG = "Megan_Gamma"; GP = "Megan_Gamma_PFT"; IP = "Megan_Gamma_PFTISO").

	CO		
	SUBURBAN	**URBAN**	**RURAL**
N_stations	150	618	75
bias_ME	-27.30	-30.98	-27.79
bias_MG	-23.91	-27.49	-24.36
bias_GP	-23.87	-27.44	-24.31
bias_IP	-24.12	-27.61	-24.58
nrmse_ME	0.710	0.617	0.709
nrmse_MG	0.699	0.599	0.699
nrmse_GP	0.698	0.599	0.699
nrmse_IP	0.700	0.601	0.701
r_ME	0.109	0.231	-0.030
r_MG	0.124	0.244	-0.015
r_GP	0.124	0.245	-0.016
r_IP	0.122	0.238	-0.019

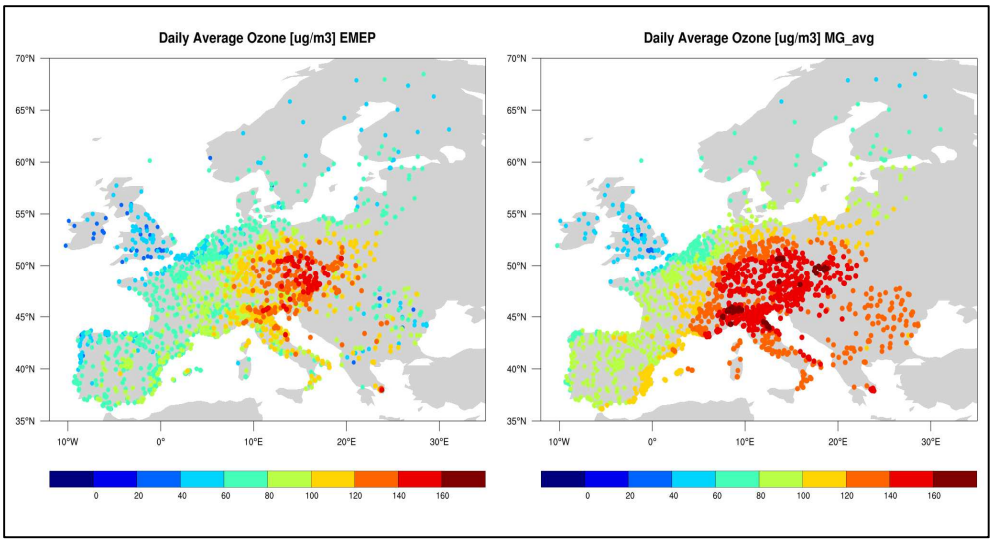

Appendix A. 7: The spatial resolutions of the mean day time (7 am – 6 pm UTC) concentrations for O_3 over the whole simulation period (from August 10th 00:00 UTC to 16th 00:00 UTC, 2015) for simulations with the activity factors (γ_i) updated ("Megan_Gamma"), compared against the AIRBASE dataset (1981 stations) (12 km x 12 km resolution).

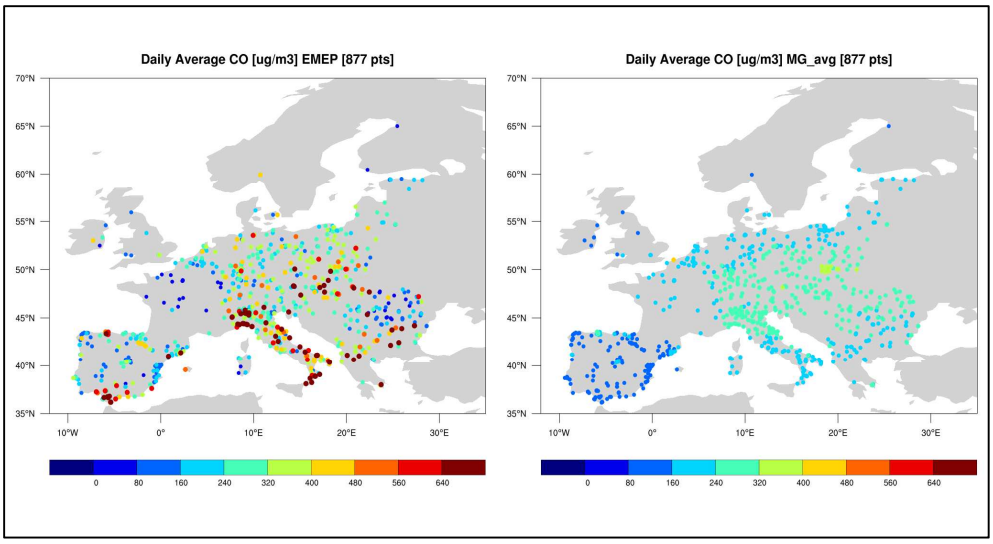

Appendix A. 8: The spatial resolutions of the mean day time (7 am – 6 pm UTC) concentrations for CO over the whole simulation period (from August 10th 00:00 UTC to 16th 00:00 UTC, 2015) for simulations with the activity factors (γ_i) updated ("Megan_Gamma"), compared against the AIRBASE dataset (12 km x 12 km resolution).

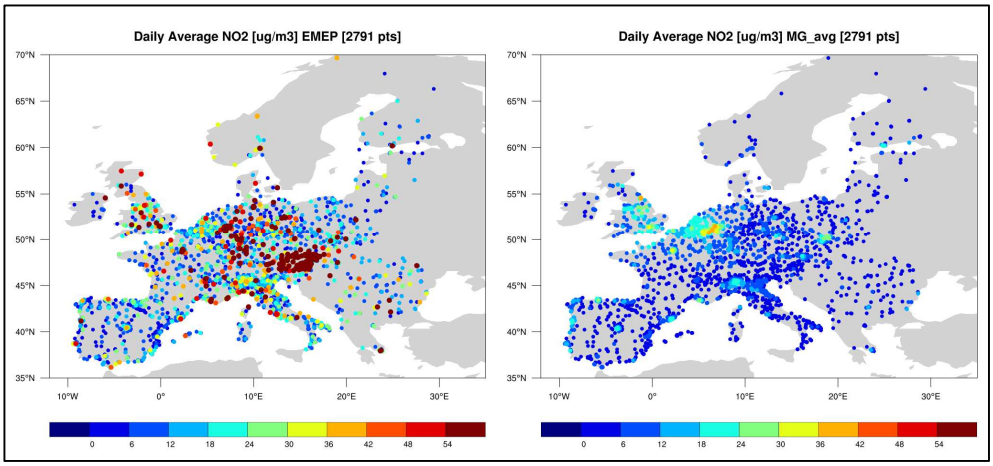

Appendix A. 9: The spatial resolutions of the mean day time (7 am – 6 pm UTC) concentrations for NO_2 over the whole simulation period (from August 10th 00:00 UTC to 16th 00:00 UTC, 2015) for simulations with the activity factors (γ_i) updated ("Megan_Gamma"), compared against the AIRBASE dataset (12 km x 12 km resolution).

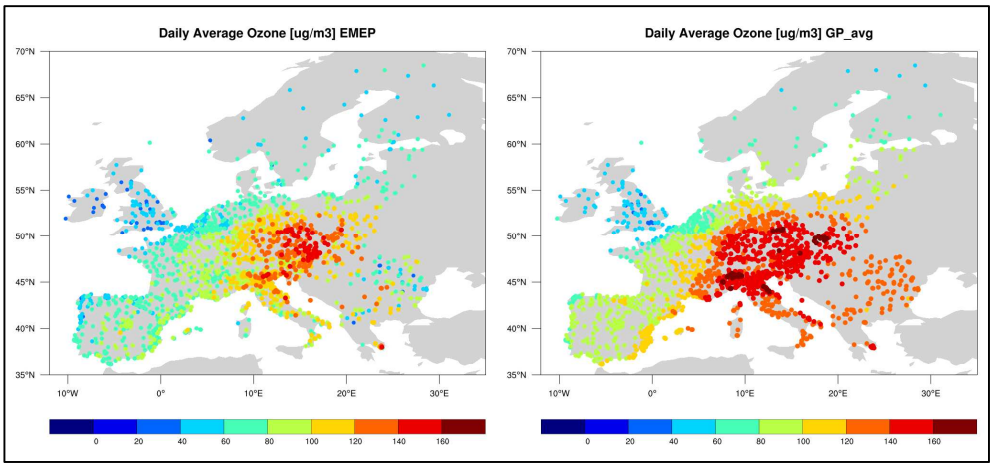

Appendix A. 10: The spatial resolutions of the mean day time (7 am – 6 pm UTC) concentrations for O_3 over the whole simulation period (from August 10th 00:00 UTC to 16th 00:00 UTC, 2015) for simulations with the activity factors (γ_i) and the PFTs emission factors updated ("Megan_Gamma_PFT"), compared against the AIRBASE dataset (1981 stations) (12 km x 12 km resolution).

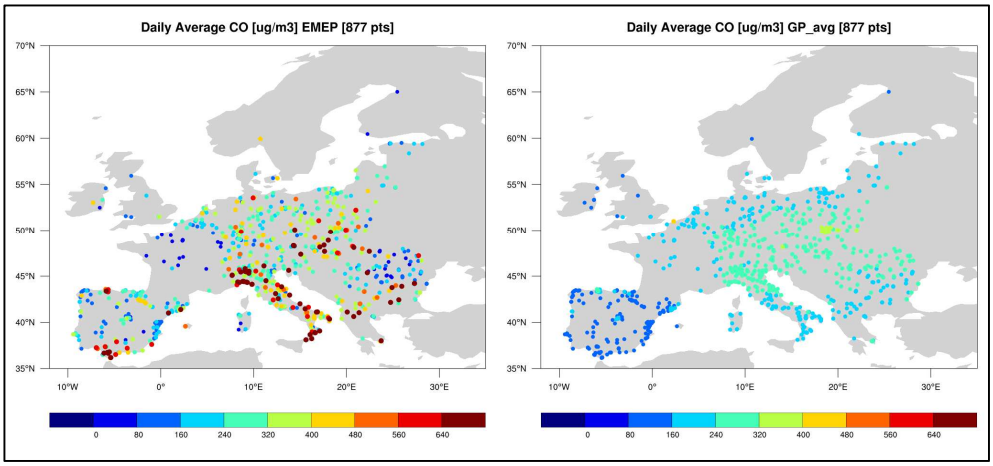

Appendix A. 11: The spatial resolutions of the mean day time (7 am – 6 pm UTC) concentrations for CO over the whole simulation period (from August 10th 00:00 UTC to 16th 00:00 UTC, 2015) for simulations with the activity factors (γ_i) and the PFTs emission factors updated ("Megan_Gamma_PFT"), compared against the AIRBASE dataset (12 km x 12 km resolution).

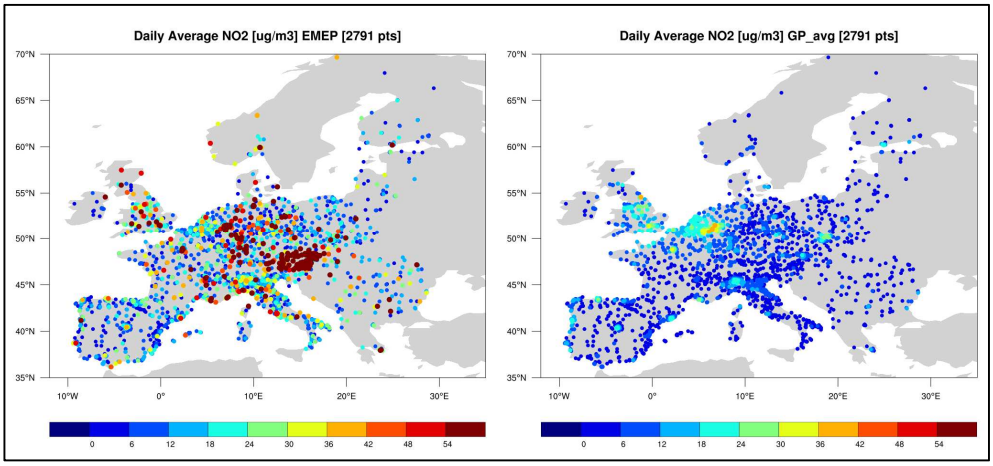

Appendix A. 12: The spatial resolutions of the mean day time (7 am – 6 pm UTC) concentrations for NO_2 over the whole simulation period (from August 10th 00:00 UTC to 16th 00:00 UTC, 2015) for simulations with the activity factors (γ_i) and the PFTs emission factors updated ("Megan_Gamma_PFT"), compared against the AIRBASE dataset (12 km x 12 km resolution).

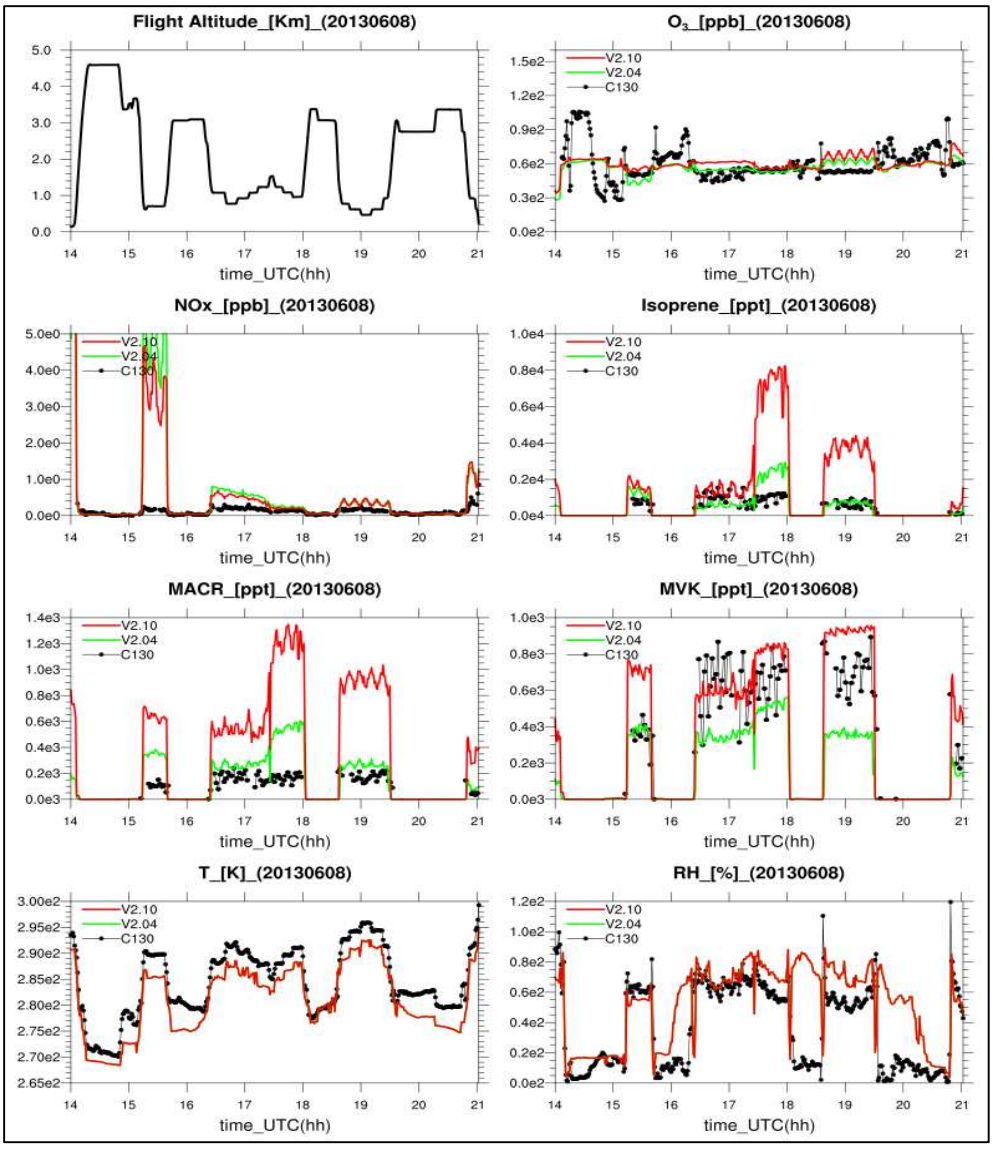

Appendix A. 13: The flight altitude [km], the temperature [K], the relative humidity [%] and the concentrations of ozone [ppb], NO_x (NO_2 + NO) [ppb], isoprene [ppt], MACR (methacrolein) [ppt] and MVK (methyl vinyl ketone) [ppt] for the third NOMADSS flight (rf03). The black line is referred to the C-130 aircraft measurements, the green one indicates the WRF-Chem model results using MEGAN version 2.04 (control simulation - "Megan_V2.04") and the red line is the WRF-Chem simulation with MEGAN updated to the version 2.10 ("Megan_Gamma_PFTISO").

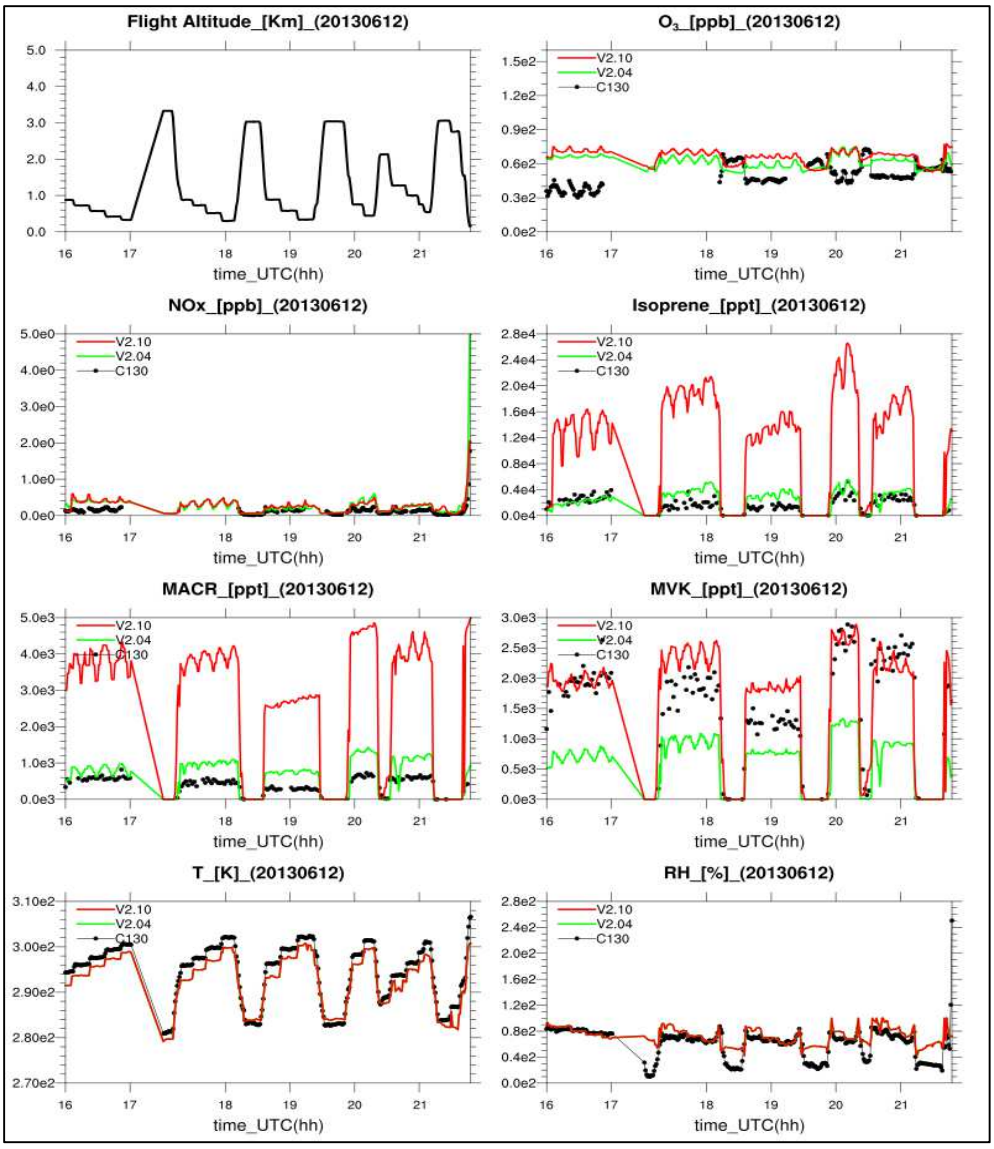

Appendix A. 14: The flight altitude [km], the temperature [K], the relative humidity [%] and the concentrations of ozone [ppb], NO_x (NO_2 + NO) [ppb], isoprene [ppt], MACR (methacrolein) [ppt] and MVK (methyl vinyl ketone) [ppt] for the fourth NOMADSS flight (rf04). The black line is referred to the C-130 aircraft measurements, the green one indicates the WRF-Chem model results using MEGAN version 2.04 (control simulation - "Megan_V2.04") and the red line is the WRF-Chem simulation with MEGAN updated to the version 2.10 ("Megan_Gamma_PFTISO").

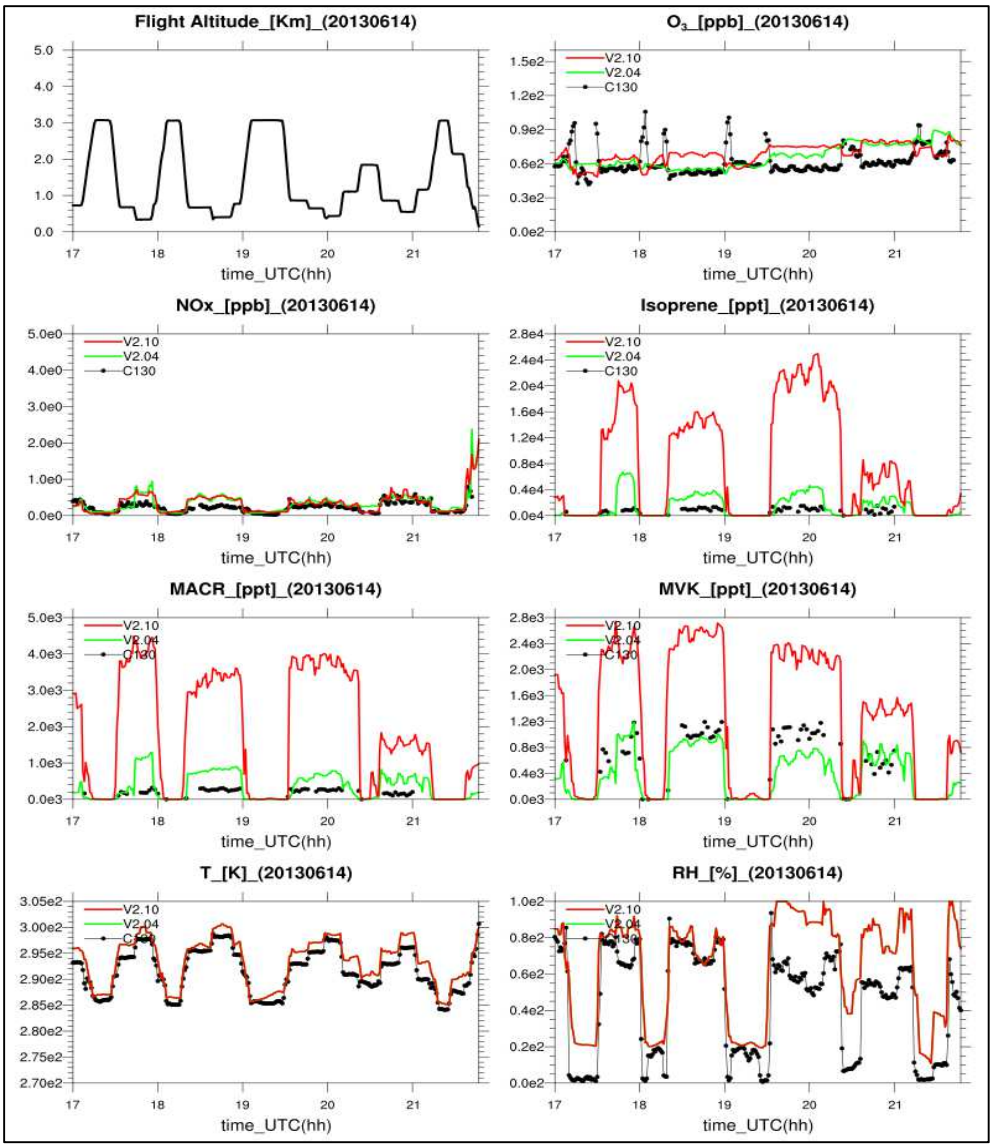

Appendix A. 15: The flight altitude [km], the temperature [K], the relative humidity [%] and the concentrations of ozone [ppb], NO_x (NO_2 + NO) [ppb], isoprene [ppt], MACR (methacrolein) [ppt] and MVK (methyl vinyl ketone) [ppt] for the fifth NOMADSS flight (rf05). The black line is referred to the C-130 aircraft measurements, the green one indicates the WRF-Chem model results using MEGAN version 2.04 (control simulation - "Megan_V2.04") and the red line is the WRF-Chem simulation with MEGAN updated to the version 2.10 ("Megan_Gamma_PFTISO").

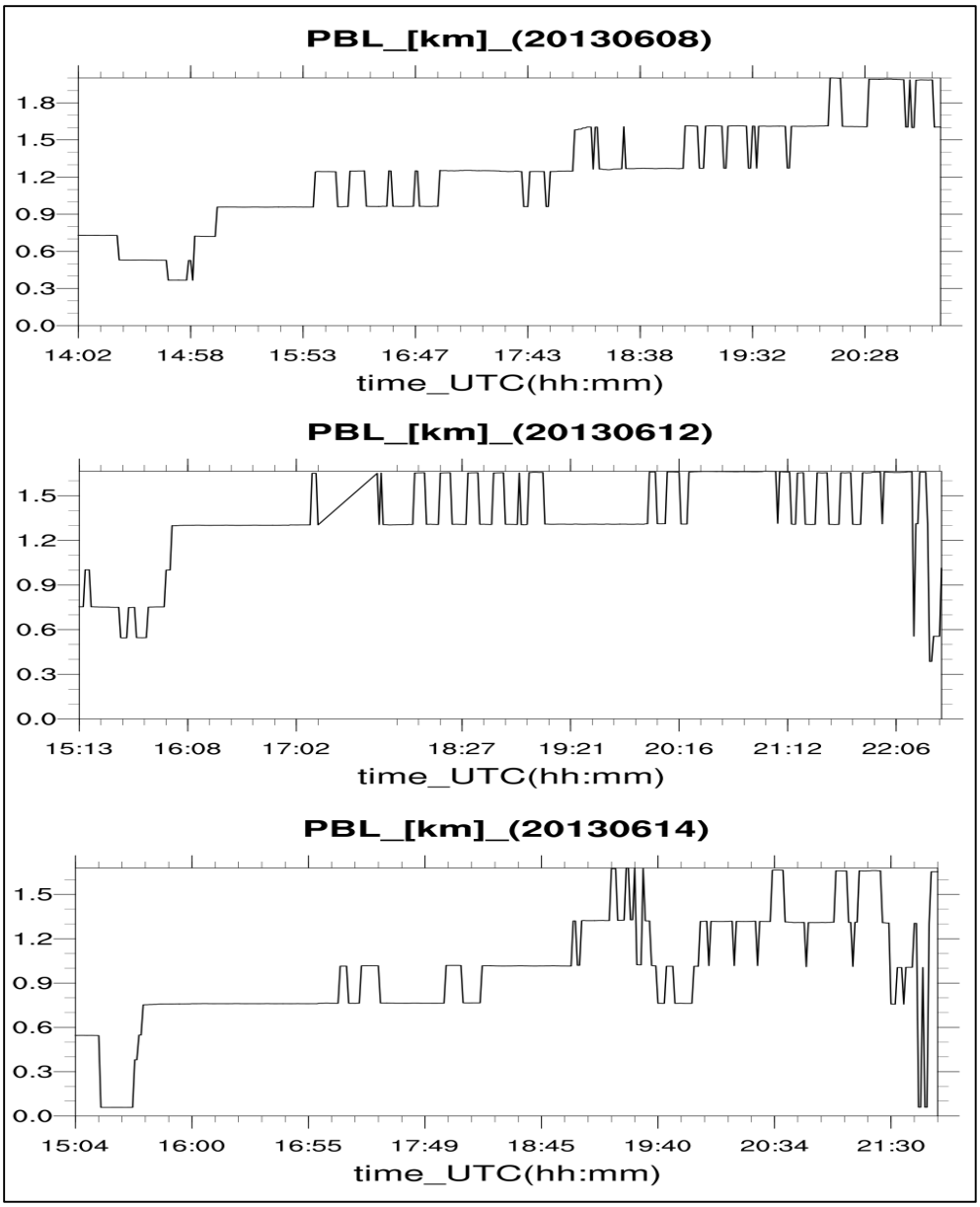

Appendix A. 16: PBL altitude [km], for rf02, rf03 and rf04 NOMADSS flights track. They occurred, respectively, on June 8th (14 – 21 UTC; 9 - 16 US central time zone), June 12th (15 – 22 UTC; 10 – 17 US central time zone) and June 14th (15 – 22 UTC; 10 – 17 US central time zone), 2013.

Appendix B.

Appendix B. 1: North-Africa meteorological surface stations (elaborated by University of Wyoming) selected to prepare the wind speed statistical analysis (referred to Figure 44).

Station name	Code	LAT	LON	ELEV (m)
BOU-SAADA, Algeria	DAAD	35.33N	4.20E	461
DAR-EL-BEIDA HOUARI, Algeria	DAAG	36.72N	3.25E	25
CONSTANTINE EL BEY, Algeria	DABC	36.28N	6.62E	694
TILREMPT HASSI, Algeria	DAFH	32.93N	3.32E	774
TIARET, Algeria	DAOB	35.25N	1.43E	1127
BECHAR OUAKDA, Algeria	DAOR	31.62N	2.23W	773
ADRAR TOUAT, Algeria	DAUA	27.88N	0.28W	263
EL GOLEA, Algeria	DAUE	30.57N	2.87E	397
TOUGGOURT SIDI MAHD, Algeria	DAUK	33.12N	6.13E	85
LAGHOUAT, Algeria	DAUL	33.77N	2.93E	765
HABIB BOURGUIBA, Tunisia	DTMB	35.77N	10.75E	2
TUNIS CARTHAGE, Tunisia	DTTA	36.83N	10.23E	4
GABES, Tunisia	DTTG	33.88N	10.10E	5
TAN-TAN CIV MIL, Morocco	GMAT	28.43N	11.15W	200
ER-RACHIDIA RMA, Morocco	GMFK	31.95N	4.40W	1045
OUARZAZATE, Morocco	GMMZ	30.92N	6.90W	1140
ALEXANDRIA NOUZHA, Egypt	HEAX	31.20N	29.95E	7
MERSA MATRUH, Egypt	HEMM	31.33N	27.22E	30
TRIPOLI MITIGA, Libyan	HLLM	32.89N	13.28E	11

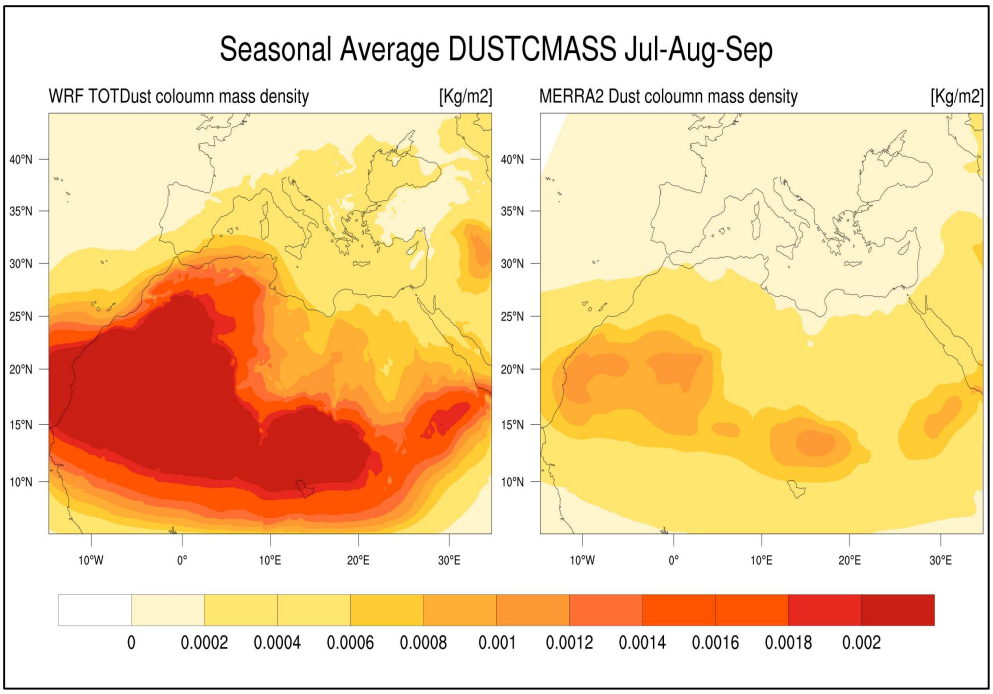

Appendix B. 2: Spatial distribution of three-month average (July, August, September 2017) of the dust column mass density [kg/m^2]; WRF-chem "dust only" (15 x 15 km grid resolutions) simulation evaluated with MERRA-2 (50 x 50 km grid resolutions) dust outputs (Gelaro et al.*, 2017).*

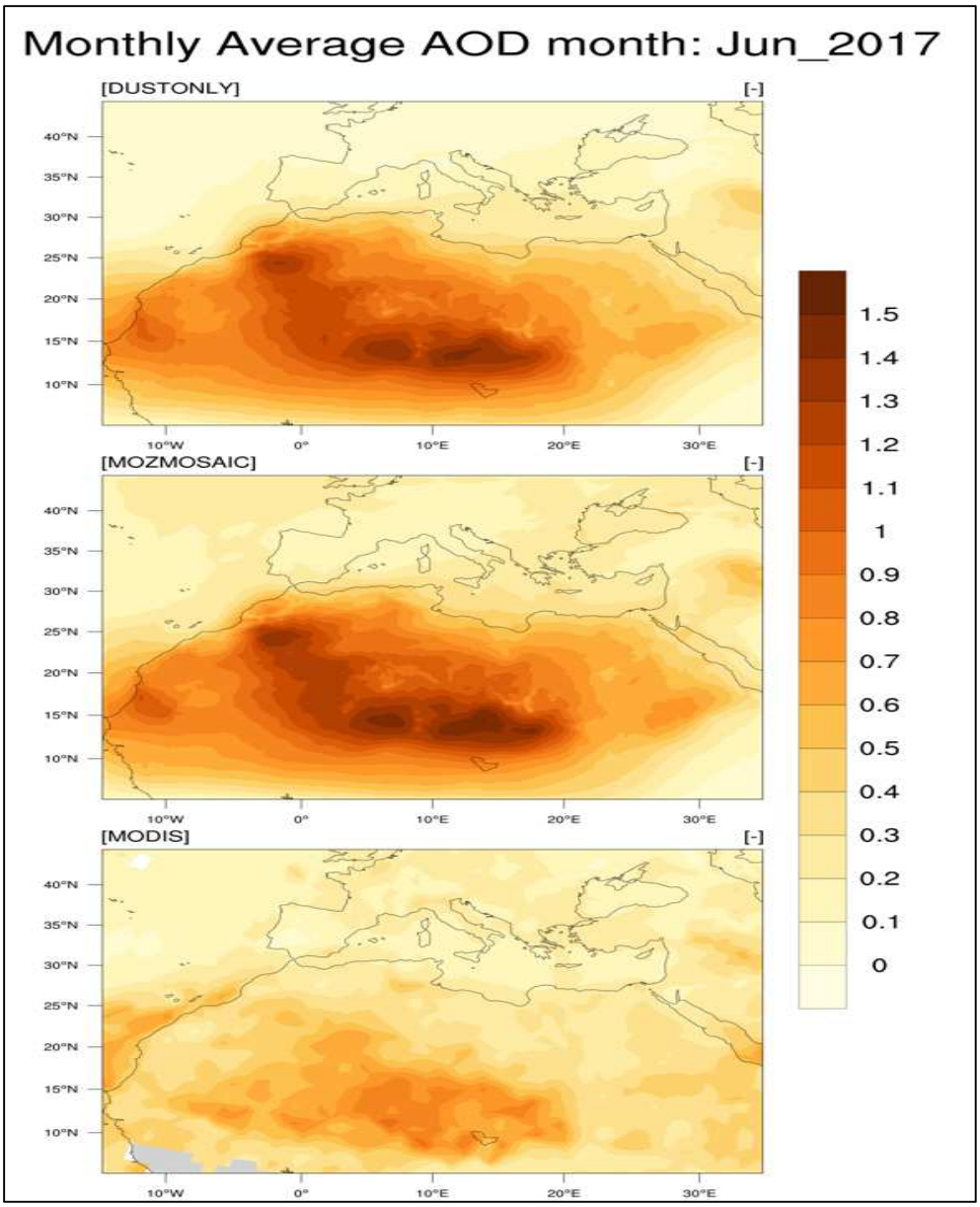

Appendix B. 3: Monthly average AOD [dimensionless] spatial distributions of the "DUSTONLY" simulation (top), the AOD at 550 nm for the simulation considering the "MOZART-MOSAIC" chemical option (center) (15 x 15 km grid resolutions) and MODIS AOD product (1° x 1° grid resolution) for June 2017.

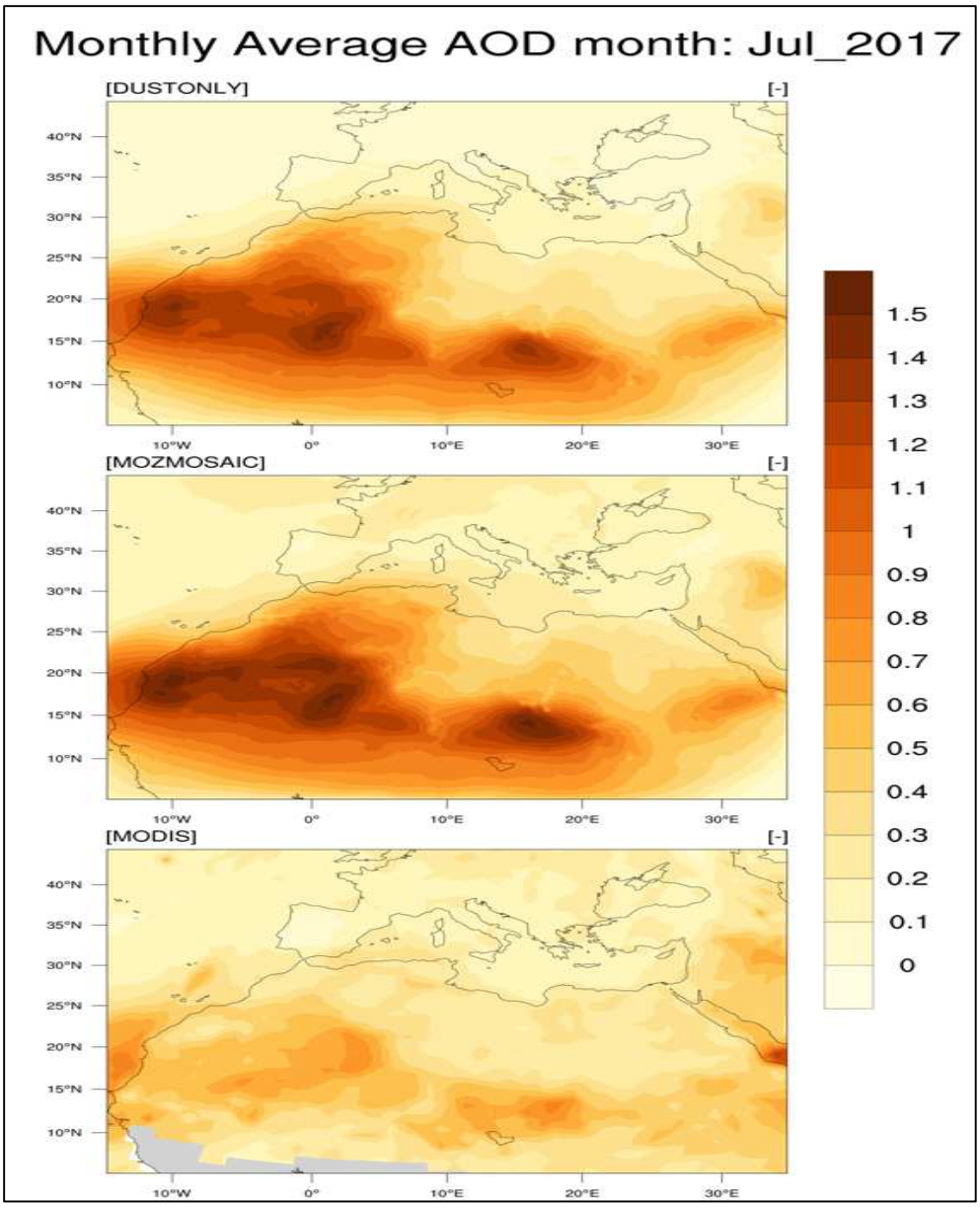

Appendix B. 4: Monthly average AOD [dimensionless] spatial distributions of the "DUSTONLY" simulation (top), the AOD at 550 nm for the simulation considering the "MOZART-MOSAIC" chemical option (center) (15 x 15 km grid resolutions) and MODIS AOD product (1° x 1° grid resolution) for July 2017.

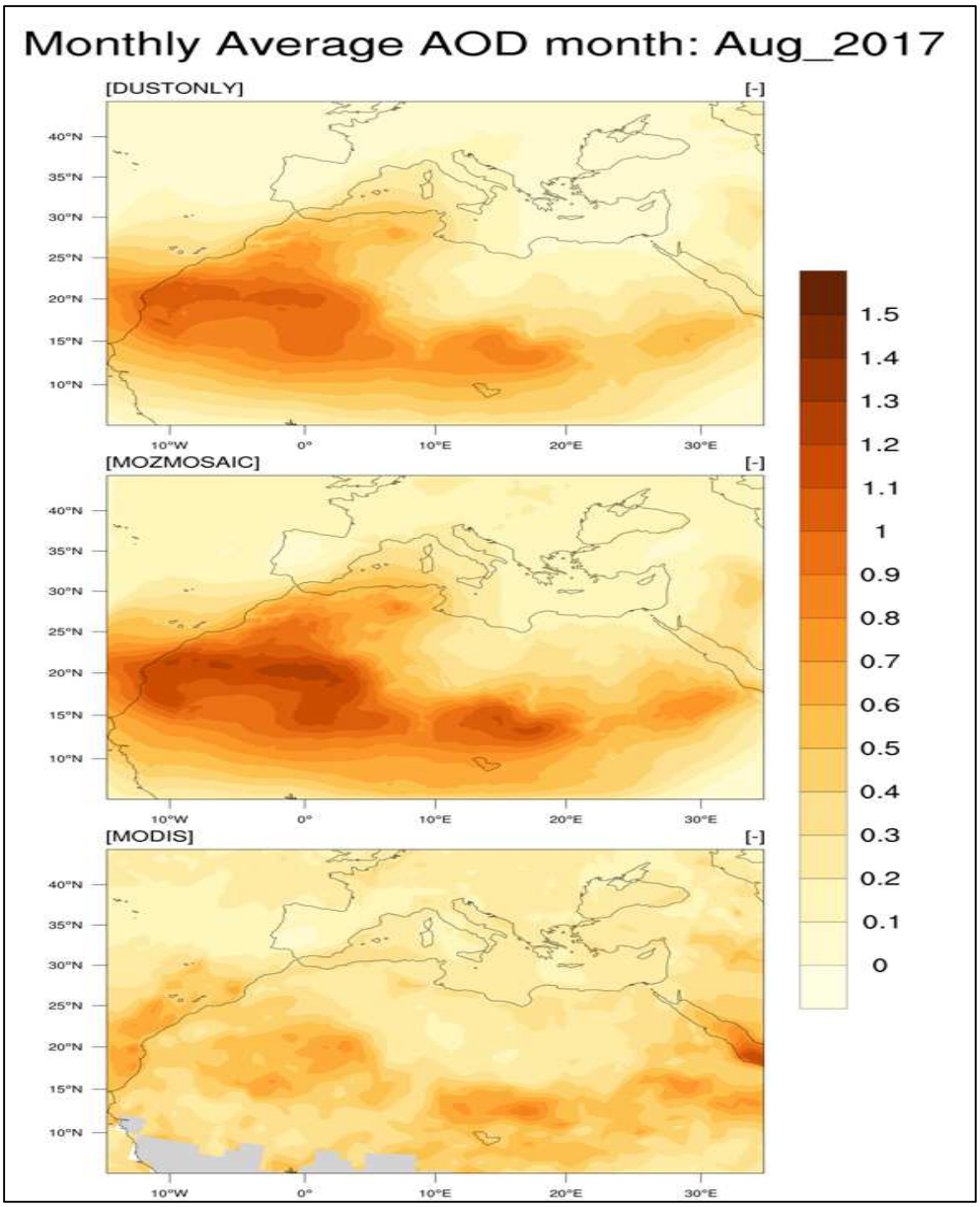

Appendix B. 5: Monthly average AOD [dimensionless] spatial distributions of the "DUSTONLY" simulation (top), the AOD at 550 nm for the simulation considering the "MOZART-MOSAIC" chemical option (center) (15 x 15 km grid resolutions) and MODIS AOD product (1° x 1° grid resolution) for August 2017.

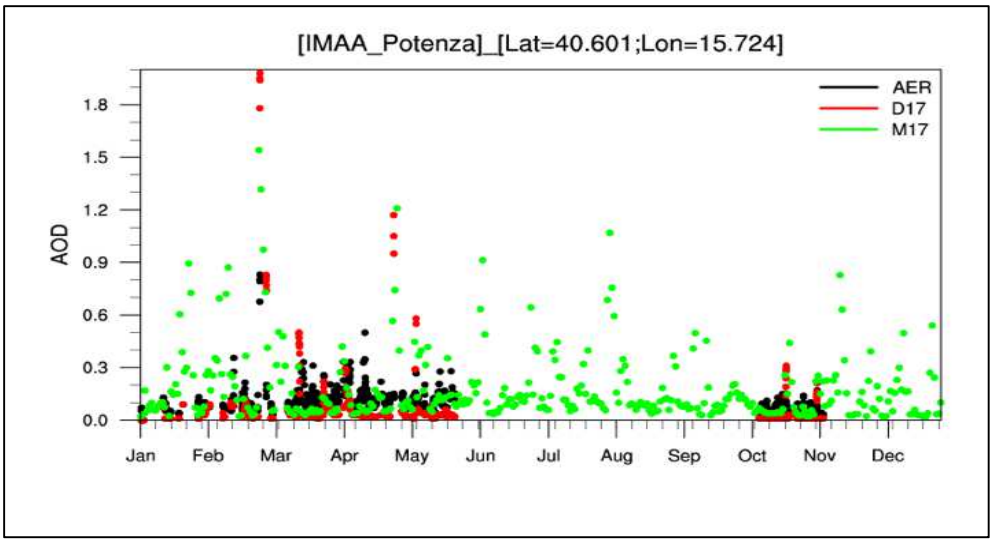

Appendix B. 6: Comparison of the daily average of AOD [dimensionless], at 550 nm, of the two simulations done "dust only"(D17) and "MOZART-MOSAIC" (M17) with the AERONET AOD level 2 at Potenza station (AER) (40.60° N, 15.72° E).

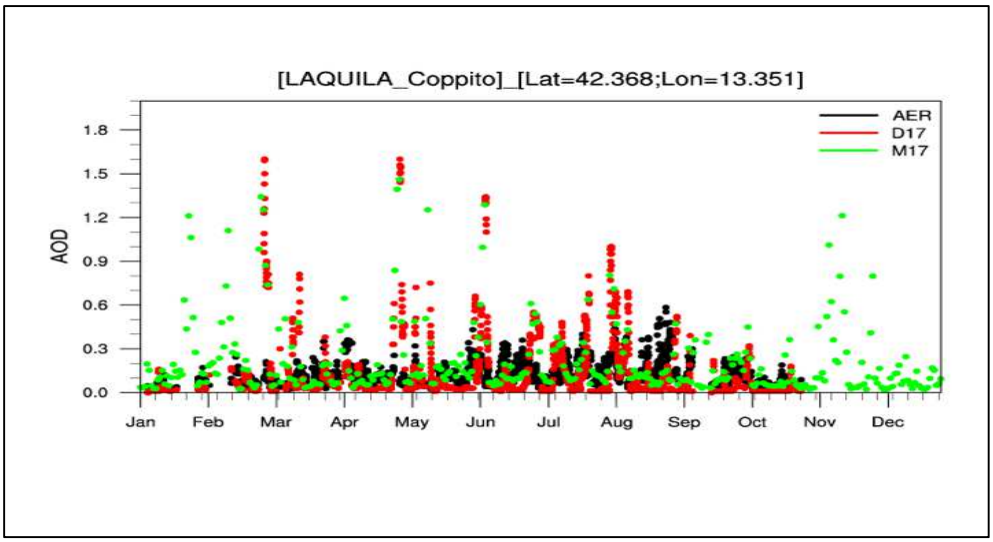

Appendix B. 7: Comparison of the daily average of AOD [dimensionless], at 550 nm, of the two simulations done "dust only"(D17) and "MOZART-MOSAIC" (M17) with the AERONET AOD level 2 at Aquila station (AER) (42.36° N, 13.51° E - Appendix B. 6).